Photofragmentation and Recombination Dynamics of Partially Solvated Anionic Clusters

by

Joshua P. Martin

B.S., Illinois State University, 2004

A thesis submitted to the

Faculty of the Graduate School of the

University of Colorado in partial fulfillment

of the requirements for the degree of

Doctor of Philosophy

Department of Chemistry and Biochemistry

This thesis entitled:

Photofragmentation and Recombination Dynamics of Partially Solvated Anionic Clusters

written by Joshua P. Martin

has been approved for the Department of Chemistry and Biochemistry by

_____

W. Carl Lineberger

_____

Robert Parson

Date: _____

The final copy of this thesis has been examined by the signatories, and we find that both the content and the form meet acceptable presentation standards of scholarly work in the above mentioned discipline.

Martin, Joshua P. (Ph.D. Physical Chemistry)

Photofragmentation and Recombination Dynamics of Partially Solvated Anionic Clusters

Thesis directed by Professor W. Carl Lineberger

Photofragmentation studies of mass-selected, partially-solvated anionic clusters are performed to investigate solvent-number specific perturbations to the dissociation dynamics of anionic chromophores. Two anion solutes are employed in the studies reported here: IBr^- and the chemically-related ICN^-. While the former has been the subject of earlier photodissociation studies, ICN^- has not been studied previously. Replacing Br with CN allows the possibilities of isomerization to INC^- and rotational excitation of a photofragment. Two quite different solvents, CO_2 and Ar, are utilized in the experiments. The CO_2 solvent is bound to the chromophore by ~200 meV. Its charge distribution gives rise to substantial electric quadrupole and higher moments that can modify the electronic structure of the solute ion. The Ar solvent is much more weakly bound to the solute (~50 meV), has no permanent multipole moments, and no possibility of rotational, vibrational or electronic excitation in the dissociation process. The contrasting photodissociation dynamics associated with the different combinations of these solutes and solvents reported in this Dissertation both provides new understanding and raises questions concerning photoprocesses in partially solvated ionic complexes.

Following 430 to 650 nm excitation of ICN^- to its $^2\Pi_{1/2}$ excited state, the predominant ionic photoproduct is I^-, with a minor CN^- component. Photodissociation of $ICN^-(Ar)_n$, n = 1–5, results in dominant I^- and $I^-(Ar)_n$ ionic photoproducts, the observation of single-solvent cage

recombination for $n = 1$, and highly solvated I^- and ICN^- photoproducts. The experimental results, electronic structure calculations, and quantum dynamics calculations together indicate that efficient transfer of a significant amount (> 0.3 eV) of the photoexcitation energy into rotation of the CN diatom occurs following dissociation of the chromophore.

Photofragmentation studies of $ICN^-(CO_2)_n$, $n = 1–18$, following 400, 500, and 600 nm excitation examine the influence of long-range solute-solvent interactions on the dissociation dynamics. While the dominant fragment from ICN^- excitation is I^-, the addition of even one CO_2 solvent results in dominant CN^--based photoproducts. Significant cage recombination products are observed for $n = 3$, 4, and 7 following 600, 500, and 400 nm excitation. Solvent evaporation experiments show that the average CO_2 solvent binding energy to the ICN^- chromophore is ~200 meV, consistent with earlier experiments on diatomic solutes.

to my Grandpa and Grandma Kettelkamp and my Grandma Martin

ne sis sapiens apud temet; ipsum time Dominum et recede a malo

Proverbia 3:7

Primitive	φ is positive
Ax. 1	$P(\neg\varphi) \leftrightarrow P(\varphi)$
Ax. 2	$P(\varphi) \wedge \Box\forall x[\varphi(x) \rightarrow \psi(x)] \rightarrow P(\varphi)$
Th. 1	$P(\varphi) \rightarrow \Diamond\exists x\varphi(x)$
Def. G	$G(x) \leftrightarrow \forall\varphi[P(\varphi) \rightarrow \varphi(x)]$
Ax. 3	P(G)
Ax. 4	$P(\varphi) \rightarrow \Box P(\varphi)$
Def. Ess.	φ Ess. $x \leftrightarrow \varphi(x) \wedge \forall\psi[\psi(x) \rightarrow \Box\forall y[\varphi(y) \rightarrow \psi(y)]]$
Th. 2	$G(x) \rightarrow G$ Ess. X
Def. NE	$NE \leftrightarrow \forall\varphi[\varphi \text{ Ess. } x \rightarrow \Box\ \exists x\phi(x)]$
Ax. 5	P(NE)
Th. 3	$\Box\exists xG(x)$

– Kurt Gödel

Acknowledgements

I want to thank Him who has given me strength, Christ Jesus my Lord. Without God's grace, mercy, and compassion I never would have able to learn so much from so many great teachers.

To my advisor Prof. Carl Lineberger, I wish to thank you for all your guidance and support throughout the years. Even after I stood in front of hundreds of the world's best physical chemists and roasted Carl, he took it all in stride. Additionally, I want to thank Carl for all the help he gave me in the laboratory, helping me whenever he could. As a member of Carl's group I have been able to interact and work with abundantly talented theoreticians, such as Prof. Robert Parson and Prof. Anne B. McCoy, and I am grateful.

The past and present members of the Lineberger research group have acted as teachers, collaborators, and, most importantly, friends. I want to thank Prof. Jack Barbera and Dr. Vladimir Dribinksi for introducing me to the instruments that would become my tools. Prof. Joshua Darr provided me the leadership and knowledge to begin performing the experiments on my own. Dr. Quanli Gu worked hard at continually asking me questions about the instrument and experiment to keep me continually thinking and learning. Dr. Amanda Case helped me in the lab near the end of my experimental work and read more versions of my dissertation than I can ever thank her for. Dr. Elisa Miller and Yu-ju Lu were always just beyond the lasers whenever I needed them. Both of them provided me with feedback to ideas and helping hands, and were my allies in the fight to keep the Infinity running. Dr. Scott Wren and Dr. Kristen Lemke were the ones past the wall that gave me sanctuary from experimental problems for the five minutes I

would need to recuperate. Also, thank you to all the past and present members of the Ion Super Group who always challenged and listened to me.

I want to thank all the brilliant professors and lecturers whom I have been a student of since I first came to CU. Thanks to Prof. Robert Parson, Prof. Casey Hynes, Prof. Niels Damrauer, and Prof. Rex Skodje for teaching me physical chemistry with such knowledge and enthusiasm. Thanks to Prof. Veronica Bierbaum, Prof. Barney Ellison, and Prof. Dr. Mathias Weber for all the amazing discussions and questions that came from the Ion Super Group meetings. As a TA, I learned so much about learning, teaching, and chemistry and I am very thankful to Prof. Robert Parson, Prof. Joel Eaves, Prof. Margaret Asirvatham, and Dr. Lynn Gieger for showing me how to teach.

Never was I met with a situation in the lab in which the extraordinary staff of JILA was not able to help. Krista Beck has kept the Lineberger group running efficiently and always knows the answer. To the staff of the machine and electronics shops, thank you for all of your skillful assistance. Each time I went to Tom Foote, James Fung-A-Fat, or Todd Asnicar with my simple questions, they would treat the situation and me with respect and support, and always save me in the end. Also, I want to thank all the JILA computing staff. Without the help of Peter Ruprecht and J.R. Raith I would not have been able to run calculations, let alone do it using Linux.

To all my family and friends outside of JILA, I want to thank you for always distracting me and keeping me sane. Thanks to my Grandpa Kettelkamp for pushing me to think simply and logically about problems and not necessarily jump straight to the “textbook” methods. To both of my Grandmas, thank you for always believing in me and never letting me forget that. To my parents, thank you for providing me with everything essential and not spoiling me with anything

that wasn't. You have always supported me in all my crazy ideas. To my parents-in-law, I could not have hoped for a better addition to my family and want to thank you for all your support. To my sister, thank you for continually pretending that I was the smart one, even though that's obviously not true.

To my wife. Without you I would have collapsed a long time ago. Thank you for always being so understanding and patient when I had to spend long nights in the lab or office. Thank you for putting up with me after I have been stuck in an office or lab by myself all day. Thank you for always listening to me talk about work, even though you don't always know what it is that I am talking about. Thank you for always reminding me to stop rambling on whenever I get carried away about something. Thank you for always believing till the very end that I could finish. Thank you for helping me in whatever way you could, without hesitation. I love you.

Table of Contents

List of Tables

List of Figures

Chapter I: Introduction

1.1 Solvation Effects

The vast majority of important chemical reactive processes take place in a condensed phase of matter. Such multi-particle environments make it extremely difficult to characterize the truly essential components of the process to obtain a molecular view of the reaction. The identity of these components cannot be uniquely specified in the abstract, but must be determined for different cases. In general, such components of a condensed phase reaction would include the reactants, possible catalysts, and some key solvent molecules. Indeed, to obtain a molecular level understanding of many chemical processes, the effects of solvation on the course of a reaction must be known. The influence that a solvent has on a reaction can be simple, such as creating a physical barrier to the motion of reactive species or acting as an energy sink stabilizing reaction products. The solvent's influence can be more complex, such as perturbing the potential energy surfaces of the reaction, or creating the opportunity for solvation-induced dynamics not observed for isolated reactants. The focus of this dissertation is the study of step-wise, solvation-induced dynamics following photodissociation of an anionic chromophore within a partially-solvated, size-selected anion-solvent complex.

The effect of solvation on photodissociation dynamics was first observed in the 1930's by Franck, Rabinowitch, and Wood.[1-3] They observed "caging" of photodissociated I_2 in polar solvents and concluded that collisions between the separating iodine atoms and the solvent (acting as a barrier) led to an increased probability that the dissociated iodine atoms would recombine to form covalently bound I_2. This process is known as **geminate** recombination.

Since this initial observation of the cage effect, a multitude of studies have further investigated this phenomenon in condensed-phase media.[4-10] However, the variable local environment of the solute in the condensed phase prevents elucidation of number- and configuration-specific solvation effects on photodissociation dynamics. Thus, only bulk averaged perturbations of the solute are detected.[11-14]

Utilization of mass-selected, partially-solvated solute-solvent complexes provides a well-defined solvent environment about the solute and allows the study of molecular level details of solvation effects without averaging over bulk conditions. Partially-solvated solute-solvent complexes are aggregates composed of one chromophore that weakly interacts with, but is not covalently bound to, solvent atoms or molecules. A primary motivation for the study of partially-solvated chromophores is to investigate the properties and dynamics of matter as it evolves from the gas to condensed phase as the number of solvent particles increases.[11, 15-18] These studies work to provide answers to questions such as, how many solvent particles are required in a cluster to observe bulk-like properties? For example, Leutwyler and coworkers[19, 20] utilized two-color resonant two-photon ionization and fluorescence emission spectroscopy of naphthol$(NH_3)_n$ clusters to study proton transfer from naphthol to NH_3. They reported that proton transfer was only observed when four or more solvent NH_3 molecules interact with naphthol inducing bulk-like processes.[21] Scoles and co-workers[22, 23] carried out infrared spectroscopic studies of $Ar_n \cdot SF_6$ and reported that solvation with approximately twelve argon atoms induced a shift in the vibrational spectrum that was comparable to values observed in matrices. McIlroy *et al*.[24] utilized a slit jet, difference frequency laser spectrometer to obtain high-resolution infrared spectra of Ar_nHF (n = 1–4). Their results show a clear red-shift in the

gas-phase infrared spectra as n increases from n = 1–4, indicating a weakening of the H–F bond by the interaction with "nearest neighbor" solvent Ar atoms.

1.2 Photofragmentation Dynamics of Solvated Dihalides

Mass selection of partially-solvated solute-solvent complexes is readily accomplished by utilization of ionic chromophores and standard mass spectroscopic techniques, such as tandem time-of-flight[25] and Fourier transform ion cyclotron resonance.[26] Within this dissertation, all work presented utilizes partially-solvated dihalide or pseudo-dihalide chromophores to study step-by-step solvation induced photodissociation dynamics; these anion-solvent complexes are henceforth referred to as "anionic clusters." The interactions between the anionic solute and neutral solvent are primarily electrostatic, resulting in binding energies of the solvent to the anionic chromophore that are larger than those observed for the corresponding solvated neutral solute.[27, 28] The properties of anionic clusters, such as ionization potential, electron affinity, chemical reactivity, and optical spectra are significantly perturbed by stepwise solvation when the cluster size ranges from one solvent particle to tens of particles.[29, 30] Following production and mass-selection of the desired anionic cluster, the photofragmentation dynamics of the cluster are examined by employing optical spectroscopic techniques. Due to the low particle densities generated by ion beam experiments,[25, 31] absorption spectroscopy is not feasible and, therefore, photofragmentation action spectroscopy is employed. In such experiments, a mass-selected parent anion is promoted, *via* a photon, from its bound ground state to a repulsive excited state. This results in direct, adiabatic dissociation of the parent anion and the formation of photoproducts (neutral and ionic). The production of ionic photoproducts is then monitored,

following secondary mass analysis, in order to elucidate the excitation energy and cluster size dependence of any observed solvation-induced photofragmentation dynamics.

Figure 1.1 illustrates the dissociation dynamics of a solvated chromophore following one-photon photoexcitation to a repulsive excited state. The dashed-blue arrow in Fig. 1.1 corresponds to the direct dissociation of the solvated dihalide. Addition of one solvent particle to the bare chromophore leads to an increased probability of nonadiabatic transitions (dash-black line in Fig. 1.1) from the excited state to the ground state at large internuclear distances. A key difference between neutral and anionic cluster photofragmentation dynamics is the charge-transfer (dashed-red arrow in Fig. 1.1) process that may occur following this nonadiabatic transition. This process is solvent-induced and strongly coupled to the motion of the solvent during dissociation of the chromophore.

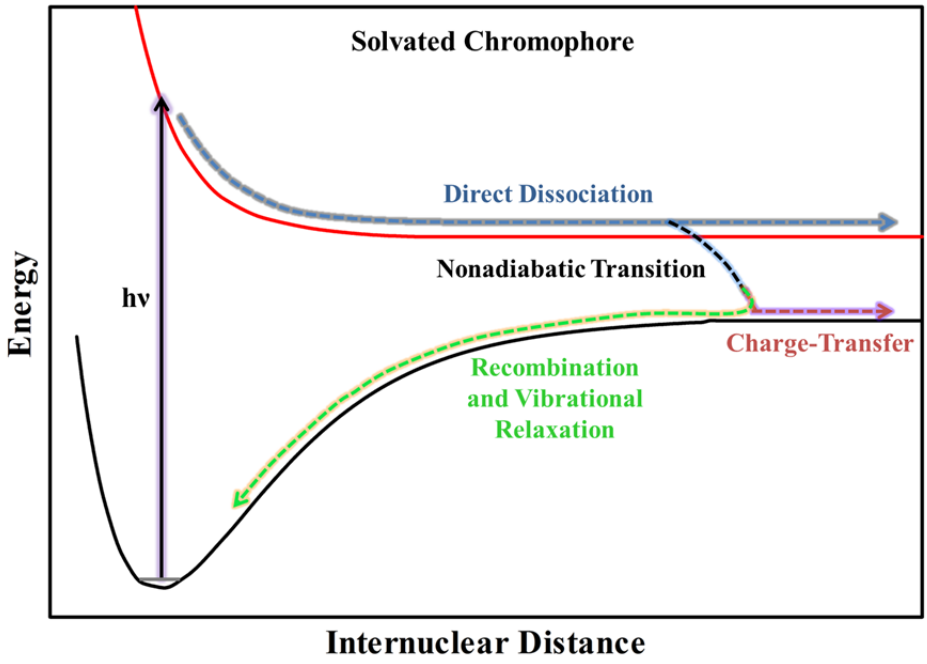

Figure 1.1 Schematic of one-photon photoexcitation of a solvated chromophore to a repulsive excited state followed by dissociation, charge transfer, or recombination. The solid arrow represents photoexcitation *via* a photon with energy hν.

With one or two solvent molecules, geminate recombination of the dissociating chromophore can sometimes be observed[32-35] (dashed-green arrow in Fig. 1.1). In the type of geminate recombination depicted here, the dissociating dihalide must undergo a nonadiabatic transition to the ground state, possibly with extensive vibrational excitation. Collisions with the solvent and solvent evaporation may further relax the recombined chromophore. The observation of > 80% recombination for partially-solvated dihalide–solvent complexes[32-36] is especially striking in light of the low yield of recombined products observed in solution.[5, 9] This gas-phase recombination process is solvent induced, similar to the "caging" of photodissociated I_2 in solution reported by Franck, Rabinowitch, and Wood.[1-3] However, recombination of a gas-phase, partially-solvated chromophore involves fewer solvent particles than in the condensed phase and

is the result of perturbations of the electronic structure of the chromophore from solvation leading to the nonadiabatic transitions. Additionally, the dihalide chromophore is stabilized by dissipation of excess energy from photoexcitation to the solvent particles. This leads to solvent evaporation, a process that does not occur in condensed-phase media.

Previous one-photon photofragmentation studies[33-35] of $I_2^-(CO_2)_n$, $IBr^-(CO_2)_n$, and $ICl^-(CO_2)_n$ clusters following excitation to the repulsive $\tilde{A}'\ ^2\Pi_{1/2}$ excited state revealed the effect of solvation on the dissociation dynamics of solvated dihalides. Of particular interest is the efficiency of solvent CO_2 molecules to induce recombination of the three different chromophores. Following photoexcitation to the $\tilde{A}'\ ^2\Pi_{1/2}$ excited state, the yield of recombined photoproducts observed increases as *n* increases; the maximum yield reached following excitation of $ICl^-(CO_2)_n$ clusters is 80%, whereas the yields reached 100% recombined products for $I_2^-(CO_2)_n$ and $IBr^-(CO_2)_n$. Additionally, the yield of recombined photoproducts for $IBr^-(CO_2)_n$ and $ICl^-(CO_2)_n$ increases rapidly from zero to > 80% at small values of *n*. This is in stark contrast to the gradual increase observed as *n* increases from two to sixteen for $I_2^-(CO_2)_n$ clusters. The distinct similarities and sharp differences in the yield of recombined products following excitation of these clusters are a result of not only the difference in size of the chromophore, but also the location at which solvation occurs around a homonuclear versus heteronuclear dihalide. Within this Thesis, photofragmentation studies of $ICN^-(Ar)_n$ and $ICN^-(CO_2)_n$ clusters provide further understanding of the effects of solvation on photodissociation dynamics.

Although photofragmentation studies provide information on the effects of solvation, these experiments only investigate the results of dissociation dynamics roughly 10 μs after

photoexcitation. In order to investigate the photodissociation dynamics on the timescale of the nuclear motion, time-resolved probe-pump spectroscopic techniques are utilized. Figure 1.2 illustrates the photodissociation dynamics of a solvated chromophore and the **one-color**, pump-probe scheme employed in time-resolved absorption recovery measurements. Following excitation of the cluster to a repulsive excited state, the dissociating chromophore can undergo a nonadiabatic transition to the ground state, and vibrationally relax by evaporating some number, m, of solvent atoms or molecules. When sufficient vibrational relaxation has occurred in the recombined chromophore, it will regain significant photoabsorption at the excitation wavelength, and the probe laser will again be able to excite the recombined chromophore. Two-photon ionic photoproducts are then detected as a function of the time delay (Δt in Fig. 1.2) between the pump and the probe pulses. In order to recognize the two-photon signal of recombination and vibrational relaxation, at least one of the two-photon photoproducts must have a mass different from that of any one-photon product.

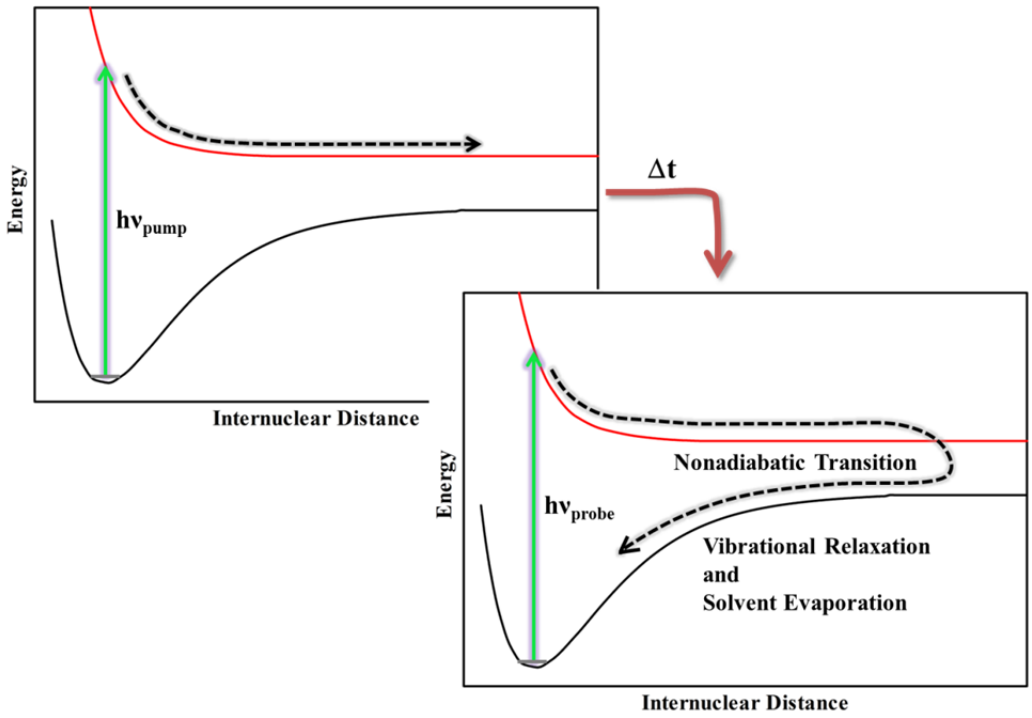

Figure 1.2 Schematic illustration of the dynamics of the dissociating cluster following photoexcitation in a one-color, pump-probe time-resolved absorption recovery experiment. The pump ($h\nu_{pump}$) and the probe ($h\nu_{probe}$) laser pulses are indicted by the solid arrows and Δt indicates the time delay between the pump and probe. The dashed arrow illustrates a possible trajectory of a solvated-dissociating chromophore that results in recombination in the ground electronic state well.

An ongoing collaboration between experimental and theoretical studies to examine the effects of solvation on the timescale of absorption recovery has revealed the drastic changes in the photodissociation dynamics that accompanies changes to the solute composition. Papanikolas *et al.*[34, 37] studied the time-resolved absorption recovery of $I_2^-(CO_2)_n$ following excitation to the $\tilde{A}'\ ^2\Pi_{1/2}$ excited state. Their results showed a decrease in the recombination time from ~30 ps to ~10 ps, as *n* increased from nine to sixteen. However, Dribinski *et al.*[38] reported an increase in the recombination time of $IBr^-(CO_2)_n$ from tens of picoseconds to roughly 1 ns as *n* increased from five to ten. This dramatic difference in the recombination dynamics gave

important clues concerning the influence of the **location** of the solvent molecules during the processes of solute recombination and relaxation. In this case, the important effect related to the size difference between Br and I, as well as the strong electric multipole moments (quadrupole and higher) of CO_2. Because the ionic radius of bromine is smaller than that of iodine, solvation begins to occur on the Br end of the IBr^- chromophore following the addition of the third CO_2 molecule.[39] This asymmetric solvation produces a strong electric field at the location of the chromophore, inducing a shallow well on the IBr^- $\tilde{A}'\ ^2\Pi_{1/2}$ excited state; the well depth increases as the asymmetry increases. The maximum depth of this well occurs with a half-filled solvent shell; this maximum depth is sufficient to trap IBr^- in the $\tilde{A}'\ ^2\Pi_{1/2}$ excited state, and extend the recombination time to the radiative lifetime of the perturbed IBr^- $\tilde{A}'\ ^2\Pi_{1/2}$ excited state. One thus might expect increasing recombination times as the number of CO_2 solvent molecules is increased up to the point of maximum solvent asymmetry (roughly a half filled solvent shell).[38] Electronic structure calculations and molecular dynamics simulations show that further solvation ($n > 10$) leads to more symmetric solvation of IBr^- and less trapping on the $\tilde{A}'$ excited state.[38] Thus, the timescale for absorption recovery might be expected to decrease as the extent of solvation is increased beyond a half-filled solvent shell. Performing this test is accordingly one of the objectives of this Thesis.

1.3 Dissertation Overview

The remainder of this Thesis comprises five chapters. Chapter II details the experimental apparatus and methods utilized to study the photofragmentation dynamics of partially-solvated anion-solvent complexes. The photofragmentation dynamics[40] of $ICN^-(Ar)_n$, $n = 0–5$, clusters following 430–650 nm excitation to the $^2\Pi_{1/2}$ excited state of the ICN^- chromophore and the

subsequent kinematics are discussed in Chapter III. Experimental and theoretical results[40] provide evidence for the distribution of a significant amount of energy into the rotation of the CN diatom following dissociation of ICN^-. The results of photofragmentation of $ICN^-(CO_2)_n$ clusters following 400, 500, and 600 nm excitation are presented in Chapter IV and elucidate the effects of long-range solute-solvent interactions. Time-resolved absorption recovery studies[39] of dissociating $IBr^-(CO_2)_n$, n = 11–14, following 790 nm pump-probe excitation to the $\tilde{A}'\ ^2\Pi_{1/2}$ excited state are presented in Chapter V. Finally, Chapter VI presents preliminary results of the photofragmentation of $ICN^-(Ar)_n$, n = 0–5, following 270–330 nm excitation and provides ideas for future experiments that build on the work presented in Chapters III–V.

Chapter II: Experimental Apparatus and Methods

2.1 Overview

The experimental apparatus and methods utilized to perform photodissociation studies of anionic clusters are described in this chapter. Each experiment is performed by interrogating specific anionic cluster sizes and compositions with laser radiation and detecting the photoproducts of the ion-laser interaction. The experimental apparatus is discussed as four sections that perform the following functions: production of anionic clusters, mass separation and selection of cluster size, photoexcitation of the anionic chromophore, and secondary mass selection and detection of photoproducts. Figure 2.1 is a schematic diagram of the experimental apparatus. The production of anionic clusters is achieved through electron-impact ionization and attachment of slow-secondary electrons to a chromophore within a pulsed gas expansion. The anionic clusters are extracted into a Wiley-McLaren time-of-flight mass spectrometer[41] where they are mass separated. Laser radiation intersects the mass-selected clusters, resulting in photoproducts. Finally, the ionic photoproducts are separated by a secondary reflectron mass spectrometer and are detected by a microchannel plate detector. The nanosecond and femtosecond laser systems utilized to investigate the photofragmentation and time-resolved recombination of solvated anionic chromophores, respectively, are also discussed in further detail.

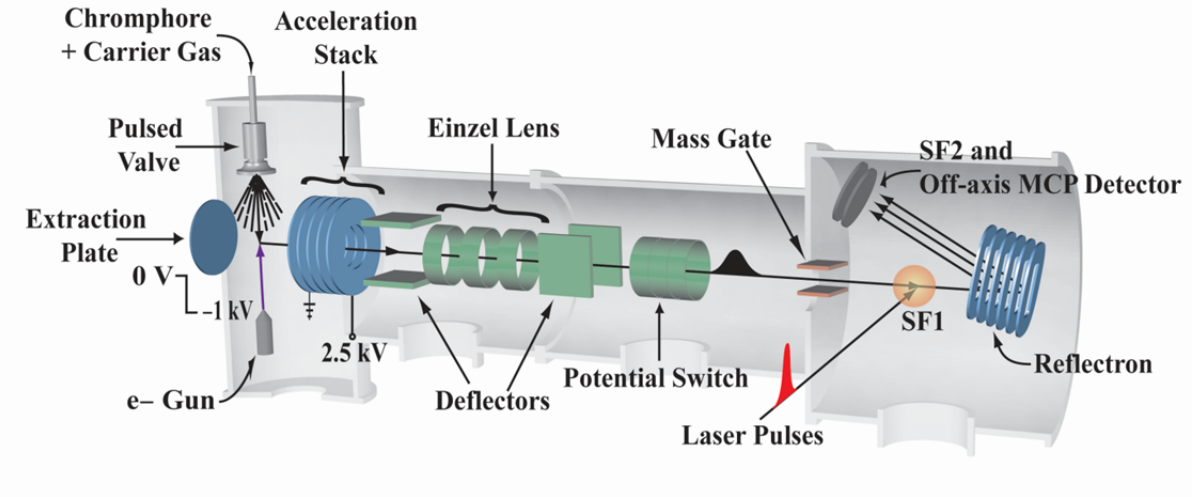

Figure 2.1 Schematic diagram of the ion source and time-of-flight mass spectrometer.

2.2 Cluster Ion Source and Cluster Formation

The two anionic chromophores studied, cyanogen iodide (ICN^-) and iodine monobromide (IBr^-), have neutral counterparts that are stable solids in ambient laboratory conditions. The IBr crystals are purchased from Aldrich (98% purity, CAS# 7789-33-5); however, due to a lack of commercial availability of ICN, the ICN sample is synthesized by the experimental procedure reported by Bak and Hillebert.[42] The neutral ICN and IBr, have sufficient vapor pressures at room temperature, ~0.9 Torr (Ref. 43) and ~5 Torr,[44, 45] respectively, that neither the container holding the solid sample nor the pulsed valve need to be heated. Additionally, by replacing all stainless steel gas supply lines with Teflon lines, the time required to passivate the supply line when performing experiments with IBr^- is reduced from a week[35] to ~1 day.[46]

The production of anionic clusters begins by passing 1–2 atm of neat CO_2 (or neat Ar in the case of $ICN^-(Ar)_n$ clusters) through a stainless steel reservoir containing the solid sample at

room temperature. The carrier gas, which mixes with the vapor from the solid sample, is pulsed into the ion source chamber using a Series 9 General Valve. For these experiments, the General Valve is equipped with an 800 μm orifice conical nozzle, a Kel-F poppet (Parker Hannifin), a Viton O-ring (Parker Hannifin), and a Teflon-coated armature (Parker Hannifin). The solenoid of the General Valve is driven by a single-channel Iota One (Parker Hannifin) pulse driver that is triggered by a TTL pulse from a digital delay generator (Stanford Research Systems, model DG535). For the photofragmentation studies, the valve is operated at 50 Hz, and for the time-resolved studies the repetition rate of the valve is set to 100 Hz. The source chamber is pumped by a 10" diffusion pump (National Research Corporation) that is backed by a Welch mechanical pump. Without a gas load, the nominal pressure of the source chamber is roughly $1x10^{-7}$ Torr. The running pressure in the source chamber reaches roughly $1x10^{-5}$ to $1x10^{-4}$ Torr, depending on the optimal conditions for anionic cluster production.

During the expansion, the gas mixture intersects a beam of electrons (~1 keV, ~200 μA) from a homebuilt electron gun. The electron gun consists of a bent ribbon filament (thoriated iridium, Electron Technology, Inc.) that is floated at −1000 V and generates electrons *via* thermionic emission. The tip of the filament is positioned just above the knife-edge of an electrode held at −200 V with respect to the potential on the filament. The electrons repelled by the anode are then focused by an einzel lens (−750 to −1000 V) and steered vertically and horizontally by two pairs of deflectors to optimize ion production. Additionally, a ring magnet is placed on the faceplate of the pulsed valve, around the nozzle, to direct electrons toward the densest portion of the gas expansion.

Low-energy secondary electrons produced *via* ionization of the gas mixture can attach to molecules, forming anions and an overall neutral plasma. Coulomb screening and ambipolar diffusion reduce the diffusive spread and allow for a high density of ions within the plasma. The internal energy of the anionic clusters produced is estimated to be ~40–70 K based on previous studies.[36]

Formation of anionic clusters (Eq. 2.1) is dependent on the reaction time and the gas density in the expansion as it involves a termolecular attachment of the electrons[47] and is described as

$$X + e^-(\text{secondary}) + M \rightarrow X^- + M, \qquad (2.1a)$$

$$X^- + S + M \rightarrow X^-(S) + M, \qquad (2.1b)$$

$$X^-(S)_n + S + M \rightarrow X^-(S)_{n+1} + M, \qquad (2.1c)$$

where X^- is a general chromophore, S is the neutral solvent, and M is a third body collision partner (X or S). Following the formation of an anion (Eq. 2.1a), neutral solvent atoms or molecules condense around the charge center, X^-, and are stabilized by collisions with M, Eq. 2.1b. This process continues as $X^-(S)_n$ collides with more S and M to produce cluster anions of various sizes. For example, Figure 2.2 shows a typical mass spectrum of $ICN^-(Ar)_n$ clusters, n = 0–3, formed through this process. Additionally, evaporation of monomer solvent atoms or molecules and collisions between the $X^-(S)_n$ with neutral M result in the dissipation of excess energy. Because this mechanism requires a number of collisions for cluster growth, long drift distances (long reaction times) and high density expansions are favorable. In the Langevin approximation,[48] the collision rate of an ion with a polarizable neutral is independent of

temperature, while the neutral-neutral collision rate is proportional to the square root of temperature, and, therefore, falls off rapidly with decreasing temperature.[25] Thus, at the low temperatures of the gas expansion neutral-neutral collisions are negligible, but a large number of collisions between ions and neutrals occur. This provides an ideal environment for anionic cluster growth.

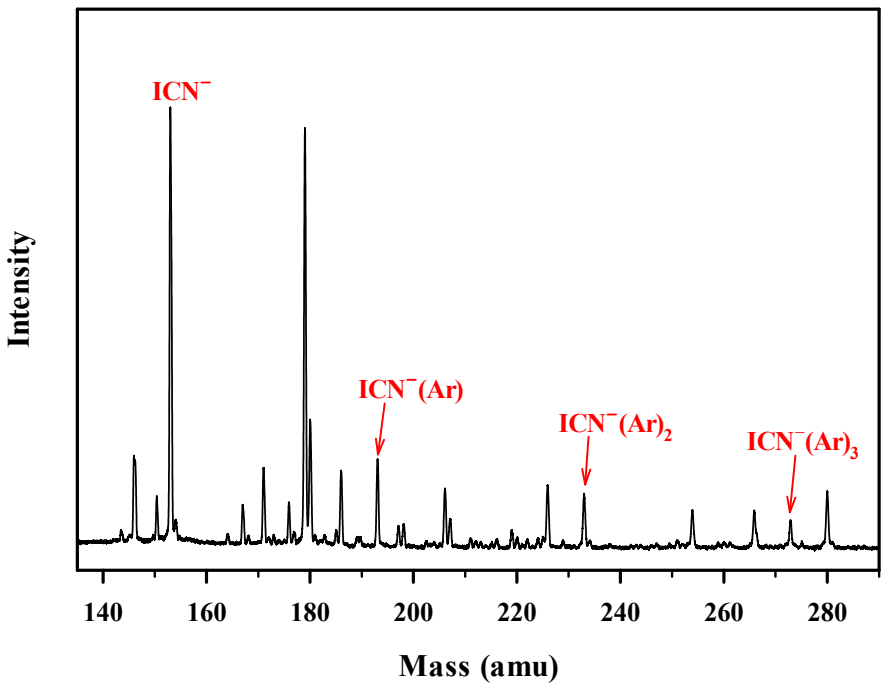

Figure 2.2 Time-of-flight mass spectrum of $ICN^-(Ar)_n$ clusters, n = 0–3. The unlabeled peaks present include $I(CN)_2^-$, $CN^-(Ar)_n$ clusters, and $I^-(Ar)_n$ clusters, for example.

2.3 Primary Time-of-Flight Mass Spectrometer

A full discussion of the time-of-flight mass spectrometer (TOF MS) has been presented elsewhere;[34] therefore, only relevant details will be discussed here. Following formation in the neutral plasma, the ions drift for roughly 15 cm, after which the anionic clusters are extracted by a transverse, pulsed-electric field into a differentially-pumped Wiley-McLaren TOF MS.[41] In general, a Wiley-McLaren TOF MS achieves mass separation of ions by accelerating them through two acceleration regions into a third field-free region. The two accelerating fields are adjusted to obtain a spatial focus at the ion-laser intersection (Wiley-McLaren condition). Additionally, the double acceleration corrects for the inherent energy spread in the extracted ion beam due to the initial position of the anions within the extraction region.

The pulsed-extraction of the anions takes place in the primary acceleration stage and the rising-edge of the square pulse defines $t = 0$ in the Wiley-McLaren TOF MS. To produce the extraction pulse, a TTL pulse from a delay generator (Stanford Research Systems, model DG535) triggers a homebuilt pulse generator, to which high voltage is supplied from an external source. The extraction pulse is roughly1 ms in duration and a 10 ns rise time; the long duration and short rise time are required to obtain spatial focusing of the ion beam because all anions must experience the same uniform electric field while in the extraction region. Typically, both the negative voltage applied to the extraction plate (−1000 to −1500 V from earth ground) and the timing of the extraction pulse are varied to achieve the Wiley-McLaren condition.

The extracted anions have roughly 1 keV kinetic energy and enter the second acceleration region of the TOF MS by passing through a 4 mm aperture. A stack of ten isolated and resistively coupled stainless-steel guard rings form an acceleration stack that accelerates the

anions to a total energy of ~3.5 keV. This is accomplished by applying a DC voltage of 2.5 kV to the last ring of the stack such that the anions are given an additional 2.5 keV of kinetic energy. From the end of the acceleration stack it is roughly 1.5 m to the spatial focus (SF1 in Fig. 2.1) of the TOF MS.

Directly after exiting the acceleration stack, the anions are steered by a pair of vertical deflectors (floated roughly 0–20 V above the beam potential) before entering an einzel lens operating in decelerating mode. The einzel lens consists of three stainless steel cylinders; the first and the last cylinders are held at the beam potential and the middle cylinder is floated at roughly 900 to 1100 V above the beam potential; this creates a focusing lens with the electric field. After exiting the einzel lens the anions encounter a second pair of deflectors that steer them horizontally and are floated roughly 0–40 V above the beam potential. A 1.5° horizontal bend in the mass spectrometer, located after the horizontal deflectors, separates stray neutral atoms or molecules formed during collision-induced dissociation or metastable decay of the anions in the extraction and acceleration regions from the ion beam.

To avoid floating the detection region of the mass spectrometer at 2.5 kV (the ion beam potential), a potential switch[49] is utilized to re-reference the potential of the anions to earth ground. The potential switch is composed of a 40 cm long cylindrical wire mesh with a 2.5 cm diameter aperture at each end. As the desired anions reach the center of the potential switch, a pulser (Directed Energy, Inc., model PVX-4140) switches ($\Delta t \leq 25$ ns) the potential on the mesh to earth ground, re-referencing the anions to earth ground and providing a mass-to-charge transmission window corresponding to the flight time in the potential switch cylinder. For most of the experiments reported here, this time corresponds to a mass range of $\Delta m \sim 130$ amu.

A pulsed mass gate is positioned 4 cm before the anions reach the Wiley-McLaren spatial focus (SF1 in Fig. 2.1). The purpose of the mass gate is to transmit only anionic clusters of a selected mass-to-charge ratio and reduce background noise by vertically deflecting unwanted ions from the beam path. The mass gate consists of three pairs of horizontal, parallel stainless steel plates enclosed in a stainless steel housing with a 4 mm diameter entrance aperture and 5 mm diameter exit aperture. The lower plate in each pair is at earth ground, while the upper plates are pulsed between −200 V and earth ground. When −200 V is supplied to the upper plates, all anions entering the mass gate housing are deflected. When the voltage is pulsed off, the top plates are at earth ground and the desired anions are allowed to pass through the mass gate undeflected. To switch the upper plates of the mass gate between the two potentials, a pulser (Directed Energy, Inc., model GRX, referred to as the DEI box) is supplied with two input voltages (−200 V and earth ground) and a trigger pulse. The trigger pulse is generated by a homebuilt, NIM-rack mounted, mass-gate driver that is supplied two TTL trigger pulses from a digital delay generator (Stanford Research Systems, model DG535). The first TTL pulse triggers the DEI box to switch the potential on the mass gate to −200 V, deflecting all the anions. The second pulse from the driver triggers the DEI box to switch the potential on the mass gate to earth ground. This second pulse, supplied by the mass gate driver, has an adjustable temporal width typically set between ~200 and 500 ns. Following the second pulse, the DEI box reapplies −200 V to the mass gate deflecting the anions. Successful implementation of the pulsed mass gate permits unambiguous selection of a single cluster anion size.

After traveling roughly 4 cm from the mass gate, the anions are intersected by pulsed laser radiation at the Wiley-McLaren spatial focus (SF1 in Fig. 2.1). Optimization of the temporal overlap of the anions and laser radiation is accomplished by adjustment of the timing

delay between the extraction pulse and laser pulse, while monitoring the intensity of an ionic photoproduct (see Sec. 2.6.1). At the spatial focus, the ion packet has been measured to have a roughly 4 mm waist and is predicted to be roughly 4 mm in length along the beam axis. Additionally, the ion packets are estimated to consist of 10^3 to 10^4 ions.

2.4 Secondary Mass Spectrometer and Detector

Following photodissociation of a parent ion at the ion-laser interaction, the photoproducts (ionic and neutral) enter a single-stage reflectron mass analyzer[50] roughly 10 cm upstream from the exit of the mass gate with the same velocity the parent ion had at the time of photodissociation. The reflectron consists of a stack of ten concentric cylindrical electrodes, which are separated by Mylar washers and separated by resistors so as to maintain a uniform retarding electric field. The reflectron is mounted such that the deflection angle between the retarding field and the ion beam propagation direction can be varied from ~5° to ~10°; this angle is typically set at 8°. As the photoproducts traverse the reflectron, the ions experience a retarding electric field and only penetrate to a specific depth in the reflectron, determined by each ion's kinetic energy. As an ion penetrates the retarding field, the ion decelerates until its velocity along the beam axis goes to zero and its trajectory is reversed. Consequently, ions with the same mass and spatial position, but different energies, will penetrate to different depths and exit the reflectron at different times and positions. After exiting the reflectron, the ions enter a roughly 20 cm field-free drift region in which the more energetic ions (the ions that spent more time in the reflectron) will overtake the less energetic ions of the same mass. The point in space at which this occurs is the second spatial focus (SF2 in Fig. 2.1) and is the optimal location for the off-axis detector. Therefore, the reflectron provides secondary mass-selection of the ionic photoproducts

and increased mass resolution. The energetic neutral photoproducts, however, pass unperturbed through the reflectron and after exiting are monitored on an inline channeltron detector (Burle Electro-Optics, Model 32685).

As described above, the spatial focus following the reflectron, SF2, is the position in space at which the more energetic ions overtake the less energetic ones. The distance from the exit of the reflectron to SF2 will vary according to the mass of the ion and will be different for an ionic photoproduct and the parent ion. The position of SF2 for an ionic photoproduct is found by taking the derivative of the total travel time of the ionic photoproduct within the reflectron with respect to the parent ions average kinetic energy, E_k, and setting it equal to zero to obtain

$$d = \frac{4m_f E_k}{qE_r m_p}, \qquad (2.2)$$

where d is the distance from the exit of the reflectron to the second spatial focus (SF2), m_f is the mass of the photofragment, q is the elementary charge, E_r is the magnitude of the reflectron electric field, and m_p is the mass of the parent ion. As a result, to detect photofragments the electric potential on the reflectron is adjusted so that SF2 of the ionic photoproduct is located at the off-axis detector face. Additionally, by adjusting the potential on the reflectron, the ionic photoproducts will penetrate to the same depth and have the same travel time through the reflectron to the detector as the parent ion. This provides an unambiguous identification of the ionic photoproduct mass.

The off-axis detector, positioned at SF2, utilizes dual microchannel plates (Burle Electro-Optics, model 31558, referred to as MCP), that are in a chevron configuration and 25 mm in diameter. Just prior to the MCPs, the ions encounter three mesh grids. The first grid is at earth

ground and the second is biased at −200 V to eliminate low energy electrons, thereby reducing detector noise. The final grid, also at earth ground, is resistively coupled to three concentric stainless steel rings by three 10 MΩ resistors, allowing acceleration of the product ions by an additional 3 keV. The acceleration stack is utilized to increase the detection efficiency of the MCPs by providing the ions with an additional 3 keV of energy. The final ring in the acceleration stack is resistively coupled to the face of the first MCP, which is constantly maintained at the beam potential (3 kV). The second MCP is coupled to the collector anode by a Zener diode that provides a 200 V drop in the voltage between the MCP and the anode. When detecting parent anions, the collector anode biased at 4.7 kV and the face of the second MCP biased at 4.5 kV. When detecting one-photon photoproducts during photofragmentation experiments, the MCPs are operated with a higher voltage applied to the collector anode to increase the gain of the MCPs; the second MCP is biased at 4.8 kV and the collector is at 5.0 kV. For time-resolved experiments, a still higher gain in required to observe the two-photon products; therefore, the face of the second MCP is biased at 5.1 kV and the anode is at 5.3 kV.

2.5 Laser Systems

2.5.1 Nanosecond Laser System

A nanosecond laser is used to study the photofragmentation of ICN^- and solvated ICN^- (Chapters III, IV, and VI). The laser system employed has been described in detail previously[51] and, therefore, only an overview will be presented here.

The nanosecond laser employed in these experiments is a Coherent Infinity laser, with a Coherent XPO and 2nd harmonic generation stage. A Q-switched master oscillator pumps two

Nd:YAG (neodymium-doped yttrium aluminum garnet, Nd:$Y_3Al_5O_{12}$) rods resulting in 1064 nm fundamental light. The 1064 nm radiation can be frequency doubled and tripled to produce 532 nm and 355 nm light, respectively, by using two type I BBO (β-barium borate) crystals (SHG and THG in Fig. 2.3). The 355 nm light is then directed into a build-up cavity that pumps a third type I BBO crystal in an optical parametric oscillator (henceforth referred to as XPO). The BBO crystal in the XPO produces both signal (420–680 nm) and idler (730–900 nm) radiation from the 355 nm light. The output pulse energies of the signal radiation range from 1–20 mJ, with an energy resolution of < 8 cm^{-1}. Additionally, the light generated in the XPO can be frequency doubled by another type I BBO crystal (SHG(2) in Fig. 2.3) to generate 210–340 nm light from the signal and 365–450 nm light from the idler radiation.

The photofragmentation experiments require a laser beam with relatively uniform spatial intensity and known size. A 2:1 telescope collimates the laser beam and a periscope is utilized to raise the elevation of the laser beam to the entrance of the TOF MS. Depending on the polarization of the light required in the experiment, the setup of the periscope can be altered to rotate the polarization of the light. An additional optical path is constructed using a removable mirror that picks off the laser beam and allows for measurement of the laser beam diameter (dashed path in Fig. 2.4). The length of this path is such that a knife-edge, used for determining the beam diameter, is at the same distance as the ion-laser interaction from the last turning mirror to ensure measurement of the diameter at the interaction. The diameter of the laser beam is determined by fitting the curve produced by measuring the transmitted pulse energy as the knife-edge is moved in the *x* or *y* plane of the beam with an analytic equation reported by Khosrofian and Garetz.[52] Typically, the laser beam is optimized by adjusting the focusing

conditions of the telescope in order to have a diameter of roughly 8 mm at the ion-laser interaction.

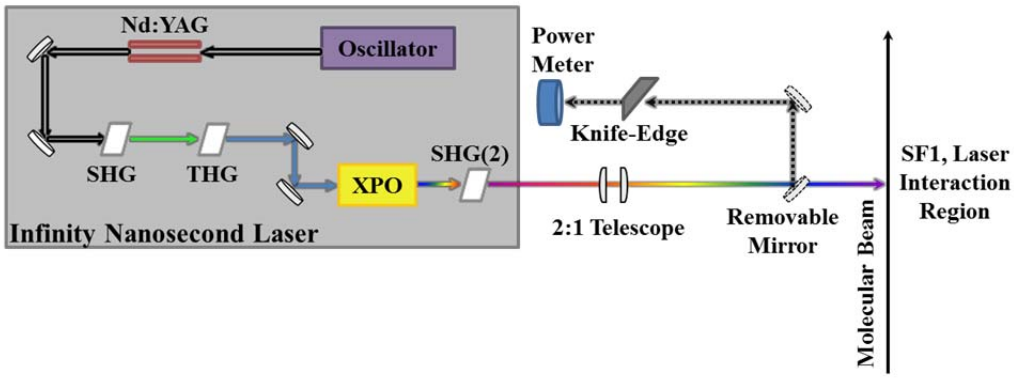

Figure 2.3 Schematic diagram of nanosecond laser system and optical path.

2.5.2 Femtosecond Laser System

A femtosecond laser system, described in detail previously,[36, 53] is utilized in the study of the time-resolved absorption recovery of photodissociated $IBr^-(CO_2)_n$ clusters (Chapter V). Only a brief overview of details relevant to these experiments is presented here.

A Ti:Sapphire oscillator (Coherent Mira Basic) is pumped by a Nd:VO_4 (neodymium-doped vanadium oxide) laser (Coherent Verdi V5, λ = 532 nm) to generate 750–850 nm light at a repetition rate of ~76 MHz. The temporal pulse width of the MIRA output beam is ~85 fs and the pulse energy is ~7–8 nJ. The output of the Mira is then amplified in a Ti:Sapphire regenerative multipass amplifier (Quantronix, Titan). The Titan amplifier is pumped by a Nd:YLF (neodymium-doped yttrium lithium fluoride) laser (Quantronix, model 527 DQ,

λ = 527 nm) to produce 795 nm light (~3 mJ/pulse, bandwidth $\Delta\lambda \approx 10$ nm) at a repetition rate of 400 Hz. The temporal pulse width of the Titan output is measured by optical autocorrelation (INRAD, model 5-14BX) to be roughly 120 fs.

The time-resolved experiments, discussed in Chapter V, are performed with a one-color pump-probe scheme and optical path that utilizes two delay stages, see Fig. 2.4. The 795 nm pump pulse photoexcites $IBr^-(CO_2)_n$ clusters to the $\tilde{A}'\ ^2\Pi_{1/2}$ excited state, on which the chromophore begins to dissociate. Following dissociation of IBr^-, the anionic cluster is transparent to 795 nm light. Only after a solvent-induced nonadiabatic transition to the ground state, vibrational relaxation into the ground state well, and evaporation of solvent CO_2 molecules, the recombined chromophore regains absorption cross section. The probe pulse (at some time delay relative to the pump pulse) then excites the recombined chromophore to the $\tilde{A}'\ ^2\Pi_{1/2}$ excited state. This leads to either dissociation of the chromophore on the $\tilde{A}'$ state into I^--based photoproducts or a second nonadiabatic transition to the ground state and recombination in the ground state well resulting in IBr^--based products. By detecting the total number of two-photon ionic photoproducts, the absorption recovery is measured as a function of pump-probe delay time.

To perform this measurement, the output of the Titan amplifier must be split, utilizing a 50/50 beam splitter, into the pump and probe beams. The pump beam traverses a computer-controlled delay stage (Parker, 008-9129) with a range of 800 ps and time resolution of ~100 fs. The probe beam is directed through an optical rail delay stage with a range of 3.5 ns and a time resolution of ~20 ps. The poor time resolution of the optical rail compared to the computer-controlled delay stage is a result of manual positioning of the stage on the optical rail

to adjust the range of pump-probe delay time. The two delay stages are used in conjunction to allow for both small and large time steps; the computer-controlled delay stage is utilized, with the manual delay at a fixed position, to obtain data for short pump-probe delay and small time intervals. For large pump-probe delay, the position of the delay stage on the optical rail was adjusted, with the computer-controlled delay scanning ±400 ps at each position. After traversing the delay stages, the two halves of the beam are then recombined collinearly in a 50/50 beam combiner, directed through a periscope, and focused using a single lens before entering the TOF MS. The typical laser beam is roughly 1 mm in diameter at the intersection of the anions with the laser, with a pulse energy of ~500 μJ.

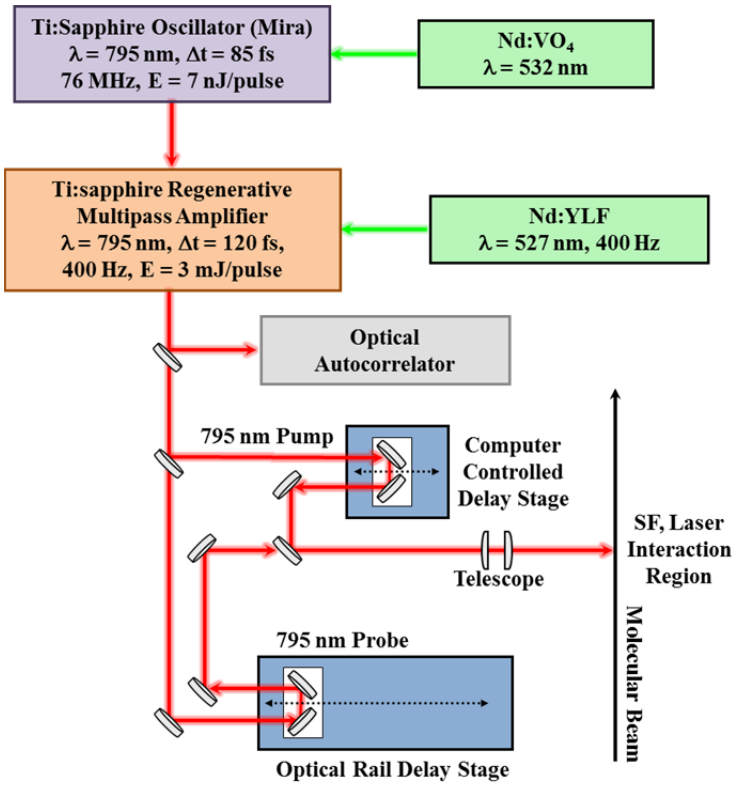

Figure 2.4 Schematic diagram of femtosecond laser system and optical path.

2.6 Data Acquisition

2.6.1 Experimental Timing Sequence

For the experiments presented in this thesis, two to three digital delay generators (Stanford Research Systems, model DG535) are utilized to control the timing sequence of the experiments. When taking data, the master clock is provided to the digital delay generators by the laser system in use. When measuring the ion photoproduct distribution or action cross section for photodissociation of ICN^-, $ICN^-(Ar)$, or $ICN^-(CO_2)$, the Q-switch of the master oscillator in the Infinity nanosecond laser provides the external trigger for the digital delay generators. The trigger in the time-resolved experiments is provided by the pulse train from the Ti:Sapphire oscillator. A portion of the 76 MHz pulse train is continually monitored on a photodiode and the resulting signal is divided to 400 Hz. The 400 Hz signal triggers the Pockels Cell driver (Medox Electro-Optics, model DR85-A), which is utilized to trigger the Titan amplifier and Nd:YLF laser. The 400 Hz output signal from the Pockels Cell driver is further divided by a homebuilt Modulo-N divider to 100 Hz and utilized as the external trigger for the digital delay generators.

Figures 2.5 and 2.6 show a schematic representation of the relative timing sequence for the various experimental components of the static and time-resolved experiments, respectively. For both types of experiments, following the trigger from the lasers, the opening of the pulsed valve is the first in a sequence of events to produce, mass separate, and photoexcite ions. The extraction pulse to extract anions into the TOF MS is the next event to occur. Following extraction, the potential switch is pulsed when the desired ion is in the middle to re-reference the ions to earth ground. The mass gate is pulsed next, allowing for the desired anionic cluster size to

pass through, while deflecting the other ions from the beam axis. Finally, when performing time-resolved experiments, four time-gates, used for the integration of the ionic photoproducts, are triggered. The relative timing for each event in this sequence is varied to optimize the spatial focus of the parent anionic clusters at SF1 (Wiley-McLaren condition) and the temporal overlap of the ion packet and the laser pulses.

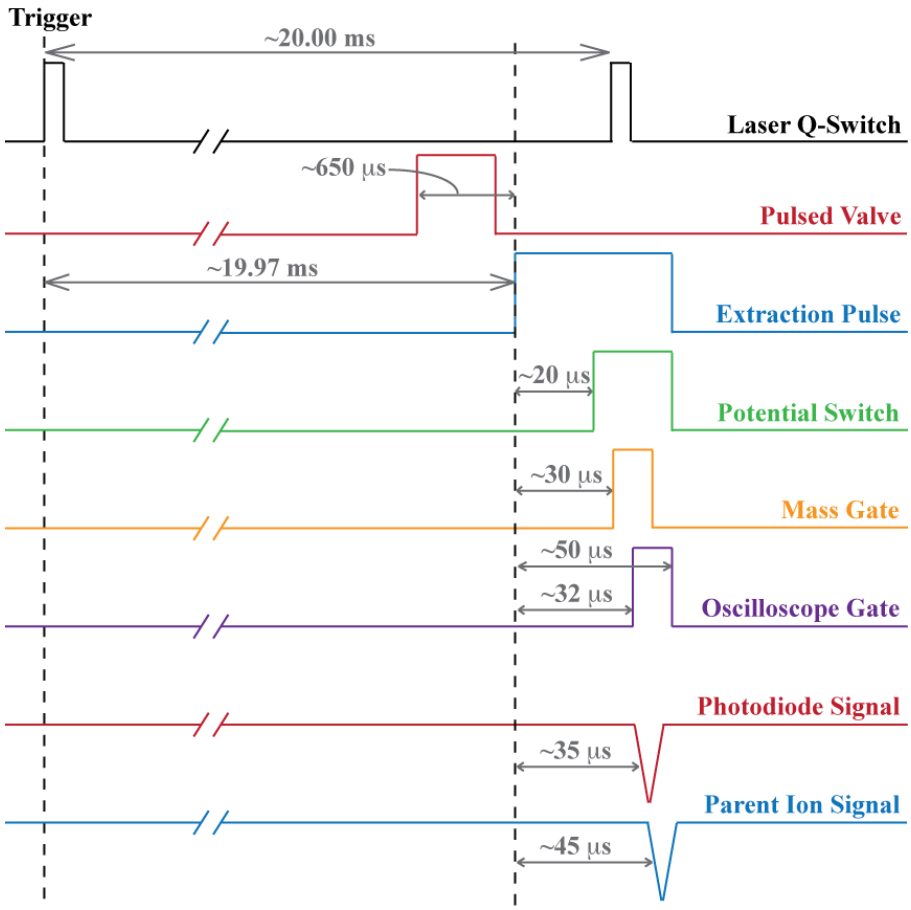

Figure 2.5 Schematic diagram describing the relative timing of the mass spectrometer and nanosecond laser system utilized for static experiments. All delays and pulse widths shown are approximate.

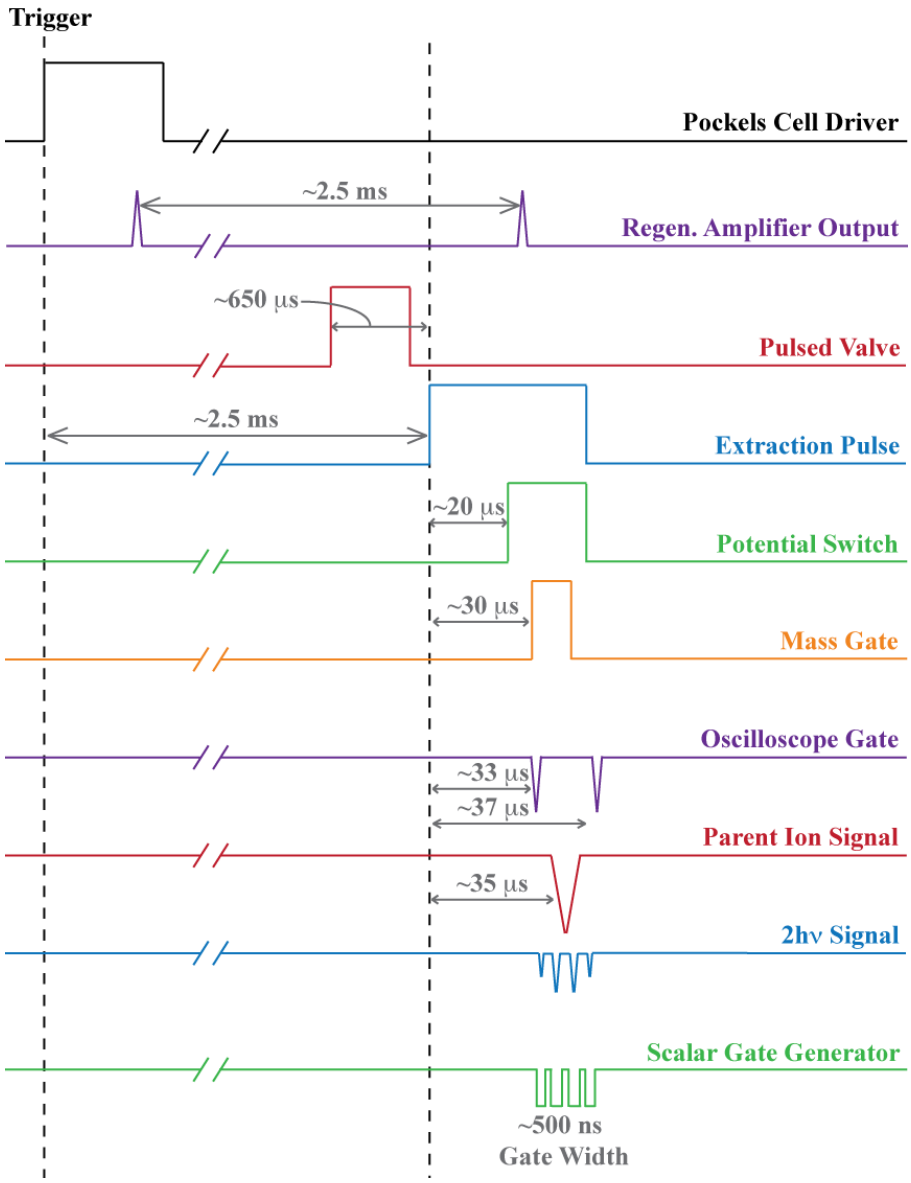

Figure 2.6 Schematic diagram describing the relative timing of the mass spectrometer and femtosecond laser system utilized for time-resolved experiments. All delays and pulse widths shown are approximate.

2.6.2 Data Acquisition Electronics

In order to measure the photoproducts of one or two-photon experiments, the output signal from the collector anode of the off-axis detector is monitored and collected. This output transient signal is capacitively coupled to the data acquisition electronics to isolate the output signal from the high voltage applied to the collector anode. The output signal is amplified by a 10x fast preamplifier (Ortec, model 9301) that is directly connected to the output capacitors. The signal is further amplified by an adjustable gain (1x to 10x) quad bipolar amplifier (Phillips Scientific, model 771) set to scale the signal by a factor of ten. The subsequent data acquisition methods, presented below, are different for the two types of experiments described in this thesis.

2.6.3 Data Acquisition for Static Photofragmentation Experiments

For the static photofragmentation experiments, the amplified photoproduct signal is monitored on an oscilloscope (Tektronix, model DPO 2024) to allow for optimization of the ion intensities. Two measurements (described below) are performed in the static experiments: the measurement of the ionic photoproduct distributions following photoexcitation of a parent anionic cluster and the *relative* action cross section for photodissociation of ICN^-, $ICN^-(Ar)$, and $ICN^-(CO_2)$.

2.6.3.1 Ionic Photoproduct Distributions

The significance of photofragmentation dynamics occurring on a single or multiple excited states following excitation of a chromophore is elucidated by the ionic photoproduct distributions as a function of wavelength and cluster size. To distinguish between ionic

photoproducts, the electric potential on reflectron is adjusted to focus the desired ionic photoproduct, *i,* on the off-axis MCP detector.

The ionic photoproduct distributions are obtained by measuring the production of mass-selected ionic photofragments following excitation and fragmentation of parent anionic clusters. Optimization of the temporal overlap of the ion packets with the laser pulses is performed by adjusting the laser timing with respect to the extraction timing (Fig. 2.5); during a data set, the laser timing is not adjusted. Additionally, a manually-activated shutter (Uniblitz, model VS14S2TO) is utilized to block the laser beam to allow for background subtraction. A minimum of ten data sets are collected to reduce statistical fluctuations and systematic effects. The spectrum of the ionic photoproduct *i* is averaged over all data sets, integrated, and divided by the sum of all observed ionic photofragment average peak areas. This yields the final ratio for ionic photoproduct *i* from the photofragmentation of one parent cluster size. Laser power dependence studies on the production of ionic photoproducts following photofragmentation of a parent cluster are performed to ensure the measured ionic photoproduct distribution results entirely from one-photon photodissociation. Following the analysis of ten data sets, the typical statistical errors in the ionic photoproduct distribution are about 5%.

2.6.3.2 Action Cross Section for Photodissociation of an Anionic Chromophore

The measurement of an *absolute* cross section necessitates determining the same quantities as the *relative* cross section, with the addition of the spatial overlap of the laser pulse and ion packet, and the detection efficiency of the off-axis MCP detector. However, because of the difficulty in measuring the ion-laser spatial overlap and detection efficiencies neither of these factors is measured. Therefore, the cross section data presented in this thesis are *relative* cross

sections for the production of ionic photoproduct *i*. Action spectroscopic techniques are utilized to measure the *relative* photodissociation cross section by monitoring the production of a selected ionic photoproduct *i*, the parent ion signal with no laser interaction, and the laser fluence.

For each ionic photoproduct *i*, the average total peak area, $\bar{I}_{Fi}$, on the off-axis detector as a function of wavelength is determined by

$$\bar{I}_{Fi} = \Phi \bar{I}_P \sigma_{i,rel}(\lambda)\chi, \tag{2.3}$$

where Φ is the fluence of photons per laser pulse (in photons/pulse*cm^2), $\bar{I}_P$ is the average total precursor anion peak area on the off-axis with the laser blocked, and χ is the product of the unmeasured spatial overlap and detection efficiency. The fluence of photons per laser pulse is given by

$$\Phi = \frac{E_{laser}}{h\nu A_{laser}}, \tag{2.4}$$

where E_{laser} is the measured pulse energy of the laser, *h* is Planck's constant, ν is the frequency of the laser light, and A_{laser} is the cross-sectional area of the laser beam at the ion-laser interaction. The peak area of *i*, $I_{Fi,jk}$, for a single laser pulse *j* and data set *k* ($k \geq 10$) is roughly equivalent to $\bar{I}_{Fi}$ when summed over 128 laser pulses at 50 Hz. Therefore, the *relative* cross section for the production of *i* as a function of excitation wavelength summed over all laser pulses and data sets is determined by

$$\sigma_{i,rel}(\lambda) = \frac{1}{10}\sum_{k=1}^{10}\left(\frac{1}{\Phi}\right)\frac{\sum_{j=1}^{128} I_{Fi,jk}}{\sum_{j=1}^{128} I_{P,jk}}\chi, \tag{2.5}$$

where χ is assumed to be unity. A minimum of ten data sets is measured to reduce statistical fluctuations and systematic effects. Typical statistical fluctuations in the *relative* cross section measurements are roughly 5-15%.

2.6.4 Data Acquisition for Time-Resolved Experiments

Figure 2.7 shows a schematic of the data acquisition system used for the time-resolved experiments. Following amplification of the signal from the off-axis MCP detector, the resulting signal is split by a splitter (Minicircuits, model ZSC-2-2); one half of the signal is monitored on an oscilloscope (Tektronix, model DPO 2024) and the other half is input into a 300 MHz discriminator (Phillips Scientific, model 6904). The discriminator threshold is set to ~0.150 V, which separates of the ion signal from the detector noise. From the discriminator, the signal proceeds to a quad scalar (DSP, model QS-450), which counts the pulses associated with ionic products that impinge upon the MCPs within one of four adjustable time-gates. The position of the time-gates is controlled by a digital delay generator (Stanford Research Systems, model DG535) and set to open during the arrival times of the desired photoproducts. A computer, run in MS-DOS (Microsoft Disk Operating System), then obtains the signal from the quad scalar through a GPIB (General Purpose Interface Bus) crate controller (DSP, model 6001) that is interfaced with a CAMAC crate (Kinetic Systems, model 1510-P2C), in which the quad scalar is held.

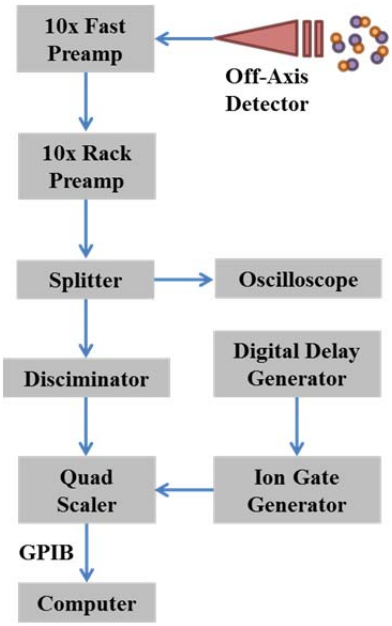

Figure 2.7 Schematic diagram of the data acquisition system utilized for time-resolved experiments.

2.6.4.1 Time-Resolved Absorption Recovery Measurements

The time-resolved absorption recovery data for photodissociated $IBr^{-}(CO_2)_n$ clusters are collected by scanning a selected set of pump-probe time delays; the procedure utilized is detailed elsewhere[54] and only a brief description is reported here. One scan sweeps the time-delay range, collecting data for 1000 laser shots per time delay, until all selected time delays are sampled. Typically, the pump-probe delays are stepped by roughly 20–100 ps for small pump-probe delays and roughly 500 ps for large delays. Scans are repeated, in both the forward and backward scanning direction, until data for roughly $5x10^4$ laser shots per time delay is collected. To allow for background subtraction to obtain the two-photon time-dependent signal, baseline traces from the pump and probe laser beams are obtained by a series of measurements with computer-controlled shutters in the open and closed positions. This also enables analysis of the

contribution of the pump and the probe beams to the ionic photoproduct signal. The number of photoproducts detected per laser pulse is dependent on the size of the parent cluster anion, but typical two-photon signals range from 1–4 photoproducts per laser shot.

Chapter III: Photodissociation of $ICN^-(Ar)_n$

3.1 Introduction

This chapter describes experimental studies[40] of the dissociation/recombination dynamics of $ICN^-(Ar)_n$, n = 0–5, following photoexcitation to the dissociative $^2\Pi_{1/2}$ state. The ICN molecule is a prototype for the study of dynamics at conical intersections.[55-63] Trajectory calculations run on high-level potential energy surfaces[64, 65] established that bending motion, which occurs along with the I–CN bond elongation, maps into torque on the CN diatom as ICN passes through a conical intersection, giving the notably high degree of rotational excitation observed in concurrence with I ($^2P_{3/2}$). In the absence of a conical intersection, as is the case for ICN^- photodissociation, the shape of the excited-state potential energy surface still plays a large role in the rotational state distribution of the photofragments. This chapter focuses on the role of the CN fragment rotation in the dynamics of photoexcited ICN^- with and without Ar solvation. Figure 3.1 sketches potential energy curves adapted from Ref. 66 for the electronic ground state of the ICN^- and INC^- isomers ($^2\Sigma^+$, black) and the first optically accessible excited state of these isomers ($^2\Pi_{1/2}$, purple). Figure 3.1 also depicts photoexcitation of ground-state ICN^-, which undergoes dissociation (3.1) through the following channels:

$$ICN^-(Ar)_n + h\nu \rightarrow ICN^-(Ar)_{m<n} + (n-m)Ar \qquad (3.1a)$$

$$\rightarrow I^-(Ar)_{k\leq n} + CN + (n-k)Ar \qquad (3.1b)$$

$$\rightarrow CN^- + I + nAr \qquad (3.1c).$$

Beyond the photodissociation products observed following excitation of previous dihalides[33-35] to the $^2\Pi_{1/2}$ excited state, the addition of a single Ar atom (which is only bound by ~50 meV (Ref. 67)) results in the formation of recombined ICN^-. Experimental and theoretical evidence suggests a large amount of internal energy must be deposited into the neutral or anion product. For the photon energies used in these experiments, most of the excess energy is in the I–C bond. Energy transfer between the low-frequency I–C stretch and the high-frequency C–N stretch will be inefficient. Furthermore, quantum dynamics calculations indicate quick and efficient energy transfer into CN rotation following photoexcitation. Thus, it is likely that CN rotation plays a vital role in storing considerable amounts of internal energy.

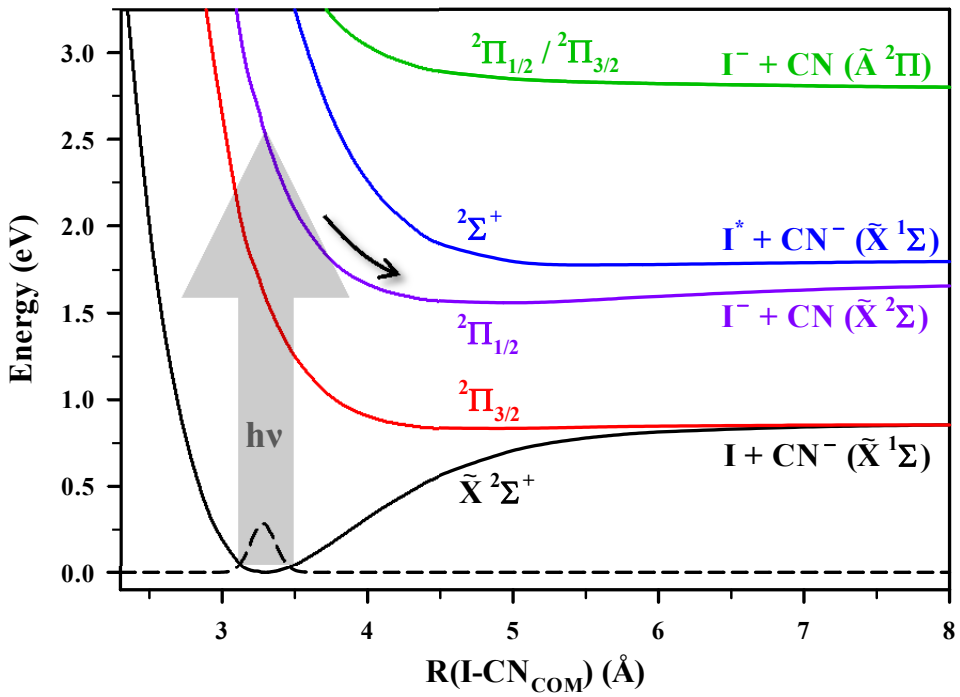

Figure 3.1 Schematic potential energy curves (based on Ref. 66) for the ICN^- ($^2\Sigma^+$ in black and $^2\Pi_{1/2}$ in purple) as a function of the I–CN center of mass distance. The black dashed line shows the probability amplitude of the ground-state wave function for ICN^-. The black arrow illustrates photoexcitation and subsequent dissociation (3.1).

3.2 Experimental

This section presents an overview of the experimental methods utilized in this study; only relevant details, beyond those presented in Chapter II, are provided. Solid ICN is synthesized using the procedure reported by Bak and Hillebert.[42] Neat Ar (20–30 psig) passes over solid ICN and then expands from a 0.8-mm orifice of a pulsed General Valve nozzle into the ion-source chamber. The neutral molecular beam encounters a focused and magnetically-guided 1-keV electron beam, forming a variety of anions. A pulsed extraction field, the first component of the Wiley-McLaren[41] time-of-flight mass spectrometer (TOF MS), extracts the anions into the TOF MS, where they separated by their mass-to-charge ratio. While in the TOF MS, a fast potential switch[49] re-references the anions to an earth ground and an einzel lens focuses the anions into the interaction region.

A mass gate located just prior to the anion spatial focus selects the desired anion, allowing only this single species to continue into the interaction region. The output of a Nd:YAG-pumped optical parametric oscillator (OPO) is collimated into the interaction region. Both the surviving parent anions and the photodissociation products (neutral and anionic components) generated from the ion-light interaction enter a single-stage secondary reflectron mass spectrometer. The neutral photoproducts continue through the reflectron unperturbed. The reflectron separates the anionic photoproducts by mass and directs them toward a dual set of microchannel plates (MCPs) located 8° off-axis of the parent-ion beam. Changing the reflectron potential allows different product anion masses to impinge upon the detector; a recording oscilloscope collects the signal from the detector for various reflectron potentials, thereby

permitting a determination of the ion photoproduct distribution and photodissociation cross section, as detailed in Chapter II.

It is also critically important to note that the observed ionic fragments are fragments that have remained in their detected form from the time of photodissociation through the time that they are detected. While this time could be calculated for each photoproduct, it is adequate to note that it is ~10 μs for all of the products discussed here. Thus, e.g., when recombined photoproducts are observed, the observation only implies stability on a 10 μs time scale, **not** absolute stability.

3.3 Theoretical Methods

Initial one-dimensional ICN^- electronic structure calculations of the ground and valence excited states were carried out by the author,[40] in collaboration with Professor Anne McCoy and have been detailed elsewhere.[66] Further investigations showed that in order to describe adequately the photodissociation process, it would be essential to increase the dimensionality to include large amplitude bending motions. This was done and the ICN^- electronic structure was obtained as a function of two Jacobi coordinates, R and θ.[66] In this context, R is the distance between the iodine atom and the center-of-mass of the CN diatom and θ is the angle between the vector $\boldsymbol{R}$ and the CN bond. As excitation of CN vibrations are not expected in the photodissociation process reported in this thesis, it was acceptable to constrain the CN bond length (r) to its v = 0 value, 1.16 Å. We define $\theta = 0°$ to be the linear ICN^- configuration and the INC^- configuration then corresponds to $\theta = 180°$. Thus the $\theta = 0°$ limit of this calculation corresponds to the one-dimensional calculations mentioned above.

We display the resulting $\tilde{X}\ ^2\Sigma^+$ and $^2\Pi_{1/2}$ surfaces in Figure 3.2, plotted as functions of the two Jacobi coordinates described above. As can be seen, the $^2\Pi_{1/2}$ state has a shallow minimum at a slightly bent geometry. Analysis of the potential energy surface for this state shows that it is bound by 0.27 eV, relative to the dissociated products, and that this minimum occurs at $R = 4.74$ Å and $\theta = 24°$.

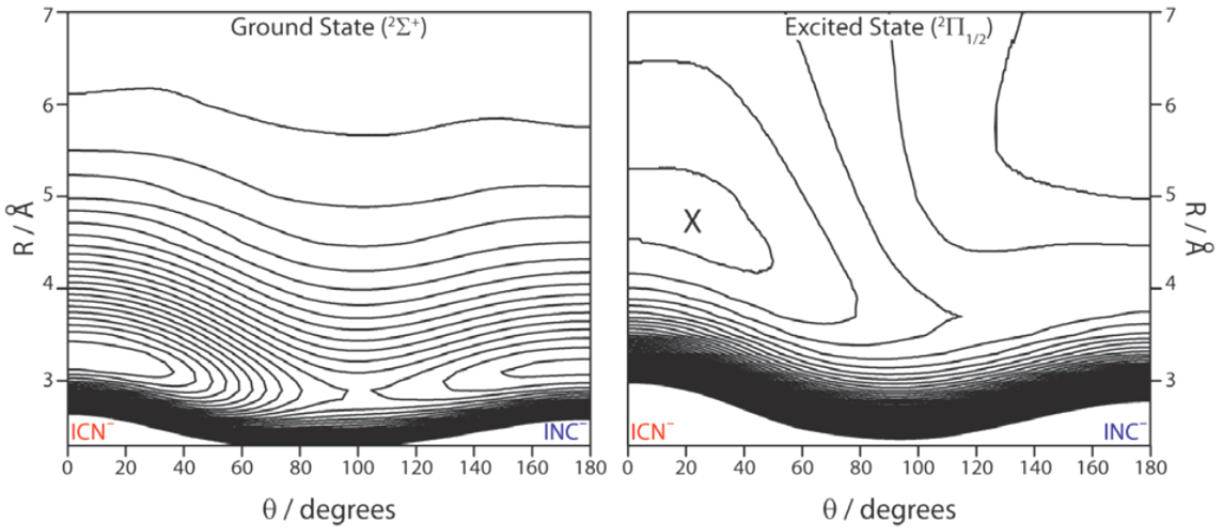

Figure 3.2 Two-dimensional contour plots of the ground ($^2\Sigma^+$) and excited ($^2\Pi_{1/2}$) states of ICN^-; contour lines are shown every 0.05 eV. The X denotes the location of the shallow minimum of the $^2\Pi_{1/2}$ potential (Ref. 66)

To explore the energy partitioning following 500 nm excitation of ICN^- to the dissociative $^2\Pi_{1/2}$ state, we propagate eigenstates of the ground-state surface on this excited-state potential. Based on the potential energy surfaces shown in Figure 3.2, the ground-state vibrational wave is obtained using the approaches described in Ref 66. For these calculations, the Hamiltonian is

$$\hat{H} = \hat{T}_{trans} + \hat{T}_{rot} + V(R, \theta),$$

where

$$\hat{T}_{trans} = -\frac{\hbar}{2\mu_{I\ldots CN}}\frac{\partial}{\partial R^2},$$

and

$$\hat{T}_{rot} = \left[\frac{1}{2\mu_{I\ldots CN}R^2} + \frac{1}{2\mu_{CN}\,r^2}\right]\left(\hat{J}^2 + \hat{j}^2 - 2\hat{J}_z^2\right),$$

and $V(R, \theta)$ represents the potential energy for the $^2\Pi_{1/2}$ state. For the purpose of the analysis, the average potential energy at the end of the calculation is defined to be zero. The masses represent the reduced mass, μ, of I–CN and CN. In these calculations, we set $J = M = 0$ for calculations of states with even quanta in the bend and $J = M = 1$ for calculations involving states with odd quanta in the bend. Here J represents the total angular momentum of the ICN^- molecule, while M gives its projection onto R.

The calculations use 1000 evenly spaced grid points in R, ranging from 2 to 50 a_0 (1.06–26.5 Å), and 75 grid points in θ, which are based on the zero's in the Legendre polynomial with $l - m = 75$ (with $m = 0$ for even quanta in the bend and $m = 1$ for odd quanta in the bend). Again, the CN bond length is held constant at 1.16 Å. At $t = 0$, the wave function for the state of interest is promoted to the $^2\Pi_{1/2}$ excited-state potential, and the dynamics are followed as a function of time. We propagate the dynamics using a Lanczos scheme with 20 iterations for each 25 au time step. The approach is similar to that employed in an earlier study of $Cu(H_2O)$.[68] We test the parameters to ensure convergence of the calculations for the 1000 time steps over which the results are reported.

3.4 Experimental Results: Photodissociation of $ICN^-(Ar)_{0–5}$

The cross sections for the production of I^- and CN^- following photoexcitation of ICN^-, along with the results of 500 nm photodissociation of $ICN^-(Ar)_n$ (n = 1–5), are given below.[40] Argon was chosen as the solvent because of the weak electrostatic interactions it shares with the solute and with other Ar atoms. The short-range, ion-induced dipole interaction between Ar and the ICN^- chromophore results in an Ar solvation energy[67] of ~0.05 eV and is not expected to lead to significant perturbations of the ICN^- electronic structure. Additionally, Ar–Ar interactions are only slightly attractive and result in a loose cage around the chromophore, which is not anticipated to lead to high yields of caged photoproducts for the small (0–5) numbers of Ar solvent molecules studied. Comparing the results of $ICN^-(Ar)_n$ photodissociation with previous dihalide results elucidates the role of the additional degrees of freedom available for ICN^- and its photoproducts.

3.4.1 *Relative* Action Cross Section for Photodissociation of ICN^-

The experimental *relative* cross sections ($\sigma_{rel}(\lambda)$) for the production of I^- and CN^- products following 430 to 650 nm excitation of the ICN^- chromophore are shown in Fig. 3.3. This spectral region corresponds to excitation to the $^2\Pi_{1/2}$ state which results in two dissociation channels: $ICN^- \longrightarrow I^- + CN$ (97%) and $ICN^- \longrightarrow I + CN^-$ (3%). The peak of the I^- spectrum is near 490 nm and the full-width-at-half-maximum (FWHM) is ~0.31 eV. Similar experiments were performed following photoexcitation of $ICN^-(Ar)_n$. As expected, because of the weak solvent-solute interaction, solvation of ICN^- with one Ar atom does not lead to a significant change in the cross section for the production of ionic photoproducts.

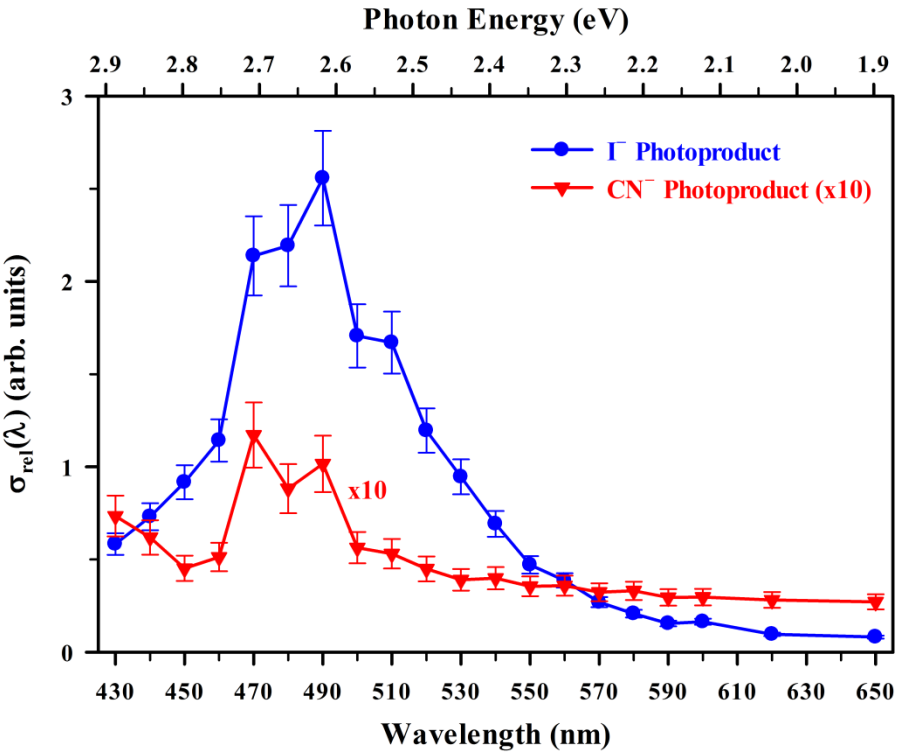

Figure 3.3 Cross sections ($\sigma_{rel}(\lambda)$) for the production of I^- (blue circles) and CN^- (red triangles, x10) photoproducts following 430 to 650 nm photodissociation of ICN^-.

3.4.2 Anionic Photoproduct Distributions

Studies of the photodissociation product distributions of mass-selected $ICN^-(Ar)_{1\text{-}5}$ following 500 nm excitation to the $^2\Pi_{1/2}$ electronic-excited state of ICN^- show that I^--based products dominate for all cluster sizes. For example, $I^-(Ar)$ and $I^-(Ar)_2$ are by far the most abundant products of $ICN^-(Ar)_2$ photodissociation. Figure 3.4 shows the degree of Ar solvation of the I^-- and ICN^--based products ($I^-(Ar)_m$ and $ICN^-(Ar)_m$), plotted as a function of the number of Ar atoms in the parent $ICN^-(Ar)_n$. Both an unexpectedly large solvent retention and recombination with a single Ar solvent are observed. From these two plots in Figure 3.4, it is apparent that the product distributions are in stark contrast to previous studies on dihalides,[33-36, 69]

where the solvent loss from caged products follows the evaporative ensemble model, in which excess energy rapidly results in the loss of neutral solvent.[70] This result unequivocally demonstrates that the large amount of energy released following photodissociation is not completely converted into evaporation of the weakly bound Ar, but instead must remain in internal degrees of freedom of the I^- and CN or, if recombination occurs, ICN^-.

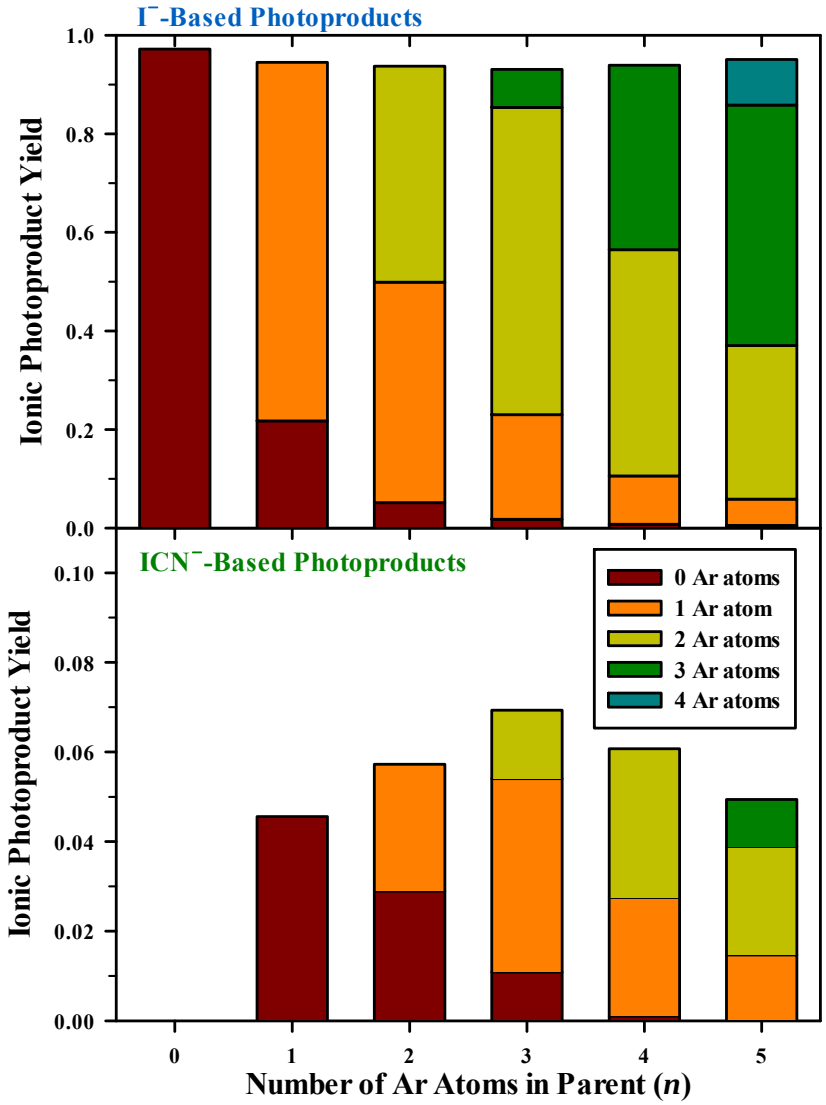

Figure 3.4 Solvation breakdown for I^-- and ICN^--based photoproducts following 2.5 eV excitation of $ICN^-(Ar)_n$. The color of the bar corresponds to the number of Ar atoms in the ionic photoproduct. Note the change in scale of the y-axis between the two plots.

The photodissociation studies also find a roughly 6% recombination yield for $ICN^-(Ar)$. Cage recombination for a single Ar solvent is particularly surprising, especially with such a weakly bound solvent. Moreover, the observation that the cage fraction depends very weakly on n for $1 \leq n \leq 5$ strongly indicates that a single, labile Ar is critical for cage recombination in this

size range. The Ar–ICN^- potential is relatively isotropic, allowing the Ar to sample large regions of configuration space about the chromophore. This leads to an occasional collision between the Ar and the departing CN fragment, the kinematics of which are described below. Recombination to stable ICN^- products cannot occur on a dissociative state. Yet, the ICN^- photoproduct survives for at least 10 μs after photoexcitation, indicating that substantial energy is stored in the molecular ion for a long period of time. The weak binding energy of the Ar solvent (~0.05 eV) is insufficient to bridge the large energy separation between the $^2\Pi_{1/2}$ state and the bound ground state (ΔE = 0.80 eV). While, *ab initio* calculations do find a shallow (~0.27 eV) potential well on the $^2\Pi_{1/2}$ surface of ICN^-,[66] the only way that recombined anions can be trapped on the excited $^2\Pi_{1/2}$ surface is for a large fraction of the available energy to be tied up in rotation of the CN diatom, forming a complex between the I^- and the *trapped, quasi-free rotor* CN diatom (B_e(CN) = 1.89974 cm^{-1}).[71, 72] This [I^-–CN] complex formation allows sufficient time for radiative decay back to the ground state, resulting in a bound (but with significant internal excitation) ground state ICN^- photodissociation product.

3.4.3 Kinematics of Collinear ICN^-(Ar) Dissociation

A simple hard-sphere, center-of-mass frame model that only considers translational degrees of freedom is used to describe the kinematics of dissociation for ICN^-(Ar). The photodissociation of ICN^- and the elastic collision of the CN fragment with the Ar atom are considered as two separate actions. Additionally, the collision is only evaluated in a collinear geometry. Accordingly, the numbers given in this section represent the maximum translational energy transfer to the Ar atom.

Photodissociation of the ICN^- initiated with a 500 nm photon produces I^- and ground-state CN, leaving 0.87 eV of available energy to be partitioned into the products. (This excess energy is obtained by taking the difference between the photon energy and the experimentally determined $D_0(I–CN^-) = 0.83$ eV (Ref. 67) and $EA(CN) - EA(I) = 0.80$ eV).[73, 74] This simple kinematic model finds that 0.15 eV and 0.72 eV of energy distributes into translation of I^- and CN, respectively. The subsequent CN–Ar collision further divides the 0.72 eV of CN translation energy into 0.44 eV and 0.28 eV of energy for translation of the CN and Ar, respectively. This model results in roughly one third of the translational energy available to the three species (I^-, CN, and Ar) leaving with the Ar atom. By obtaining the potential energy of the I^-–CN system from the sum of $D_0(I–CN^-)$ and $[EA(CN) - EA(I)]$, we determine the amount of translational energy available to the dissociation products and, thus, the energy transfer between the CN fragment and Ar atom, at an infinite I^-–CN separation.

Although the ICN^-–Ar potential is rather flat, the Ar atom is located roughly 3.5 Å beyond the N atom of the ICN^- chromophore. As a result, it is likely that the CN–Ar collision will occur at a I^-–CN separation of roughly 4.5 Å. To consider the quantity of energy that leaves with the Ar atom for finite I^-–CN separations, we use a 1D potential patterned after the calculated $^2\Pi_{1/2}$ potential to approximate the translation energy available to the dissociating ICN^- for varying I^-–CN separations. The results of these calculations are given in Table 3.1; $R_{I–CN}$ is the distance between the iodine atom and the center of mass of the CN diatom, E_{avail} is the amount of energy that becomes available for translation of the fragments, and E_t is the translational energy that is partitioned into the given fragment. The translational energies are broken into pre- and post-collision energies, representing the energy deposited into the I^- and CN

fragments from the dissociation and then the transfer of energy from the CN fragment to the Ar atom upon collision.

Table 3.1 Translational energy partitioning as a function of the assumed I–CN separation at the time of collision of CN with Ar, as determined from a simple kinematic analysis.

		Pre-Collision Energies (eV)			**Post-Collision Energies (eV)**		
$\boldsymbol{R_{I–CN}}$ **(Å)**	E_{avail} (eV)	$E_t(I^-)$	E_t(CN)	E_t(Ar)	$E_t(I^-)$	E_t(CN)	E_t(Ar)
3.27	0.00	0.00	0.00	0.00	0.00	0.00	0.00
4.50	1.02	0.17	0.85	0.00	0.17	0.51	0.33
9.00	0.87	0.15	0.72	0.00	0.15	0.44	0.28

At an I^-–CN separation of 4.5 Å (approximately the separation for which the CN fragment will collide with the Ar atom), the available energy is 1.02 eV. Figure 3.5 is a schematic of the photodissociation of ICN^-(Ar) and the subsequent collision between the CN diatom and the collinear, solvent Ar atom. From this simple kinematic model, we find that the departing Ar removes 0.33 eV of energy *via* translation and another 0.05 eV is expended to break the ICN^-–Ar bond. There is an additional loss of 0.03 eV as the CN fragment changes its trajectory following the collision with Ar and the center of mass of the ICN^- begins to translate (see Fig. 3.5). This leaves the I^-–CN system with 0.61 eV of energy unaccounted for on an excited-state surface ($^2\Pi_{1/2}$) that contains a 0.27 eV potential well. For this simplified model, the amount of energy that is left in the I^-–CN system implies that dissociation will be rapid. This rapid dissociation leaves no opportunity for a radiative transition back to the ICN^- ground state, which is essential to undergo recombination. As such, it is apparent that the energy partitioned to the rotation of the CN fragment is crucial to the observation of recombined ICN^- from ICN^-(Ar).

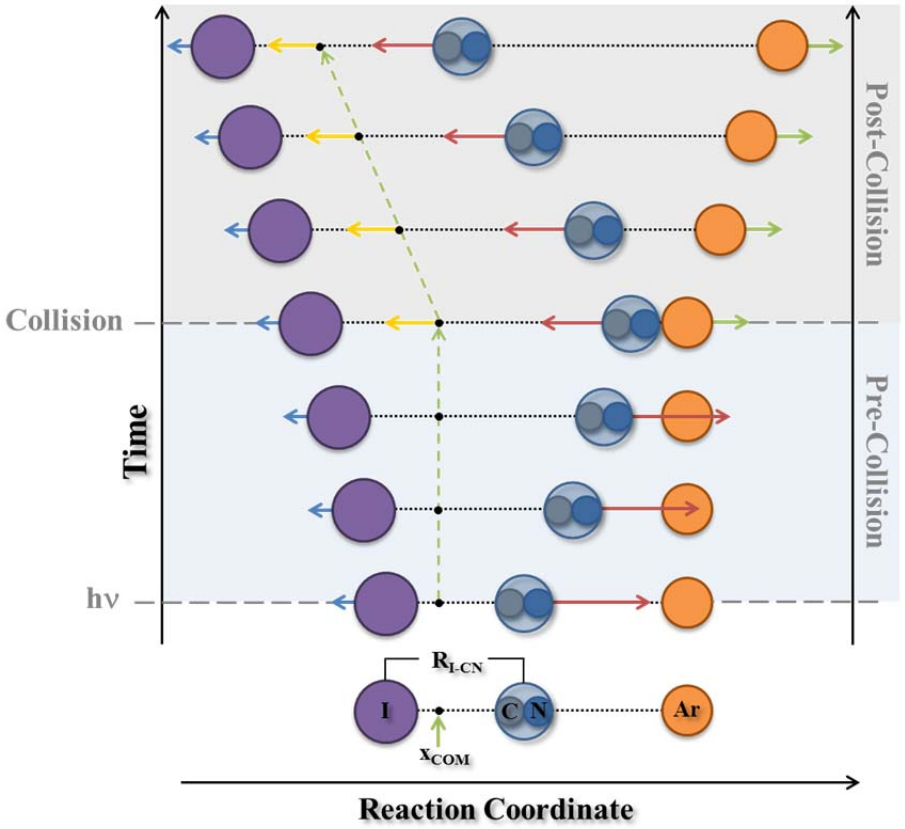

Figure 3.5 Schematic diagram of the photodissociation of ICN^-(Ar) and the subsequent collision between CN and the solvent Ar atom. The bottom ICN^-(Ar) cluster defines the atoms, the center-of-mass of ICN^-, X_{COM}, and the distance between the iodine and the center-of-mass of the CN diatom, $R_{I–CN}$. The CN diatom is assumed to be a hard sphere with a radius of 1.16 Å, the calculated bond length of CN. The arrows indicate the direction of the hard-sphere's trajectory and the time at which photodissociation and the collision occur is indicated on the left axis. Additionally, the time range for the pre-collision (light blue shading) and post-collision (light gray shading) energy values in Table 3.1 are shown on the right.

3.4.4 Quantum Dynamics

Additional evidence for the importance of the *free* internal rotation of the CN diatom in $[I^-–CN]$ comes from quantum dynamics calculations of the photodissociation of bare ICN^- on the $^2\Pi_{1/2}$ potential energy surface.[40] Promoting the rovibronic ground-state wave function ($J_{tot} = 0$) for the anion onto the $^2\Pi_{1/2}$ surface results in an increase in the I–CN distance

(*R* coordinate) due to the dissociative nature of the excited state. The calculations also show that the wave function spreads quickly along the CN rotational degree of freedom (θ coordinate). The anisotropy of the $^2\Pi_{1/2}$ potential efficiently couples *R* and θ, allowing the excited ICN^- to explore both internal coordinates as it dissociates. As illustrated in Figure 3.6, at $t = 0$ the wave function only has amplitude for values of θ less than 50°; however, by 180 fs the wave function has amplitude over all I–CN bend angles, effectively making the CN diatom a free rotor ($B_e(CN) = 1.89974\ cm^{-1}$).[71, 72] After 360 fs, the I–CN separation has increased to ~12 Å, and essentially all CN orientations are equally probable. The calculations also show that ~20% of the available energy is partitioned into the CN diatom rotation; furthermore, this fraction increases with initial bend excitation. Additional calculations, artificially altering the time scale of the CN rotation with respect to the ICN^- dissociation, illustrate that the longer CN samples the anisotropic portions of the potential energy surface, the more energy will go into rotation.

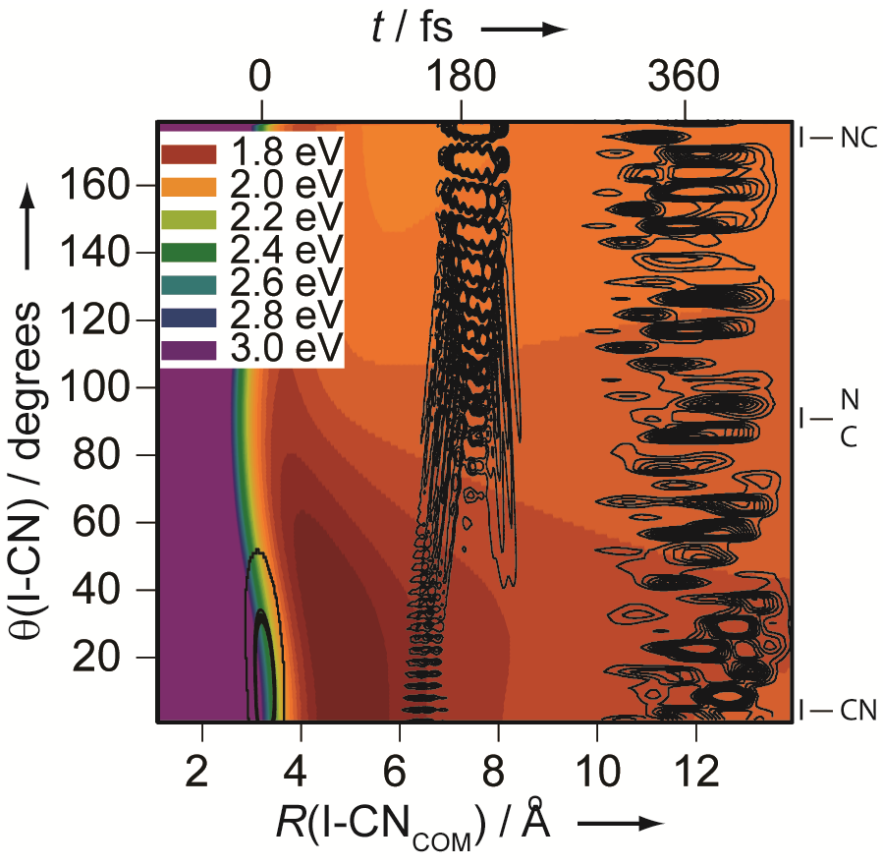

Figure 3.6 Quantum dynamics calculation results for $t = 0$, 180 and 360 fs following promotion of the ICN^- $^2\Sigma^+$ rovibronic ground-state wave function ($J_{tot} = 0$) to the $^2\Pi_{1/2}$ surface. The probability amplitude (black contours) is shown on the $^2\Pi_{1/2}$ potential energy surface (color) as a function of the Jacobi coordinates, R and θ.

Photodissociation of ICN^- on the $^2\Pi_{1/2}$ surface produces I^- and ground-state CN, leaving 0.87 eV of kinetic energy to be partitioned into the products. In the analysis of the dispersal of this kinetic energy, we focus on the expectation values of the three operators that make up the Hamiltonian. Thus at $t = 600$ fs ($\langle R \rangle = 18.1$ Å), of the 0.87 eV of kinetic energy, 19% or 0.17 eV is in CN rotation; the remaining 0.71 eV is in translation. The time when $\langle V \rangle$ is a minimum, $t = 45$ fs, gives $\langle R \rangle = 4.1$ Å , $\langle T_{trans} \rangle = 0.77$ eV and $\langle T_{rot} \rangle = 0.25$ eV. This corresponds to the propagation time for which the $\langle V \rangle$ is minimized.

To elucidate the mechanism for the substantial energy deposited into CN rotational motion, we repeat the wave packet propagation but change the mass of the iodine atom to that of a hydrogen atom. This change in mass leads to a much more rapid dissociation of the ICN^- relative to the timescale for CN rotation. As a result, the CN does not have the opportunity to sample the anisotropic portions of the potential energy surface and a smaller fraction of the kinetic energy ultimately appears in CN rotation (1% when $\langle R \rangle$ = 18 Å). Likewise in another propagation, the CN rotation is made fast relative to the timescale of the ICN^- dissociation by changing the reduced mass of the CN fragment to that obtained for a carbon and nitrogen each having the mass of hydrogen; thereby increasing the rotational constant for the CN diatom by roughly a factor of 20. This modification has the effect of allowing the CN to more fully sample the anisotropy of the potential energy surface as the ICN^- dissociates, and as a result, there is a larger fraction of the kinetic energy in CN rotation (70% of the kinetic energy). For this calculation, we do not alter the mass of the fragmenting partners for the determination of the translational energy. Furthermore, for both of these calculations, the initial wave packet and the potential energy surfaces are the same as for the true ICN^- simulations. Based on these results, we conclude that the large degree of rotational excitation in the CN fragment following photoexcitation to the $^2\Pi_{1/2}$ excited state reflects the anisotropy of the repulsive wall and the relatively slow dissociation of ICN^-.

An important characteristic of ground-state ICN^- is a very low frequency, 70 cm^{-1} bend vibration, arising in part from the very weak I–CN bond.[66] At the temperature of the experiment (see Chapter II Sec. 2.2), there will be significant population in the ICN^- bend states. Not surprisingly, additional excitation in this mode will lead to a larger fraction of the excess energy being partitioned into CN rotation. Thus, $\langle T_{rot} \rangle$ exceeds 0.3 eV when the initial anion vibrational

wave packet is prepared with one quantum of excitation in the bend. In Table 3.2, we list the expectation values of the three terms that comprise the Hamiltonian for a variety of energetically accessible initial states of ICN^-. We use ν_b to denote the number of quanta in the ICN bend, and ν_s for the number of quanta in the I–CN stretch. The results are analyzed at the initial excitation (top), at the point where $\langle V \rangle$ is minimized (middle), and after 600 fs (bottom). Note that these energies are averages based on the wave packet, and tails of the distribution will have more or less energy in rotation or translation.

Table 3.2 Energy decomposition for a variety of initial states, following excitation to the $^2\Pi_{1/2}$ state. The various components of the energy are expectation values of the three terms in the Hamiltonian.

State (ν_b, ν_s)	Time (fs)	$\langle R \rangle$ (Å)	$\langle V \rangle$ (eV)	$\langle T_{trans} \rangle$ (eV)	$\langle T_{rot} \rangle$ (eV)
Initial Excitation					
(0, 0)	0	3.25	0.87	≤ 0.01	≤ 0.01
Region Near Potential Minimum					
(0, 0)	45	4.10	−0.14	0.77	0.25
(1, 0)	40	3.91	−0.13	0.65	0.36
(2, 0)	41	3.91	−0.11	0.64	0.34
(3, 0)	40	3.85	−0.12	0.59	0.38
(4, 0)	40	3.86	−0.11	0.59	0.37
(0, 1)	46	4.11	−0.14	0.79	0.23
Asymptotic Region					
(0, 0)	600	18.08	0.00	0.71	0.17
(1, 0)	600	16.50	0.00	0.57	0.30
(2, 0)	600	16.11	0.00	0.54	0.33
(3, 0)	600	15.60	0.00	0.50	0.36
(4, 0)	600	15.36	0.00	0.48	0.37
(0, 1)	600	18.02	0.00	0.74	0.15

From the quantum dynamics calculations, the degree of rotational excitation imparted to the CN fragment in the dissociation process is revealed. It seems quite possible to deposit ~0.3 eV into CN rotation (see Table 3.2). This would lead to an *upper limit* for the CN rotational levels, j_{CN}, of ~35. Further, it is expected that some of the CN–Ar collision energy imparted to the CN fragment will also end up in rotation. In addition, the CN–Ar collision is likely to occur near the potential minimum on the excited-state surface. For the [I^-–CN] complex formed, R–T transfer should be slow, which effectively sequesters the rotational energy for a period of time longer than the radiative lifetime of the excited state. Thus, there appears to be a mechanism allowing the [I^-–CN] complex to stay together for a sufficient time to radiatively decay to the ground state, as is required to stabilize the anion and yield the observed one-atom caging in the photodissociation of ICN^-(Ar). Additional dynamics studies to further elucidate the mechanism for energy transfer are anticipated.

The calculations of bare ICN^- dynamics point to a mechanism for the one-atom cage effect that we observe in ICN^-(Ar). In a small portion of the excited population, collision of the CN fragment with Ar reduces the excess energy remaining with the I^- and CN components. Additionally, the relatively slow dissociation of ICN^- allows ample time to sample the anisotropic portions of the excited-state potential energy surface, thus populating a reasonable degree of rotational excitation in the CN fragment. Taken together, these two processes tie up a considerable amount of energy, allowing the [I^-–CN] complex a substantial excited-state lifetime and, thus, a non-negligible radiative transition probability. This mechanism gains support from photodissociation studies of neutral ICN in a cryogenic matrix, detecting emission following cage-induced trapping on a weakly bound excited-state surface.[57]

3.5 Conclusions

Despite the lack of a conical intersection, the dynamics of photodissociated, linear ICN^- result in a highly rotationally excited CN fragment. The ability of the ICN^- chromophore to sequester substantial amounts of energy in CN rotation enables both the single-solvent caging and the production of highly solvated photodissociation products. In all cases, CN rotation (hindered or free) is a crucial part of the intramolecular energy flow pathways and a major sink for internal energy.

Chapter IV: Photofragmentation Dynamics of $ICN^-(CO_2)_n$

4.1 Introduction

To further understand the role solvent plays in dissociation dynamics of an anionic cluster, the photofragmentation of mass-selected $ICN^-(CO_2)_n$ was studied following 400, 500, and 600 nm excitation to the dissociative $^2\Pi_{1/2}$ excited state of the chromophore (see Fig. 4.1). Previous studies[33-35, 39, 69, 75-81] of anionic clusters report an increased probability of nonadiabatic dynamics contributing to the photofragmentation process due to changes in the electronic structure of the chromophore. As seen in Chapter III, solvation of ICN^- with one to five Ar atoms leads to the observation of one-atom caging (n = 1) and highly-solvated I^--based and ICN^--based photoproducts, but CN^--based products were absent. These observations are the result of weakly-solvating labile Ar atoms and the significant amount (~20%) of the excitation energy that is partitioned into CN rotation. Because Ar is readily polarized (α = 1.664 $Å^3$),[82] but has neither a permanent dipole nor quadrupole moment, the dominant solute-solvent electrostatic interaction is a short-range $\left(\propto\frac{1}{r^4}\right)$ ion-induced dipole interaction. The Ar solvent binding energy to the ICN^- chromophore was measured[67] to be ~50 meV, in agreement with experimental studies in which Ar is used to reduce the internal energy content of a cluster by evaporative cooling.[83-85] With such a small solvent binding energy, solvation of the ICN^- chromophore with Ar results in only minor perturbations to potential surfaces at the ground state equilibrium geometry of ICN^-.

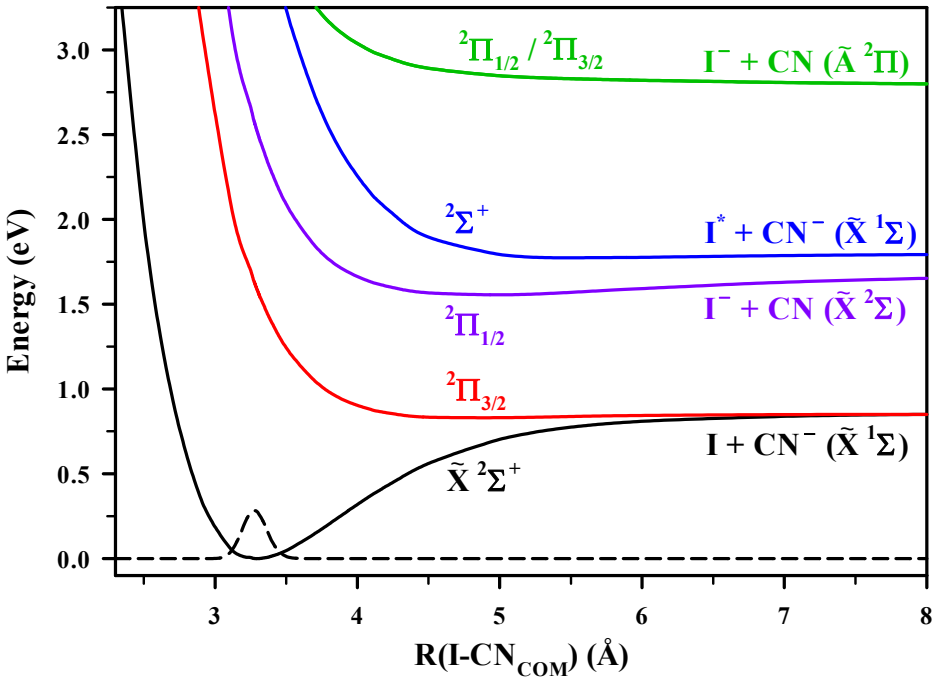

Figure 4.1 Linear ICN^- potential energy curves (based on Ref. 66) as a function of the distance from the iodine atom to the center-of-mass of the CN diatom. The ground-state wavefunction is shown as a black dashed line.

By performing similar photofragmentation experiments to those presented in Chapter III, the effect of long-range electrostatic interactions on the photodissociation of the ICN^- chromophore is examined using a CO_2 molecular solvent. The similar mass of an Ar atom (44 amu) and a CO_2 molecule (40 amu) leads to similar solute-solvent kinematics. Thus, differences in the dissociation dynamics of $ICN^-(Ar)_n$ and $ICN^-(CO_2)_n$ are attributed to the electrostatic interactions between the ICN^- chromophore and the solvent. The CO_2 molecule has a large quadrupole moment ($(-4.31\pm0.74)\times10^{-40}$ C m^2),[86] with an approximate charge distribution of +1 on the carbon atom and −½ on each oxygen. This results in not only a long-range $\left(\propto\frac{1}{r^3}\right)$ ion-quadrupole interaction between the ICN^- chromophore and the CO_2 solvent, but also a strong CO_2–CO_2 interaction that results in the formation a rigid cage around

the chromophore. Previous studies of CO_2 solvated dihalides[34, 35, 39, 87, 88] report a CO_2 solvent binding energy of ~200–300 meV, approximately a factor of 4–5 times larger than that of a solvent Ar atom. As a result, the dynamics involved in the photofragmentation of $ICN^-(CO_2)_n$ are expected to differ significantly from those observed for $ICN^-(Ar)_n$. Following photoexcitation of $ICN^-(CO_2)_n$ to the $^2\Pi_{1/2}$ excited state, CN^--based and ICN^--based photoproducts are observed as a result of increased probability of nonadiabatic transitions due to solvation, similar to $IBr^-(CO_2)_n$ and $ICl^-(CO_2)_n$.[33, 35] However, in contrast with $IBr^-(CO_2)_n$, and $ICl^-(CO_2)_n$, following photofragmentation of $ICN^-(CO_2)_n$ the yield of X^--based (X = Br, Cl, or CN) photoproducts dominates the ionic photoproduct distribution for most values of *n* studied and recombined products are a minority. Comparison of the results of photofragmentation studies on different solutes within a cluster of CO_2 molecules provides evidence for the role of internal energy of the solute in the dissociation dynamics.

4.2 Experimental

The photofragmentation studies of $ICN^-(CO_2)_n$ were performed utilizing a dual time-of-flight mass spectrometer (TOF MS) in conjunction with a nanosecond laser system. A detailed description of the TOF MS and the laser system was presented in Chapter II; only details of the experiment relevant to $ICN^-(CO_2)_n$ photofragmentation studies will be presented. A gas mixture, formed by passing CO_2 at a pressure of 1–2 atm over solid ICN (synthesized by the experimental procedure reported by Bak and Hillebert[42]) is pulsed through an 800 μm orifice of a General Valve nozzle (Series 9) operated at 50 Hz. Following electron impact from a 1 keV electron beam, anions are formed *via* slow secondary-electron attachment. Anions are formed *via* collisions with the neutral CO_2 solvent and are then extracted perpendicularly into a

Wiley-McLaren TOF MS[41] by a pulsed electric field. After entering the TOF MS, the ions are accelerated, steered, and focused before a fast potential switch[49] re-references the anions to earth ground. Directly before the Wiley-McLaren spatial focus, a pulsed mass gate deflects all ions, except the desired anionic clusters. The mass-selected anions are then photoexcited *via* a nanosecond laser pulse at the Wiley-McLaren spatial focus.

Pulsed 430 to 650 nm light is generated *via* a nanosecond laser system (Coherent Infinity XPO), with output energy of up to 5 mJ/pulse. The photoproducts that result from interaction of the parent cluster with laser radiation enter a single-stage secondary reflectron mass spectrometer and are detected by a dual microchannel plate (MCP) detector 8° off the parent ion beam axis. The electric potential applied to the reflectron is scaled in proportion to the mass ratio of the ionic photofragment and parent ion. This adjustment refocuses the trajectories of the ionic photoproducts onto the MCP detector. A mass spectrum of the ionic photofragments detected on the off-axis MCPs is amplified, digitized, and averaged after which the area under of each ionic photoproduct peak is determined. The mass spectrum is again obtained under the same conditions, but with the laser radiation blocked to provide a background trace for subtraction. The ionic photoproduct distributions and the *relative* cross section for production of ionic photoproducts reveal the effects of solvation on the photodissociation dynamics of the $ICN^-(CO_2)_n$.

4.3 Photodissociation Action Spectra

The effects of solvation with CO_2 on the electronic structure of ICN^- were investigated by measuring the photodissociation action spectra of $ICN^-(CO_2)$. Analysis of the action spectra provides the *relative* cross section for the production of each ionic photoproduct following

excitation of $ICN^-(CO_2)_n$ to the $^2\Pi_{1/2}$ excited state. As detailed in Chapter II, the cross section reported is a *relative* cross section due to unmeasured scaling factors such as detection efficiency of the photoproduct and parent ions and spatial overlap of the ion-laser interaction.

Figures 4.2 and 4.3 show the *relative* cross section, $\sigma_{rel}(\lambda)$, for the production of each ionic photoproduct following 430 to 650 nm excitation of ICN^- and $ICN^-(CO_2)$. The error limits are the average percent error for each photoproduct across the entire spectral range and the values are given in the captions for Fig. 4.2 and 4.3. Comparison of the cross sections reveals a slight shift in the location of the peak and an increased width for the I^- and CN^- products from $ICN^-(CO_2)_n$ photodissociation compared to the I^- products from ICN^- photodissociation. For example, the Gaussian-like shape of the *relative* cross section for production of I^- photoproducts from ICN^- photodissociation has a full-width-at-half-the-maximum (FWHM) of roughly 60 nm, whereas the FWHM for the *relative* cross section for I^- from $ICN^-(CO_2)$ photodissociation is roughly 80 nm.

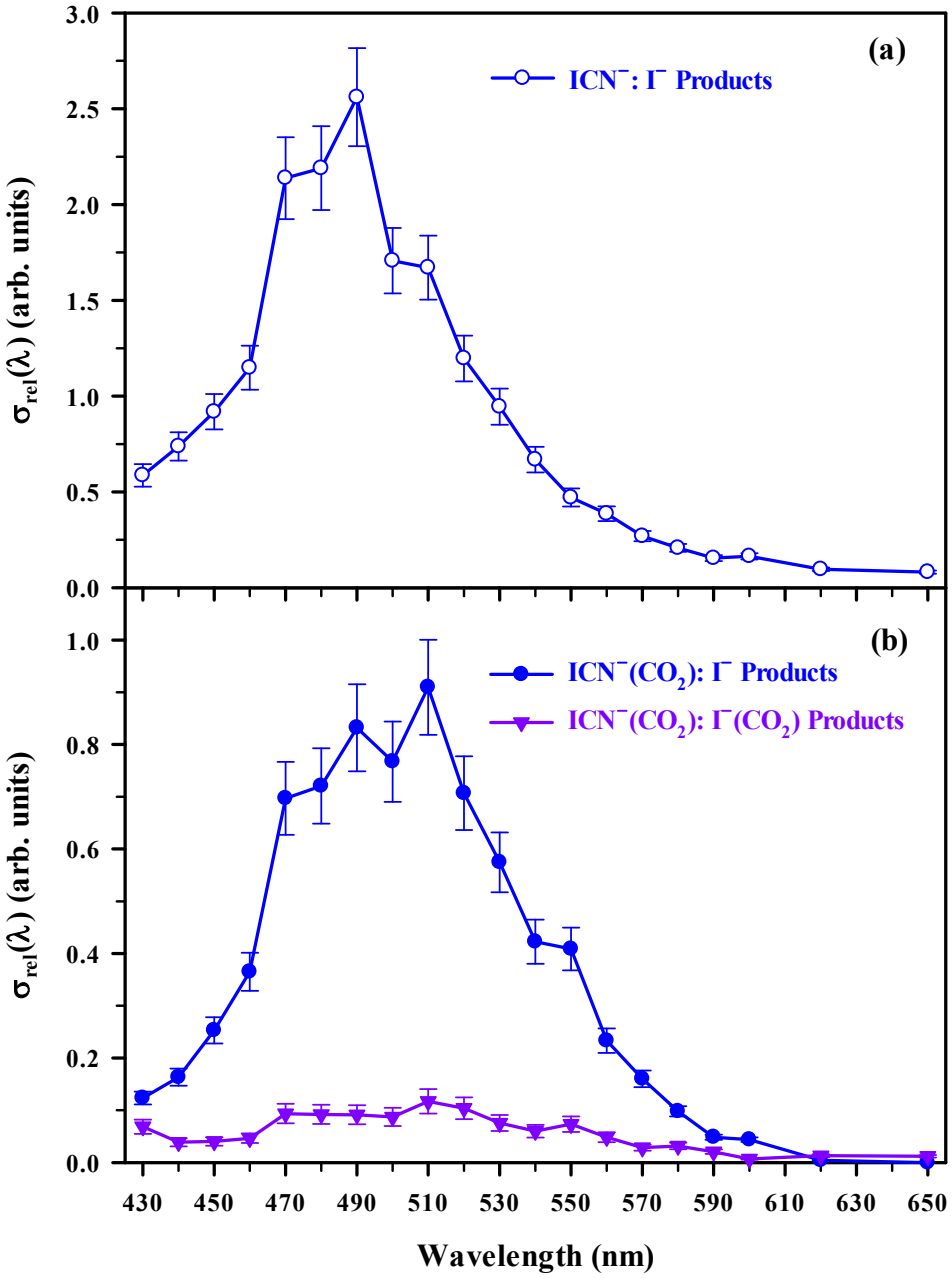

Figure 4.2 *Relative* cross sections ($\sigma_{rel}(\lambda)$) for the production of I^- and $I^-(CO_2)$ photoproducts (b) following excitation of $ICN^-(CO_2)$ to the $^2\Pi_{1/2}$ excited state. The relative cross section for the production of I^- photoproducts (a) following excitation of ICN^- to the $^2\Pi_{1/2}$ excited state is shown as a reference. The error limits are the average percent error for each photoproduct across the entire spectral range and are defined as follows: 10% for I^- from photodissociation of ICN^-, and 10% and 20% for I^- and $I^-(CO_2)$ from photodissociation of $ICN^-(CO_2)$, respectively.

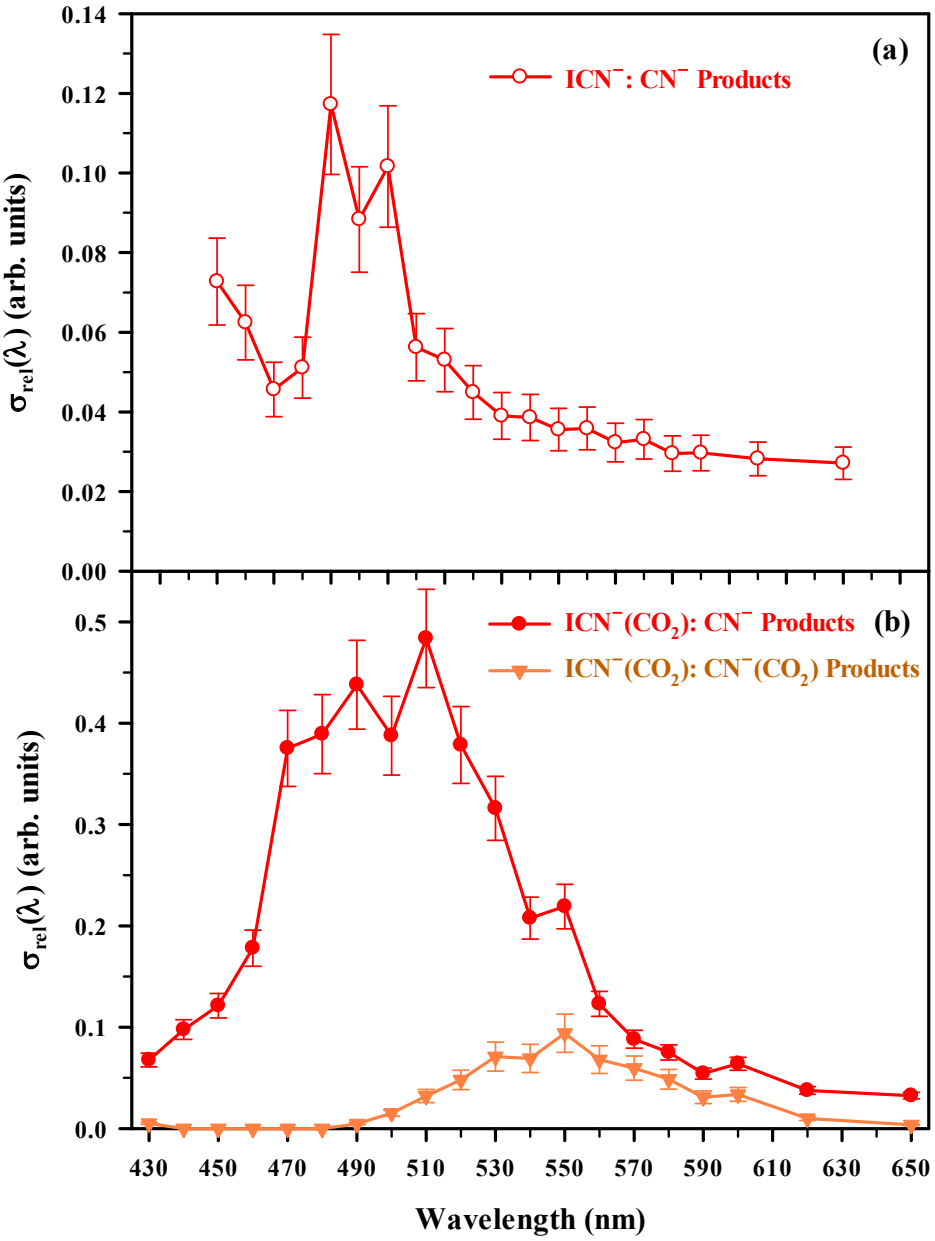

Figure 4.3 *Relative* cross sections ($\sigma_{rel}(\lambda)$) for the production of CN^- and $CN^-(CO_2)$ photoproducts (b) following excitation of $ICN^-(CO_2)$ to the $^2\Pi_{1/2}$ excited state. The relative cross section for the production of CN^- photoproducts (a) following excitation of ICN^- to the $^2\Pi_{1/2}$ excited state is shown as a reference. The error limits are the average percent error for each photoproduct across the entire spectral range and are defined as follows: 15% for CN^- from photodissociation of ICN^-, and 10% and 20% for CN^- and $CN^-(CO_2)$ from photodissociation of $ICN^-(CO_2)$, respectively.

The small red shift and increase in the width of the *relative* cross section for the production of I^- and CN^- products from photodissociation of $ICN^-(CO_2)$ are likely the result of a change in the charge distribution near the ground state equilibrium geometry of ICN^- following excitation from the ground state to the $^2\Pi_{1/2}$ excited state. Because the asymptotes of the $\tilde{X}\ ^2\Sigma^+$ and $^2\Sigma^+$ states both correspond to CN^- photoproducts and the photon energy following 430 to 650 nm excitation is insufficient to result in a $^2\Pi_{1/2}/^2\Pi_{3/2} \leftarrow \tilde{X}$ transition ($^2\Pi_{1/2}/^2\Pi_{3/2}$ mixed state designation used as defined by McCoy[66]), observation of the I^- and $I^-(CO_2)$ photoproducts must be the result of dissociation on the $^2\Pi_{1/2}$ excited state (purple in Fig. 4.1) that corresponds to I^- + CN photoproducts. Multi-reference configuration-interaction calculations performed by McCoy[66] show that, near the equilibrium geometry on the ground state of the ICN^- chromophore, roughly 44% of the excess charge is localized on CN. For this same geometry on the $^2\Pi_{1/2}$ excited state, ~80% of the excess charge is localized on the CN, even though the asymptotic photoproducts for this state are I^- + CN. (This change in charge distribution from the ground-state equilibrium geometry to the asymptote of the $^2\Pi_{1/2}$ excited state has a drastic effect on the photofragmentation dynamics, as discussed in Sec. 4.4.) Because solvation of a smaller anion is energetically favored,[33, 77, 78] solvation of CN^- (ionic radius = 1.77 Å)[89, 90] is favored over solvation of I^- (ionic radius = 2.20 Å).[91] Since the charge is more localized on the CN diatom on the $^2\Pi_{1/2}$ excited state, the $^2\Pi_{1/2}$ state should be more stabilized than the ground state, and a red shift in the cross section is expected. Alternatively, if the charge localized on the iodine, a blue-shift in the cross section would occur because of solvation of the larger iodine is energetically unfavorable. Therefore, it is proposed that solvation of the ICN^- chromophore with CO_2 results in a solvated $^2\Pi_{1/2}$ excited state that is stabilized at large internuclear distances. This

result illustrates the relative effect of the long-range electrostatic interactions between ICN^- and CO_2 on the ground state and $^2\Pi_{1/2}$ excited state of the ICN^- chromophore.

4.4 Photofragmentation of $ICN^-(CO_2)_n$

As with previously studied dihalide clusters,[33-35] it was expected that the photofragmentation of $ICN^-(CO_2)_n$ would result in three dissociation products following excitation to the $^2\Pi_{1/2}$ excited state: I^--based products from direct adiabatic dissociation, CN^--based products from nonadiabatic transitions, and recombined ICN^--based photoproducts. The distribution of these ionic photoproducts is predicted to vary with excitation energy (due to different amounts of kinetic energy release) and the size of the parent cluster anion. Similar to photofragmentation studies[36] of $I_2^-(Ar)_n$ and $I_2^-(CO_2)_n$, the caging efficiencies of the Ar and CO_2 solvents were expected to be drastically different.

4.4.1 Photofragmentation Data at 400, 500, and 600 nm

The photoproduct distributions of each ionic dissociation channel (I^--based, CN^--based, or ICN^--based) following 500 and 600 nm excitation of $ICN^-(CO_2)_n$ as a function of the parent cluster size are shown in Fig. 4.4 an 4.5, respectively. The total yield for each ionic photoproduct channel, in bold red in Tables 4.1 and 4.2, is plotted in the figures. Additionally, the yield of all photoproducts observed following excitation of $ICN^-(CO_2)_n$ at these two wavelengths is tabulated in Table 4.1 and 4.2. All excitation energies utilized are larger than the measured bond dissociation energy[67] of ground electronic-state ICN^-, $D_o(I–CN^-) = 0.84(+0.04/−0.02)$ eV, and laser power dependence studies are performed to ensure photofragmentation was the result of a

one-photon process. Additionally, typical statistical errors in the ionic photoproduct distributions are roughly 5%.

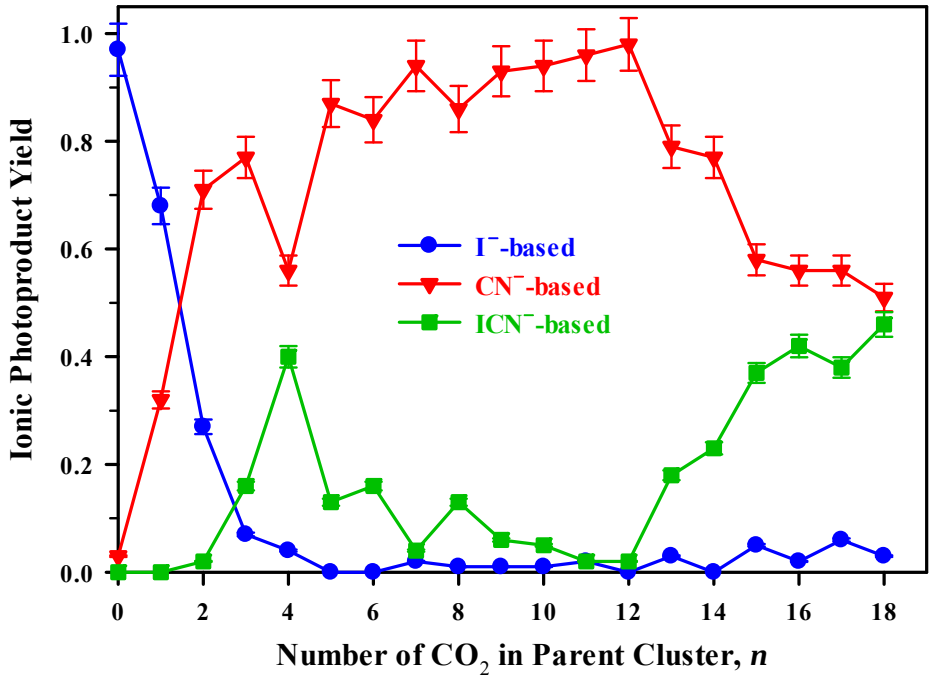

Figure 4.4 Ionic photoproduct distribution of $ICN^-(CO_2)_n$ upon one-photon 500 nm excitation to the $^2\Pi_{1/2}$ excited state. The error bars correspond to a 5% standard deviation and are plotted for each ionic product distribution.

Table 4.1 One-photon ionic photoproducts following 500 nm excitation of $ICN^-(CO_2)_n$.

Parent Cluster	CN^--Based	I^--Based	ICN^--Based
ICN^-	CN^- = 3% **3%**	I^- = 97% **97%**	**0%**
$ICN^-(CO_2)$	CN^- = 31% $CN^-(CO_2)$ = 1% **32%**	I^- = 61% $I^-(CO_2)$ = 7% **68%**	**0%**
$ICN^-(CO_2)_2$	CN^- = 29% CN^- (CO_2) = 42% **71%**	I^- = 12% $I^-(CO_2)$ = 15% **27%**	ICN^- = 2% **2%**
$ICN^-(CO_2)_3$	CN^- = 19% $CN^-(CO_2)$ = 58% **77%**	$I^-(CO_2)$ = 7% **7%**	ICN^- = 16% **16%**
$ICN^-(CO_2)_4$	CN^- = 3% $CN^-(CO_2)$ = 39% $CN^-(CO_2)_2$ = 14% **56%**	$I^-(CO_2)_2$ = 4% **4%**	ICN^- = 40%. **40%**
$ICN^-(CO_2)_5$	$CN^-(CO_2)$ = 17% $CN^-(CO_2)_2$ = 69% $CN^-(CO_2)_3$ = 1% **87%**	**0%**	ICN^- = 12% $ICN^-(CO_2)$ = 1% **13%**
$ICN^-(CO_2)_6$	$CN^-(CO_2)$ = 3% $CN^-(CO_2)_2$ = 56% $CN^-(CO_2)_3$ = 24% $CN^-(CO_2)_4$ = 1% **84%**	**0%**	ICN^- = 14% $ICN^-(CO_2)$ = 2% **16%**
$ICN^-(CO_2)_7$	$CN^-(CO_2)$ = 1% $CN^-(CO_2)_2$ = 10% $CN^-(CO_2)_3$ = 78% $CN^-(CO_2)_4$ = 4% $CN^-(CO_2)_5$ = 1% **94%**	I^- = 1% $I^-(CO_2)$ = 1% **2%**	ICN^- = 2% $ICN^-(CO_2)$ = 2% **4%**

$ICN^-(CO_2)_8$	$CN^-(CO_2)_3$ = 28% $CN^-(CO_2)_4$ = 35% $CN^-(CO_2)_5$ = 20% $CN^-(CO_2)_6$ = 3% **86%**	$I^-(CO_2)_2$ = 1% **1%**	ICN^- = 7% $ICN^-(CO_2)$ = 4% $ICN^-(CO_2)_2$ = 2% **13%**
$ICN^-(CO_2)_9$	$CN^-(CO_2)_3$ = 1% $CN^-(CO_2)_4$ = 34% $CN^-(CO_2)_5$ = 6% $CN^-(CO_2)_6$ = 50% $CN^-(CO_2)_7$ = 2% **93%**	$I^-(CO_2)_2$ = 1% **1%**	ICN^- = 2% $ICN^-(CO_2)$ = 2% $ICN^-(CO_2)_2$ = 2% **6%**
$ICN^-(CO_2)_{10}$	$CN^-(CO_2)_4$ = 1% $CN^-(CO_2)_5$ = 4% $CN^-(CO_2)_6$ = 43% $CN^-(CO_2)_7$ = 46% **94%**	$I^-(CO_2)_4$ = 1% **1%**	ICN^- = 1% $ICN^-(CO_2)$ = 1% $ICN^-(CO_2)_2$ = 2% $ICN^-(CO_2)_3$ = 1% **5%**
$ICN^-(CO_2)_{11}$	$CN^-(CO_2)_6$ = 1% $CN^-(CO_2)_7$ = 86% $CN^-(CO_2)_8$ = 9% **96%**	$I^-(CO_2)_5$ = 1% **2%**	$ICN^-(CO_2)$ = 1% $ICN^-(CO_2)_2$ = 1% **2%**
$ICN^-(CO_2)_{12}$	$CN^-(CO_2)_7$ = 11% $CN^-(CO_2)_8$ = 87% **98%**	**0%**	$ICN^-(CO_2)_2$ = 1% $ICN^-(CO_2)_3$ = 1% **2%**
$ICN^-(CO_2)_{13}$	$CN^-(CO_2)_6$ = 1% $CN^-(CO_2)_7$ = 1% $CN^-(CO_2)_8$ = 64% $CN^-(CO_2)_9$ = 13% **79%**	$I^-(CO_2)_6$ = 3% **3%**	$ICN^-(CO_2)_2$ = 1% $ICN^-(CO_2)_3$ = 5% $ICN^-(CO_2)_4$ = 10% $ICN^-(CO_2)_5$ = 3% **18%**
$ICN^-(CO_2)_{14}$	$CN^-(CO_2)_8$ = 3% $CN^-(CO_2)_9$ = 71% $CN^-(CO_2)_{10}$ = 3% **77%**	**0%**	$ICN^-(CO_2)_3$ = 2% $ICN^-(CO_2)_4$ = 11% $ICN^-(CO_2)_5$ = 7% $ICN^-(CO_2)_6$ = 3% **23%**

$ICN^-(CO_2)_{15}$	$CN^-(CO_2)_9$ = 17% $CN^-(CO_2)_{10}$ = 33% $CN^-(CO_2)_{11}$ = 8% **58%**	$I^-(CO_2)_5$ = 1% $I^-(CO_2)_6$ = 2% $I^-(CO_2)_7$ = 2% **5%**	$ICN^-(CO_2)_4$ = 8% ICN $(CO_2)_5$ = 17% $ICN^-(CO_2)_6$ = 11% $ICN^-(CO_2)_7$ = 1% **37%**
$ICN^-(CO_2)_{16}$	$CN^-(CO_2)_{10}$ = 6% $CN^-(CO_2)_{11}$ = 35% $CN^-(CO_2)_{12}$ = 15% **56%**	$I^-(CO_2)_8$ = 2% **2%**	$ICN^-(CO_2)_4$ = 1% $ICN^-(CO_2)_5$ = 10% $ICN^-(CO_2)_6$ = 16% $ICN^-(CO_2)_7$ = 13% $ICN^-(CO_2)_8$ = 2% **42%**
$ICN^-(CO_2)_{17}$	$CN^-(CO_2)_{12}$ = 42% $CN^-(CO_2)_{13}$ = 14% **56%**	$I^-(CO_2)_7$ = 2% $I^-(CO_2)_8$ = 2% $I^-(CO_2)_9$ = 2% **6%**	$ICN^-(CO_2)_5$ = 2% $ICN^-(CO_2)_6$ = 14% $ICN^-(CO_2)_7$ = 17% $ICN^-(CO_2)_8$ = 5% **38%**
$ICN^-(CO_2)_{18}$	$CN^-(CO_2)_{12}$ = 2% $CN^-(CO_2)_{13}$ = 37% $CN^-(CO_2)_{14}$ = 12% **51%**	$I^-(CO_2)_7$ = 1% $I^-(CO_2)_8$ = 1% $I^-(CO_2)_9$ = 1% **3%**	$ICN^-(CO_2)_6$ = 5% $ICN^-(CO_2)_7$ = 19% $ICN^-(CO_2)_8$ = 15% $ICN^-(CO_2)_9$ = 5% $ICN^-(CO_2)_{10}$ = 2% **46%**

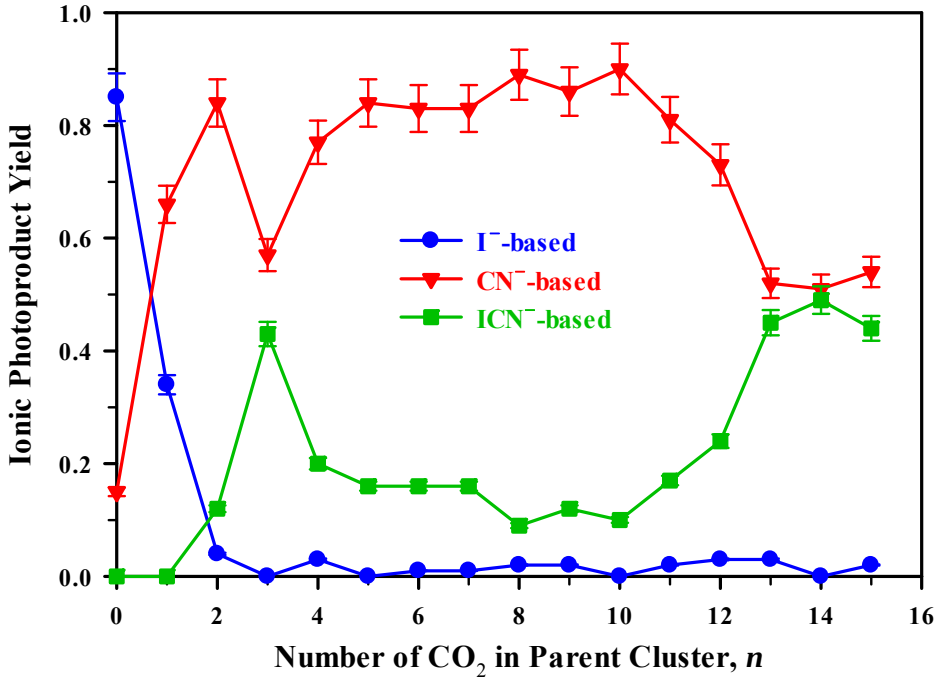

Figure 4.5 Ionic photoproduct distribution of $ICN^-(CO_2)_n$ upon one-photon 600 nm excitation to the $^2\Pi_{1/2}$ excited state. The error bars correspond to a 5% standard deviation and are plotted for each ionic product distribution.

Table 4.2 One-photon ionic photoproducts following 600 nm excitation of $ICN^-(CO_2)_n$.

Parent Cluster	CN^--Based	I^--Based	ICN^--Based
ICN^-	CN^- = 15% **15%**	I^- = 85% **85%**	**0%**
$ICN^-(CO_2)$	CN^- = 43% $CN^-(CO_2)$ = 23% **66%**	I^- = 34% **34%**	**0%**
$ICN^-(CO_2)_2$	CN^- = 35% $CN^-(CO_2)$ = 49% **84%**	$I^-(CO_2)$ = 4% **4%**	ICN^- = 12% **12%**
$ICN^-(CO_2)_3$	CN^- = 10% $CN^-(CO_2)$ = 45% $CN^-(CO_2)_2$ = 2% **57%**	**0%**	ICN^- = 43% **43%**
$ICN^-(CO_2)_4$	CN^- = 1% $CN^-(CO_2)$ = 12% $CN^-(CO_2)_2$ = 64% **77%**	I^- = 3% **3%**	ICN^- = 19% $ICN^-(CO_2)$ = 1% **20%**
$ICN^-(CO_2)_5$	$CN^-(CO_2)$ = 5% $CN^-(CO_2)_2$ = 42% $CN^-(CO_2)_3$ = 33% $CN^-(CO_2)_4$ = 4% **84%**	**0%**	ICN^- = 13% $ICN^-(CO_2)$ = 3% **16%**
$ICN^-(CO_2)_6$	$CN^-(CO_2)$ = 2% $CN^-(CO_2)_2$ = 3% $CN^-(CO_2)_3$ = 59% $CN^-(CO_2)_4$ = 10% $CN^-(CO_2)_5$ = 9% **83%**	$I^-(CO_2)_2$ = 1% **1%**	ICN^- = 10% $ICN^-(CO_2)$ = 4% $ICN^-(CO_2)_2$ = 2% **16%**

$ICN^-(CO_2)_7$	$CN^-(CO_2) = 1\%$ $CN^-(CO_2)_2 = 2\%$ $CN^-(CO_2)_3 = 1\%$ $CN^-(CO_2)_4 = 49\%$ $CN^-(CO_2)_5 = 11\%$ $CN^-(CO_2)_6 = 19\%$ **83%**	$I^-(CO_2)_3 = 1\%$ **1%**	$ICN^- = 6\%$ $ICN^-(CO_2) = 6\%$ $ICN^-(CO_2)_2 = 3\%$ $ICN^-(CO_2)_3 = 1\%$ **16%**
$ICN^-(CO_2)_8$	$CN^-(CO_2)_3 = 1\%$ $CN^-(CO_2)_4 = 1\%$ $CN^-(CO_2)_5 = 5\%$ $CN^-(CO_2)_6 = 55\%$ $CN^-(CO_2)_7 = 27\%$ **89%**	$I^-(CO_2)_4 = 1\%$ $I^-(CO_2)_5 = 1\%$ **2%**	$ICN^- = 1\%$ $ICN^-(CO_2) = 4\%$ $ICN^-(CO_2)_2 = 2\%$ $ICN^-(CO_2)_3 = 2\%$ **9%**
$ICN^-(CO_2)_9$	$CN^-(CO_2)_3 = 2\%$ $CN^-(CO_2)_4 = 1\%$ $CN^-(CO_2)_5 = 1\%$ $CN^-(CO_2)_6 = 2\%$ $CN^-(CO_2)_7 = 80\%$ **86%**	$I^-(CO_2)_5 = 2\%$ **2%**	$ICN^-(CO_2) = 3\%$ $ICN^-(CO_2)_2 = 4\%$ $ICN^-(CO_2)_3 = 3\%$ $ICN^-(CO_2)_4 = 2\%$ **12%**
$ICN^-(CO_2)_{10}$	$CN^-(CO_2)_3 = 2\%$ $CN^-(CO_2)_4 = 2\%$ $CN^-(CO_2)_5 = 2\%$ $CN^-(CO_2)_6 = 2\%$ $CN^-(CO_2)_7 = 12\%$ $CN^-(CO_2)_8 = 68\%$ $CN^-(CO_2)_9 = 2\%$ **90%**	**0%**	$ICN^-(CO_2) = 1\%$ $ICN^-(CO_2)_2 = 3\%$ $ICN^-(CO_2)_3 = 4\%$ $ICN^-(CO_2)_4 = 2\%$ **10%**
$ICN^-(CO_2)_{11}$	$CN^-(CO_2)_5 = 2\%$ $CN^-(CO_2)_6 = 3\%$ $CN^-(CO_2)_7 = 3\%$ $CN^-(CO_2)_8 = 66\%$ $CN^-(CO_2)_9 = 7\%$ **81%**	$I^-(CO_2)_6 = 1\%$ **2%**	$ICN^-(CO_2) = 1\%$ $ICN^-(CO_2)_2 = 2\%$ $ICN^-(CO_2)_3 = 6\%$ $ICN^-(CO_2)_4 = 4\%$ $ICN^-(CO_2)_5 = 1\%$ $ICN^-(CO_2)_6 = 3\%$ **17%**

$ICN^-(CO_2)_{12}$	$CN^-(CO_2)_6$ = 4% $CN^-(CO_2)_7$ = 6% $CN^-(CO_2)_8$ = 5% $CN^-(CO_2)_9$ = 58% **73%**	$I^-(CO_2)_7$ = 3% **3%**	$ICN^-(CO_2)_3$ = 5% $ICN^-(CO_2)_4$ = 10% $ICN^-(CO_2)_5$ = 5% $ICN^-(CO_2)_6$ = 2% $ICN^-(CO_2)_7$ = 2% **24%**
$ICN^-(CO_2)_{13}$	$CN^-(CO_2)_8$ = 2% $CN^-(CO_2)_9$ = 27% $CN^-(CO_2)_{10}$ = 23% **52%**	$I^-(CO_2)_7$ = 2% $I^-(CO_2)_8$ = 1% **3%**	$ICN^-(CO_2)_3$ = 2% $ICN^-(CO_2)_4$ = 15% $ICN^-(CO_2)_5$ = 19% $ICN^-(CO_2)_6$ = 9% **45%**
$ICN^-(CO_2)_{14}$	$CN^-(CO_2)_8$ = 5% $CN^-(CO_2)_9$ = 7% $CN^-(CO_2)_{10}$ = 11% $CN^-(CO_2)_{11}$ = 28% **51%**	**0%**	$ICN^-(CO_2)_3$ = 1% $ICN^-(CO_2)_4$ = 2% $ICN^-(CO_2)_5$ = 19% $ICN^-(CO_2)_6$ = 16% $ICN^-(CO_2)_7$ = 8% $ICN^-(CO_2)_8$ = 3% **49%**
$ICN^-(CO_2)_{15}$	$CN^-(CO_2)_9$ = 7% $CN^-(CO_2)_{10}$ = 6% $CN^-(CO_2)_{11}$ = 6% $CN^-(CO_2)_{12}$ = 31% **54%**	$I^-(CO_2)_7$ = 1% $I^-(CO_2)_8$ = 1% **2%**	$ICN^-(CO_2)_5$ = 1% $ICN^-(CO_2)_6$ = 20% $ICN^-(CO_2)_7$ = 18% $ICN^-(CO_2)_8$ = 5% **44%**

Upon absorption of a 500 or 600 nm photon, the ICN^- chromophore is excited to the $^2\Pi_{1/2}$ state, for which the adiabatic asymptote corresponds to the formation of I^- and CN ($\tilde{X}\ ^2\Sigma$) photoproducts. Thus, direct dissociation following 500 or 600 nm excitation of ICN^- results in a dominant I^- photoproduct; 97% of the observed ionic photoproducts following 500 nm excitation of ICN^- are I^-. Following the addition of one solvent CO_2 molecule, excitation to the $^2\Pi_{1/2}$ excited state *via* 500 or 600 nm light results in the observation of an increased yield of CN^--based products, with a corresponding decrease in the yield of I^--based products. Addition of the second CO_2 solvent leads to the dominance of CN^-- based products and the observation of

recombined ICN^- for both excitation wavelengths. As the number of CO_2 solvents is increased, the CN^--based products continue to dominate the ionic photoproduct distribution, and the yield of I^--based photoproducts decreases rapidly, reaching zero by $n = 5$ for both wavelengths. Remarkably, the yield of recombined products reaches a local maximum of roughly 40% at $n = 4$ and $n = 3$ for 500 and 600 nm excitation, respectively. Following the maximum yield in the recombined products, the yield begins to decrease to roughly 10–20% for $5 \leq n \leq 11$. This trend in the yield of recombined products is similar to results observed following photofragmentation of $ICl^-(CO_2)_n$, $n = 1–10$.[33, 77] For $ICN^-(CO_2)_{12–15}$, the yield of recombined photoproducts begins to increase again, but never dominates the observed ionic photoproducts for either wavelength. This is in stark contrast to the results of photofragmentation of $IBr^-(CO_2)_{n \geq 8}$,[35] for which only recombined products were observed following photoexcitation to the $\tilde{A}'\,^2\Pi_{1/2}$ excited state of IBr^-.

Additionally, photofragmentation studies were also performed following 400 nm excitation of $ICN^-(CO_2)_n$ ($n = 0–8$) to the determine the effect of an increased kinetic energy release on the yield of recombined photoproducts. Figure 4.6 and Table 4.3 report the ionic photoproduct distributions following 400 nm excitation of $ICN^-(CO_2)_n$; the values in bold red in Table 4.3 are plotted in Figure 4.6 as a function of parent cluster size. Excitation with 400 nm provides roughly 0.6 eV more asymptotic kinetic energy release on the $^2\Pi_{1/2}$ excited state than 500 nm, for a total of roughly 1.45 eV. Interestingly, excitation of ICN^- using 400 nm light results in roughly 65% I^- and roughly 35% CN^- photoproducts. The decrease in the yield of I^- photoproducts from photodissociation of the ICN^- chromophore compared to 500 nm excitation suggests that more than one excited state is taking part in the dissociation dynamics following 400 nm excitation. In marked contrast to the results for 500 and 600 nm, the addition of one CO_2

solvent molecule results in an increase in the yield of I^--based photoproducts. Furthermore, recombined ICN^- photoproducts are not observed until $n = 3$. Following the addition of the fifth CO_2 solvent, the trends observed following 400 nm excitation are qualitatively similar to those observed following 500 and 600 nm excitation, i.e. CN^--based products dominate the ionic photoproduct distribution. Explanation and comparison of the photofragmentation results for each excitation wavelength are presented in Sections 4.42, 4.4.3, and 4.4.4.

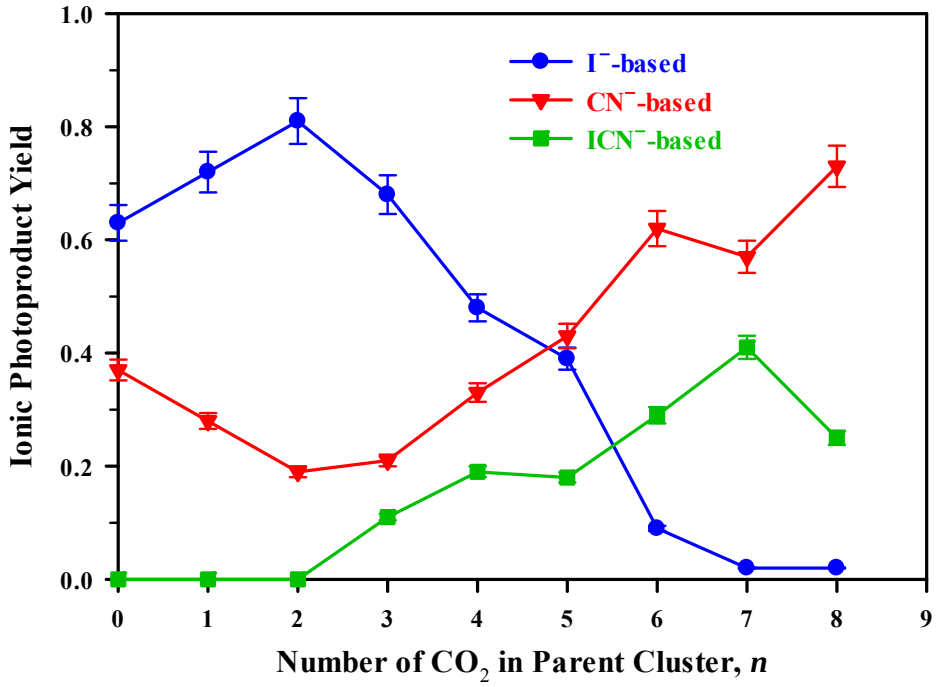

Figure 4.6 Ionic photoproduct distribution of $ICN^-(CO_2)_n$ upon one-photon 400 nm excitation to the $^2\Pi_{1/2}$ excited state. The error bars correspond to a 5% standard deviation and are plotted for each ionic product distribution.

Table 4.3 One-photon ionic photoproducts following 400 nm excitation of $ICN^-(CO_2)_n$.

Parent Cluster	CN^--Based	I^--Based	ICN^--Based
ICN^-	CN^- = 37% **37%**	I^- = 63% **63%**	**0%**
$ICN^-(CO_2)$	CN^- = 28% **28%**	I^- = 72% **72%**	**0%**
$ICN^-(CO_2)_2$	CN^- = 16% $CN^-(CO_2)$ = 3% **19%**	I^- = 28% $I^-(CO_2)$ = 53% **81%**	**0%**
$ICN^-(CO_2)_3$	CN^- = 7% $CN^-(CO_2)$ = 14% **21%**	I^- = 10% $I^-(CO_2)$ = 58% **68%**	ICN^- = 11% **11%**
$ICN^-(CO_2)_4$	CN^- = 4% $CN^-(CO_2)$ = 29% **33%**	I^- = 3% $I^-(CO_2)$ = 26% $I^-(CO_2)_2$ = 19% **48%**	ICN^- = 10% $ICN^-(CO_2)$ = 9% **19%**
$ICN^-(CO_2)_5$	$CN^-(CO_2)$ = 39% $CN^-(CO_2)_2$ = 4% **43%**	$I^-(CO_2)$ = 13% $I^-(CO_2)_2$ = 23% $I^-(CO_2)_3$ = 3% **39%**	ICN^- = 11% $ICN^-(CO_2)$ = 7% **18%**
$ICN^-(CO_2)_6$	$CN^-(CO_2)$ = 46% $CN^-(CO_2)_2$ = 13% $CN^-(CO_2)_3$ = 3% **62%**	$I^-(CO_2)$ = 2% $I^-(CO_2)_2$ = 7% **9%**	ICN^- = 17% $ICN^-(CO_2)$ = 6% $ICN^-(CO_2)_2$ = 6% **16%**
$ICN^-(CO_2)_7$	$CN^-(CO_2)$ = 21% $CN^-(CO_2)_2$ = 34% $CN^-(CO_2)_3$ = 2% **57%**	$I^-(CO_2)_2$ = 1% $I^-(CO_2)_3$ = 1% **2%**	ICN^- = 19% $ICN^-(CO_2)$ = 7% $ICN^-(CO_2)_2$ = 7% $ICN^-(CO_2)_3$ = 8% **41%**

$ICN^-(CO_2)_8$	$CN^-(CO_2) = 6\%$ $CN^-(CO_2)_2 = 48\%$ $CN^-(CO_2)_3 = 18\%$ $CN^-(CO_2)_4 = 1\%$ **73%**	$I^-(CO_2)_2 = 1\%$ $I^-(CO_2)_3 = 1\%$ **2%**	$ICN^- = 11\%$ $ICN^-(CO_2) = 4\%$ $ICN^-(CO_2)_2 = 4\%$ $ICN^-(CO_2)_3 = 6\%$ **25%**

4.4.2 Efficiency of Production of CN^--based Photofragments

Photofragmentation experiments reveal that the dissociation dynamics of solvated ICN^- are significantly affected by excitation wavelength and the solvent species utilized. Contrary to the results of the photofragmentation of $ICN^-(Ar)_n$ (Chapter III), the CN^--based photoproducts dominate the ionic photoproduct distribution following 400, 500, and 600 nm excitation of $ICN^-(CO_2)_n$. In previous photofragmentation studies[33, 35] of $IBr^-(CO_2)_n$ and $ICl^-(CO_2)_n$, excitation to the $\tilde{A}'\ ^2\Pi_{1/2}$ excited state, which correlates to dissociation into I^- photoproducts, resulted in a significant fraction of Br^--based and Cl^--based photoproducts observed for n = 1–6. Observation of the charge-transfer Br^--based photoproducts following excitation of $IBr^-(CO_2)_{1\text{-}6}$ suggested that the energy gap between the $^2\Pi_{1/2}$ excited state and the ground state was sufficiently reduced as solvation increased to lead to nonadiabatic transitions and dissociation on the ground state. Conversely, molecular dynamics simulations by Faeder and Parson[77] showed that following excitation of $ICl^-(CO_2)_n$ to the $^2\Pi_{1/2}$ excited state the observed Cl^--based products are accompanied by $I^*(^2P_{1/2})$ products as a result of dissociation on the $^2\Sigma^+$ excited state. The differing dynamics for IBr^- and ICl^- are a result of the contrasting differential solvation of the ionic fragments of the chromophore. Similar processes are proposed following photodissociation of $ICN^-(CO_2)_n$ which contribute to the dissociation dynamics as a function of parent cluster size.

To provide a rationale for the observation of an increased yield of CN^--based products, it is informative to examine the ICN^- potential energy curves. Calculations of the ICN^- potential energy curves performed by McCoy[66] show that roughly 80% of the excess charge is localized on the CN diatom on the $^2\Pi_{1/2}$ excited state near the ground state equilibrium geometry. For the same geometry, roughly 80% of the excess charge in ICN^- is localized on the iodine when on the $^2\Sigma^+$ excited state. However, as the calculations also show, the asymptotic dissociation products of these excited states correspond to I^- and CN on the $^2\Pi_{1/2}$ state and $I^*(^2P_{1/2})$ and CN^- on the $^2\Sigma^+$ excited state. Therefore, as shown in Fig. 4.7, it is proposed that a nonadiabatic crossing exists between the $^2\Pi_{1/2}$ and $^2\Sigma^+$ states at roughly 5 Å.

Photoexcitation of ICN^- to the $^2\Pi_{1/2}$ excited state leads to the observation of a minor contribution from CN^- products. For example, following 500 nm excitation, roughly 3% of the ionic photoproducts observed are CN^- and excitation of ICN^- with 400 nm light results in roughly 35% CN^- products. Because the energy gap between the $^2\Pi_{1/2}$ excited state and the ground state is too large (0.8 eV) for nonadiabatic transitions to be favorable, the observation of CN^- products suggests that following excitation of ICN^- the dissociating chromophore transitions to the $^2\Sigma^+$ excited state from the $^2\Pi_{1/2}$ state and dissociates into $I^*(^2P_{1/2})$ and CN^- photoproducts. Following excitation of either IBr^- or ICl^-, 100% of the ionic photoproducts observed were I^- as a result of direct dissociation on the $^2\Pi_{1/2}$ excited state.[33, 35, 39] However, because of the nonadiabatic crossing between the $^2\Pi_{1/2}$ and $^2\Sigma^+$ excited state of ICN^-, a minor contribution of charge-transfer CN^- photoproducts are observed, even without solvation of the ICN^- chromophore.

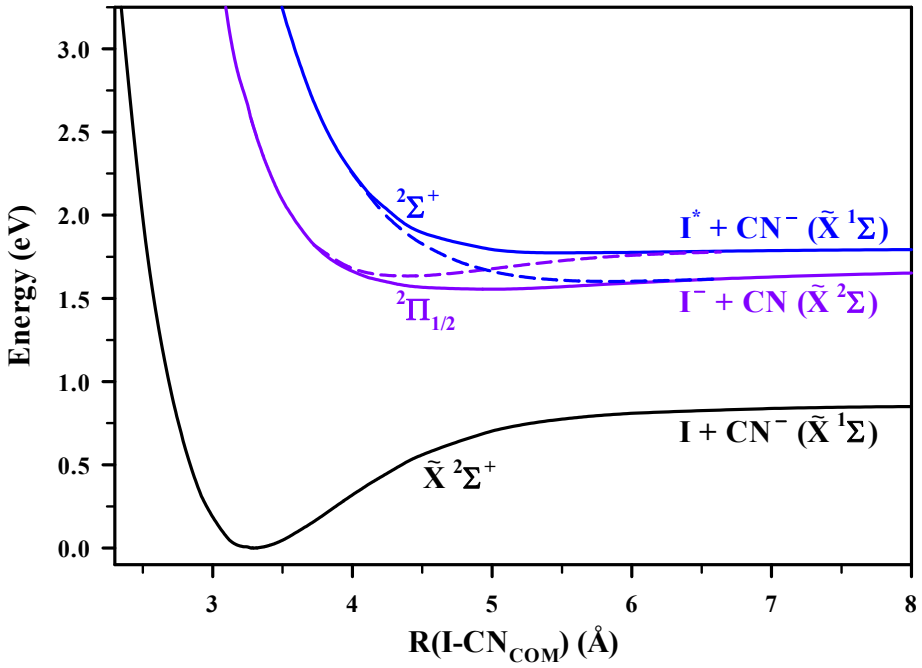

Figure 4.7 Linear ICN^- potential energy curves (based on Ref. 66) for the $\tilde{X}\ ^2\Sigma^+$, $^2\Pi_{1/2}$, and $^2\Sigma^+$ states as a function of the distance from the iodine atom to the center-of-mass of the CN diatom. The proposed *nonadiabatic* crossing is represented by two selected diabatic curves shown as dashed lines. The color of the text for the ground and excited state photoproducts correlates to *adiabatic* dissociation of the chromophore.

Following solvation of the ICN^- chromophore with CO_2, the yield of CN^--based photoproducts increases to ~30% for 500 nm. The increased yield of CN^--based products for $n \sim 1$–3 is likely the result of stabilization of the charge-transfer asymptotes with respect to the I^- asymptotes *via* the differential solvation of I^- and CN^-, similar to $ICl^-(CO_2)_n$.[33, 77] Simulations by Faeder and Parson[77] showed that adiabatic dissociation occurred on the $^2\Sigma^+$ excited state following excitation of $ICl^-(CO_2)_n$ to the $^2\Pi_{1/2}$ state. They concluded that the energy difference in the solvation of I^- versus Cl^- (~0.14 eV per CO_2) lead to the stabilization of the $^2\Sigma^+$ asymptote at large internuclear distances with respect to the $^2\Pi_{1/2}$ asymptote resulting in $I^*(^2P_{1/2})$ and Cl^- products. Because the size difference between I^- and CN^- (discussed in Sec. 4.3) is similar to the

size difference between I^- and Cl^-, solvation of ICN^- with CO_2 will likely result in similar differential solvation. Thus, the $I^*(^2P_{1/2})$ and solvated CN^- asymptote of the $^2\Sigma^+$ excited state is expected to be stabilized, which likely leads to the increased CN^- yield observed. In addition, the presence of the nonadiabatic crossing between the $^2\Pi_{1/2}$ and $^2\Sigma^+$ excited states may further increase the yield of CN^--based products. Both of these processes can occur at values of n ($n \sim 1$–3) for which nonadiabatic transitions to the ground state are still energetically unfavorable due to the large energy gap (0.8 eV) between the $^2\Pi_{1/2}$ excited state and the ground state asymptotes. Therefore, the observation of the significant yield of CN^--based photoproducts following excitation of $ICN^-(CO_2)_n$ ($n \sim 1$–3) is likely a result of excited-state transitions induced by differential solvation that lead to $I^*(^2P_{1/2})$ and CN^- products following dissociation on the $^2\Sigma^+$ excited state, similar to $ICl^-(CO_2)_n$.[77]

For all n studied ($n = 1$–12), Faeder and Parson showed[77] all Cl^--based products are the result of adiabatic dissociation on the $^2\Sigma^+$ excited state for $ICl^-(CO_2)_n$. Evidence for this adiabatic process is revealed by analysis of the average number of solvent CO_2 lost for the Cl^--based products as a function of the parent cluster size, as seen in Fig. 4.8. Because only one or two solvent CO_2 are lost on average for $n = 1$–10, dissociation must occur on the $^2\Sigma^+$ excited state and not on the ground state because a nonadiabatic transition would require dissipation of roughly 0.7 eV of additional energy. However, as seen in Fig. 4.8, the CN^--based products lose roughly 2–4 solvent CO_2 molecules following 500 nm excitation of $ICN^-(CO_2)_{3\text{-}10}$. This suggests a different dissociation mechanism is utilized and that the CN^--based products are observed for $n \geq 3$ as a result of nonadiabatic transitions from the $^2\Pi_{1/2}$ excited state to the ground state and the coincident solvent evaporation for $ICN^-(CO_2)_{n \geq 3}$. Thompson *et al.*[39] showed that nonadiabatic transitions from the $^2\Pi_{1/2}$ excited state the $\tilde{X}\ ^2\Sigma^+$ state was the sole dynamical

process that contributed to the observation of Br^--based products following excitation of $IBr^-(CO_2)_n$. With only one solvent CO_2 molecule, Br^--based products are observed and the yield increases with increased solvation. Similar dynamics are likely to occur following photofragmentation of $ICN^-(CO_2)_n$; however, because of the large energy gap between the $^2\Pi_{1/2}$ and $\tilde{X}\ ^2\Sigma^+$ asymptotes (~0.8 eV for ICN^- compared to ~0.3 eV for IBr^-),[39] nonadiabatic transitions to the ground state are not likely to occur until $n \sim 3$–4. Thus, evidence for two dynamical processes, dissociation on the $^2\Sigma^+$ excited state and nonadiabatic transitions to the ground state, resulting in the observation of CN^--based products is observed following excitation of $ICN^-(CO_2)_n$ to the $^2\Pi_{1/2}$ excited state, with contribution of each dissociation mechanism varying as a function of parent cluster size.

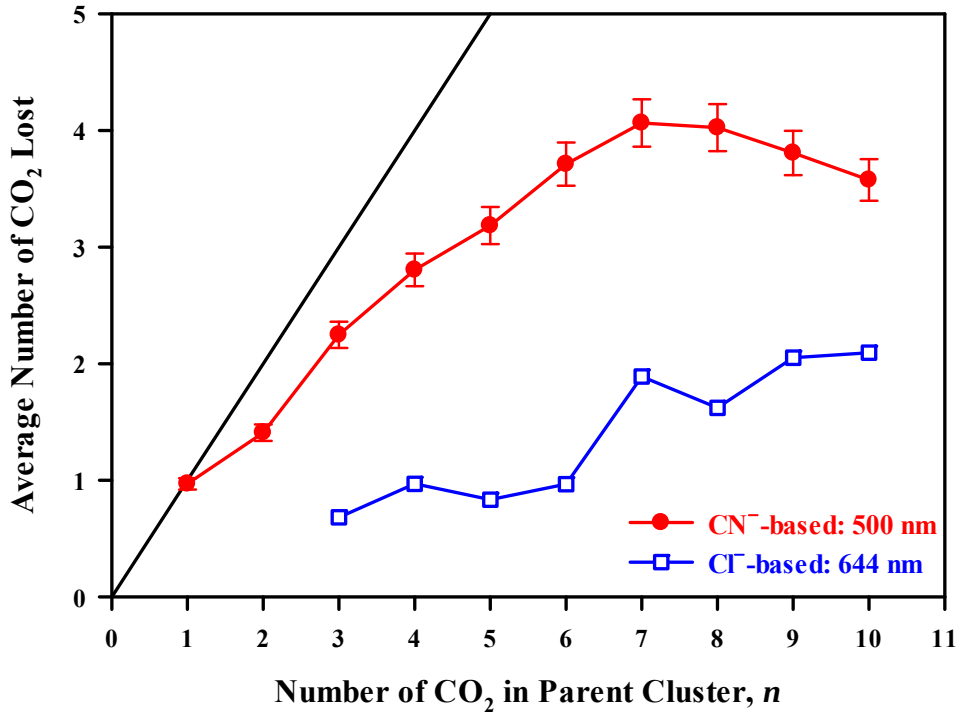

Figure 4.8 The average number of CO_2 lost from CN^--based photoproducts as a function of parent cluster size following 500 nm excitation of $ICN^-(CO_2)_n$ (n = 0–10). The number of CO_2 lost from Cl^--based products following 644 nm excitation of $ICl^-(CO_2)_n$ are also shown for comparison (Ref. 33). The solid-black diagonal line corresponds to the evaporation of all solvent CO_2 molecules from the parent cluster and is shown as a guide. The error bars on the CN^--based photoproduct distribution correspond to a 5% standard deviation.

4.4.3 Recombination as a Function of Excitation Energy

Photofragmentation of $ICN^-(CO_2)_n$ following 400, 500, and 600 nm excitation results in a rapid increase in the yield of recombined products to a peak, followed by a subsequent decrease as n increases. (For brevity, n_{max} is defined as the value of n at which the maximum in the yield of recombined products occurs). Additionally, the maximum in the yield shifts to larger values of n_{max} as excitation energy is increased. This result is contrary to what might be expected as solvation of the chromophore increases, leading to an increasingly caged chromophore.

Figure 4.9 shows the yield of recombined photoproducts following 400, 500, and 600 nm excitation of $ICN^-(CO_2)_n$.

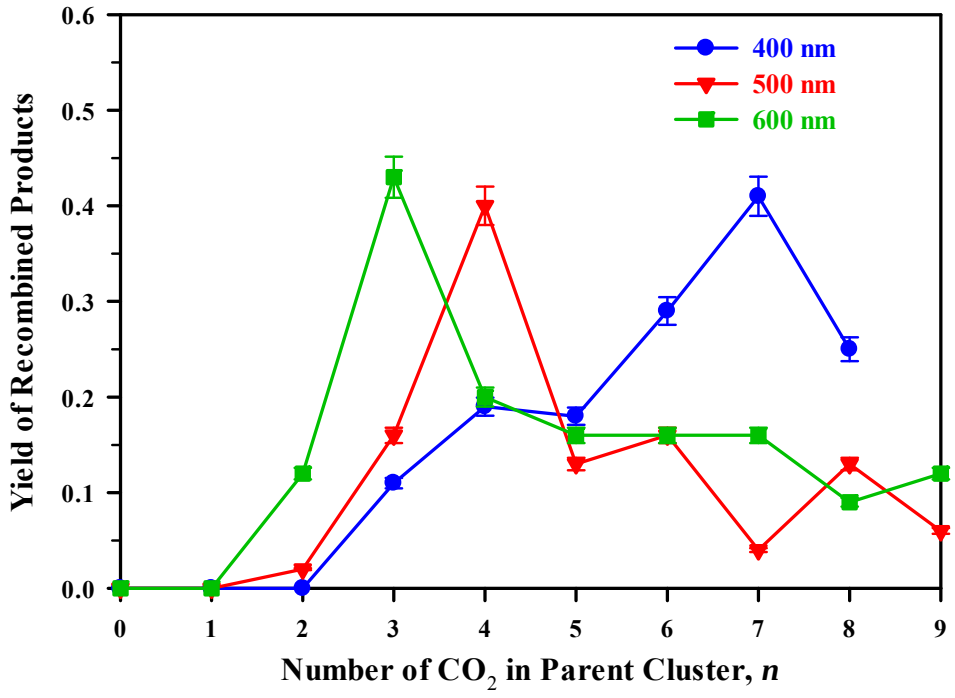

Figure 4.9 Yield of recombined ICN^--based photoproducts as a function of parent cluster size following 400, 500, and 600 nm excitation. The error bars correspond to a 5% standard deviation.

For recombination of the dissociating chromophore to occur following excitation to the $^2\Pi_{1/2}$ excited state, the chromophore must undergo a transition from the excited state to the ground state and recombine in the ground state well. Therefore, a maximum in the yield of recombined photoproducts is not expected until solvation of the ICN^- chromophore with CO_2 sufficiently reduces the 0.8 eV energy gap between the $^2\Pi_{1/2}$ and $\tilde{X}\ ^2\Sigma^+$ states to enable a transition. As proposed in Sec. 4.4.2, nonadiabatic dissociation on the $^2\Sigma^+$ excited state asymptote is the dominant source of CN^--based products until $n \approx 4$ when nonadiabatic transitions to the

ground state are proposed to be probable. This expectation is in good agreement with the peak of the yield of recombined products occurring at n_{max} = 7, 4, and 3, Fig. 4.9, following 400, 500, and 600 nm excitation, but does not explain the source of the shifting peak.

Examination of the proposed energetics of solvation provides a qualitative explanation of the shifting maximum in the yield of recombined photoproducts as a function of excitation energy. Since solvation of the smaller CN^- is energetically favored over solvation of I^-, it is proposed that a well is formed on the ground state, at large internuclear distances, corresponding to solvated CN^-, see Fig. 4.10. As the number of CO_2 solvents around the CN^- increases, the depth of the well will correspondingly increase, trapping the dissociating chromophore following a nonadiabatic transition. As the excitation energy increases, the photofragment gains sufficient kinetic energy to overcome the barrier to recombination; escaping the solvated CN^- well. However, the solvated CN^- well increasingly traps the dissociating chromophore as the number of CO_2 solvents increases, resulting in the eventual decrease in the yield of recombined photoproducts. A similar process was proposed by Nadal *et al*.[33] in the photofragmentation study of $ICl^-(CO_2)_n$. They proposed that a significant amount of the dissociating chromophores following excitation of ICl^- to the $^2\Pi_{1/2}$ excited state access the well on the ground state introduced by solvation of Cl^-. Additionally, their qualitative simulations[33] showed that the concerted motion of all solvent molecules that is required to reach the ground state global minimum, corresponding to recombined products, from the solvated Cl^- well, is unlikely to occur on the time scale of the experiment (~10 μs). Although the dynamics are similar, the additional internal degrees of freedom in the ICN^- chromophore may act as an energy sink, impacting the probability of escape of dissociating clusters from the solvated CN^- well. Furthermore, an

additional process may contribute to the development and depth of a well on the ground state from solvation of CN^-; namely, the photo-initiated intracluster reaction of CN^- and CO_2.

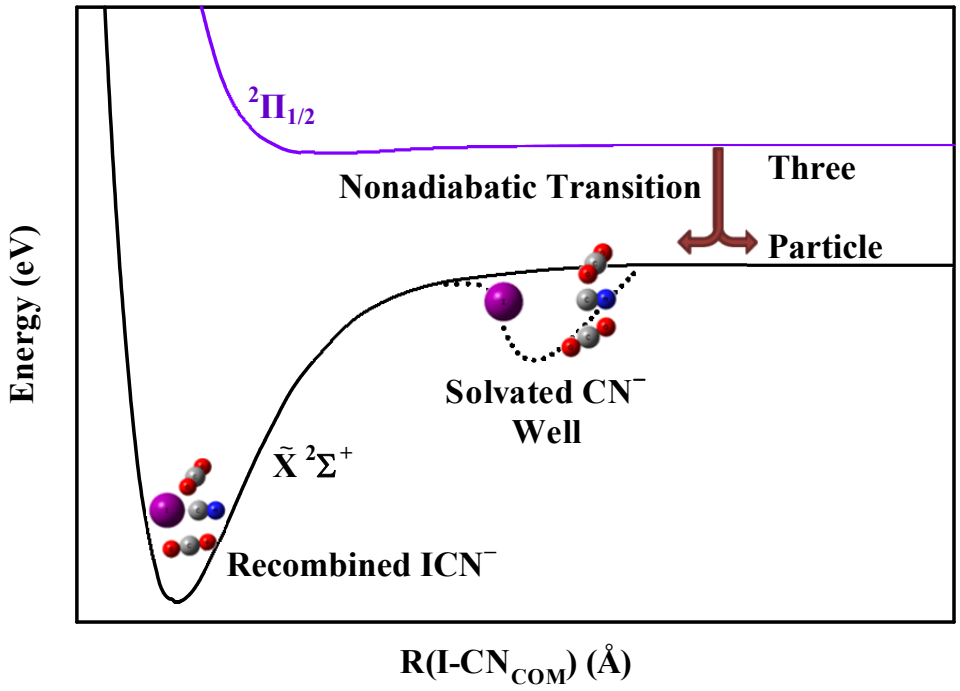

Figure 4.10 Schematic of linear ICN^- ground state (solid black) and $^2\Pi_{1/2}$ excited state (solid purple) as a function of the distance from the iodine atom to the center-of-mass of the CN diatom. The proposed well induced by solvation of CN^- is shown as a dashed line. The structures of the $ICN^-(CO_2)_2$ and $I–CN^-(CO_2)_2$ complexes are based off of previously calculated (Ref. 39) minimum energy structures of $IBr^-(CO_2)_n$.

Following photoexcitation of $ICN^-(CO_2)_n$, formation of the $NCCO_2^-$ molecule is proposed to occur on the ground state of the ICN^- chromophore and alters the photofragmentation dynamics of the dissociating cluster. Several experimental[30, 92-98] and theoretical[93, 95, 96, 98, 99] studies examined the solute-solvent interactions in $X^-(CO_2)$ (X = F, Cl, Br, I). Notably, Arnold *et al.*[93] utilized photoelectron spectroscopy to investigate the structure and energetics of the $X^-(CO_2)$ and reported the $F–CO_2$ bond in FCO_2^- is covalent in

nature. While $Cl^-(CO_2)$, $Br^-(CO_2)$, and $I^-(CO_2)$ are all reported to be weakly-bound van der Waals complexes, $D_o(X^-–CO_2) \approx 0.2–0.3$ eV, the FCO_2^- molecule is reported[93] to have a bond dissociation energy of 1.37 eV. Additionally, the excess charge is covalently shared by the F and CO_2 to such an extent that the O–C–O bond angle was reported[93] to be roughly 135°. Utilizing density functional theory (DFT) calculations, the bond dissociation energy of the ground electronic state of $NCCO_2^-$ is calculated to be 0.8 eV. The O–C–O bond angle in $NCCO_2^-$ is shown to be roughly 131°, see Fig. 4.11 (a), suggesting that the CN and CO_2 are not acting as a solute or solvent, respectively, but rather as a molecular anion. Because solvation of CN^- is favored, encounters between CN^- and the CO_2 solvent are likely to occur, increasing the chance of $NCCO_2^-$ formation. This interaction would result in an increased yield of CN^--based products observed.

If, during photodissociation of the ICN^- chromophore, a CO_2 solvent moved in between the iodine and the CN diatom, it is possible that a solvent-separated complex[100, 101] could form. The internuclear distances between the dissociating chromophore is expected to be large where nonadiabatic transitions are favored.[39] Therefore, the probability of a CO_2 solvent, positioned around the waist of ICN^- (see Sec. 4.4.4), moving between the iodine atom and CN is likely nonzero, resulting in a solvent-separated complex. Since the $NCCO_2^-$ molecule is energetically favored, it is possible that a solvent-separated-like complex forms in which the oxygen atoms of $NCCO_2^-$ point toward the iodine; Figure 4.11 (b) shows the calculated structure of the proposed solvent-separated-like complex. Due to the inability of the time-of-flight mass spectrometer to distinguish a solvated, recombined ICN^- photoproduct versus the solvent-separated-like complex in the present experiments, a solvent-separated-like complex may likely contribute to the yield of recombined photoproducts reported. Further experimental and theoretical studies are necessary

to determine the role of the $NCCO_2^-$ molecule and the solvent-separated-like complex in the dissociation dynamics of $ICN^-(CO_2)_n$.

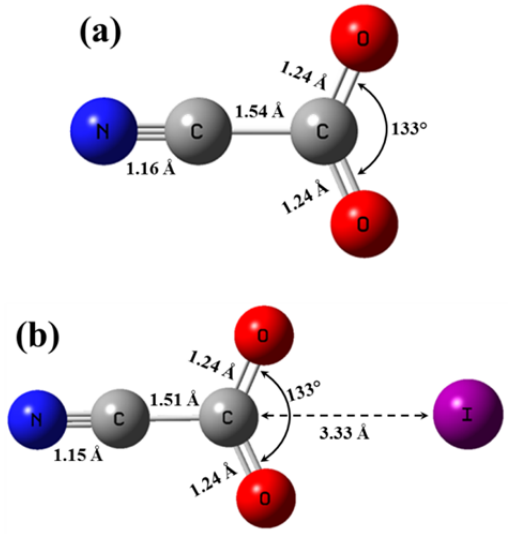

Figure 4.11 Optimized geometries of (a) the $NCCO_2^-$ molecule and (b) the solvent-separated-like complex. The structure of both complexes were calculated at the B3LYP/aug-cc-PVTZ level of theory, with the iodine electron core potential of Thompson (Ref. 102) utilized for (b).

4.4.4 Solvent Evaporation

To investigate the photofragmentation of $ICN^-(CO_2)_n$ further, it is informative to determine the solvation mechanism by examining the average number of solvent molecules lost for various cluster sizes. Figure 4.12 shows the average number of CO_2 solvent lost as a function of parent cluster size for the CN^--based photoproducts following 500 and 600 nm excitation of $ICN^-(CO_2)_n$. Additionally, the average number of CO_2 solvents lost for the Cl^--based products following 644-nm excitation[88] of $ICl^-(CO_2)_n$, is shown for reference. As seen in Fig. 4.12, all three curves show two distinct plateaus in the number of CO_2 solvent lost at intermediate and large values of n, and a positive slope in the transition region in between the plateaus. Although

no calculations have been performed to date to determine the minimum energy structures of the $ICN^-(CO_2)_n$, the behavior of the curves in Fig. 4.12 suggests solvation of ICN^- with CO_2 follows a process qualitatively similar to that previously reported for $ICl^-(CO_2)_n$.[33, 39, 77]

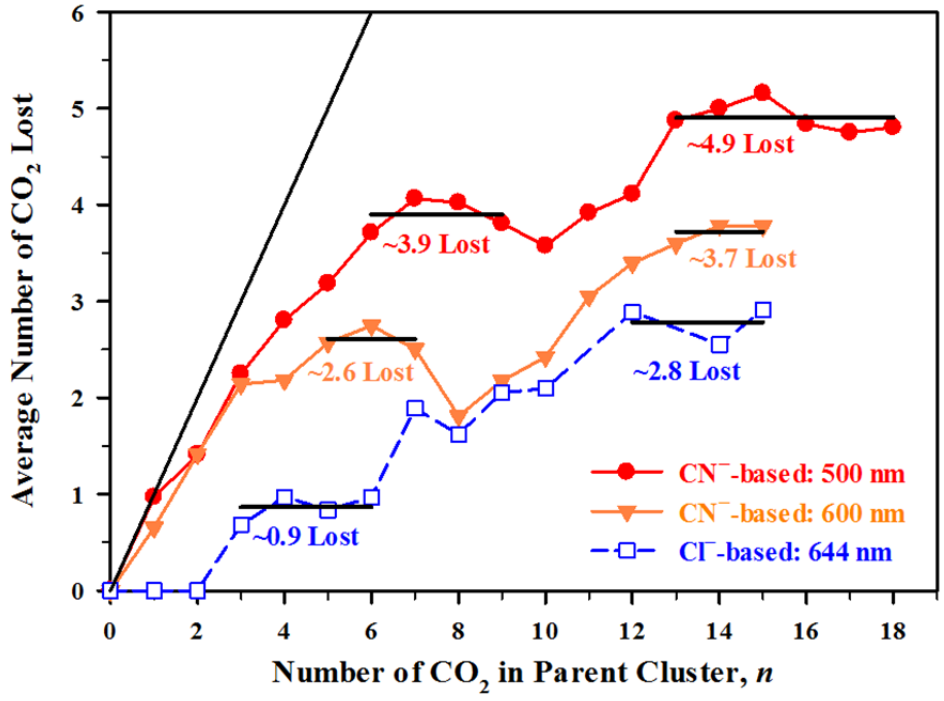

Figure 4.12 The average number of CO_2 lost from CN^--based photoproducts as a function of parent cluster size following 500 and 600 nm excitation of $ICN^-(CO_2)_n$. The number of CO_2 lost from Cl^--based products following 644 nm excitation of $ICl^-(CO_2)_n$ are also shown for comparison (Ref. 33). The solid-black diagonal line corresponds to the evaporation of all CO_2 solvent molecules from the parent cluster and is shown as a guide.

Solvation of a heteronuclear dihalide (IX^-, X = Cl, Br) with CO_2 has been shown[33, 39, 77] to begin around the waist of the chromophore. This location is energetically favored as a result of the quadrupole moment of CO_2 interacting with the delocalized excess charge on the

chromophore in the ground state equilibrium geometry. Subsequent solvation with CO_2 packs around the smaller end of the chromophore. Once the binding sites on the smaller end are filled, further solvation occurs around the iodine. Solvation on the iodine end of the chromophore is energetically unfavored and evaporation of CO_2 from the iodine end is expected to occur before evaporation from the smaller halide end.

Solvation of the CN end of the chromophore is expected to be energetically favored because of the difference in the ionic radii of CN^- and I^- (see Sec. 4.3). Thus, the first plateau in Fig. 4.12, $6 \leq n \leq 9$, is proposed to correlate with evaporation of CO_2 from the CN end of the chromophore, and, the second plateau, $13 \leq n \leq 18$, is proposed to be the result of evaporation from the larger iodine end of the chromophore. The transition region, $10 \leq n \leq 12$, corresponds to the solvent evaporation from both the iodine and CN ends of the chromophore, as solvation is shifting to the iodine end because all binding sites on the CN end are full. The slope of the curve in the transition region is expected to be positive because solvation of the iodine end of the chromophore will be less energetically favorable, resulting in a higher number of CO_2 lost following photoexcitation. As reported by Nadal,[88] the analysis of the curve for the average loss of CO_2 following photofragmentation of $ICl^-(CO_2)_n$ is performed in a similar fashion; the first and second plateaus correspond to solvation on the Cl and iodine end, respectively.

By considering the loss of CO_2 as a function of cluster size for the recombined photoproducts of $ICN^-(CO_2)_n$ photofragmentation, an approximate CO_2 solvent binding energy can be determined. This approximation must be determined from parent cluster sizes large enough to dissipate the excitation energy into solvent evaporation without resulting in an excited chromophore; therefore, data from the 400 nm study will not be included. Additionally, in the

case of $ICN^-(CO_2)_n$, it was assumed that no energy was partitioned to CN rotation in the large clusters and that *all* energy is distributed to the process of solvent evaporation; therefore, the approximation of the solvent binding energy is only an *upper bound*.

Following relaxation of the chromophore in the ground state well, the energy from photoexcitation is available for solvent evaporation.[36] The amount of solvent evaporated by the remaining energy depends on the solvent binding energy, the excitation energy, and the amount of energy partitioned to the kinetic energy of the evaporated monomer. The *upper limit* of the approximate solvent binding energy is determined by dividing the excitation energy by the number of solvent molecules lost for large cluster sizes.

A similar procedure has been utilized previously to estimate the monomer[70, 103-106] solvent binding energy in various clusters. Previously, the *upper limit* solvent binding energies for $I_2^-(CO_2)_n$, $IBr^-(CO_2)_n$, and $ICl^-(CO_2)_n$ were determined to be ~250 meV,[34, 87] ~260 meV,[35] and ~300 meV,[88] respectively. However, while studying Ar_n^+ and $(CO_2)_n^+$, Engelking[107] developed a statistical quasi-equilibrium theory/RRK model that determined roughly 20% of the energy in the *upper limit* approximation is partitioned to the kinetic energy of the departing solvent. Figure 4.13 shows the average number of CO_2 molecules lost as a function of parent cluster size for the ICN^--based photoproducts following 500 and 600 nm excitation of $ICN^-(CO_2)_n$. The solid black diagonal line in Fig. 4.13 corresponds to the loss of all solvent from the parent cluster. It is apparent from the Fig. 4.13 that solvent loss from the larger clusters ($6 \leq n \leq 15–18$) is strongly dependent on the excitation energy. Additionally, the solvent binding energy is expected to vary depending on the location of the solvent molecule with respect to the chromophore. To determine the change of the solvent binding energy with a change in location

on the chromophore an experimental binding enthalpy for I^-–CO2 and CN^-–CO_2 is required. Presently, the binding enthalpy for CN^- to a CO_2 molecule is unknown and, therefore, only the average CO_2 binding energy is calculated. Following 500 nm excitation, the average number of CO_2 molecules lost (represented by the solid black horizontal lines at large values of *n*) is 10; following 600 nm excitation an average of 8 CO_2 were lost. Therefore, the *upper limit* of the CO_2 solvent binding energy to ICN^- is determined to be ~246 meV and ~248 meV for 500 and 600 nm, respectively. By including the kinetic energy release of a CO_2 monomer, the approximate average CO_2 binding energy for the two wavelengths is roughly198 meV, with a loss to the kinetic energy of the monomer of roughly 49 meV. These quantities are consistent with the average CO_2 binding energies determined for $I_2^-(CO_2)_n$, $ICl^-(CO_2)_n$, and $IBr^-(CO_2)_n$.[34, 35, 87, 88] More experimental and theoretical studies are required to determine the average binding energy of a CO_2 molecule to the ICN^- chromophore when the CN rotation is included.

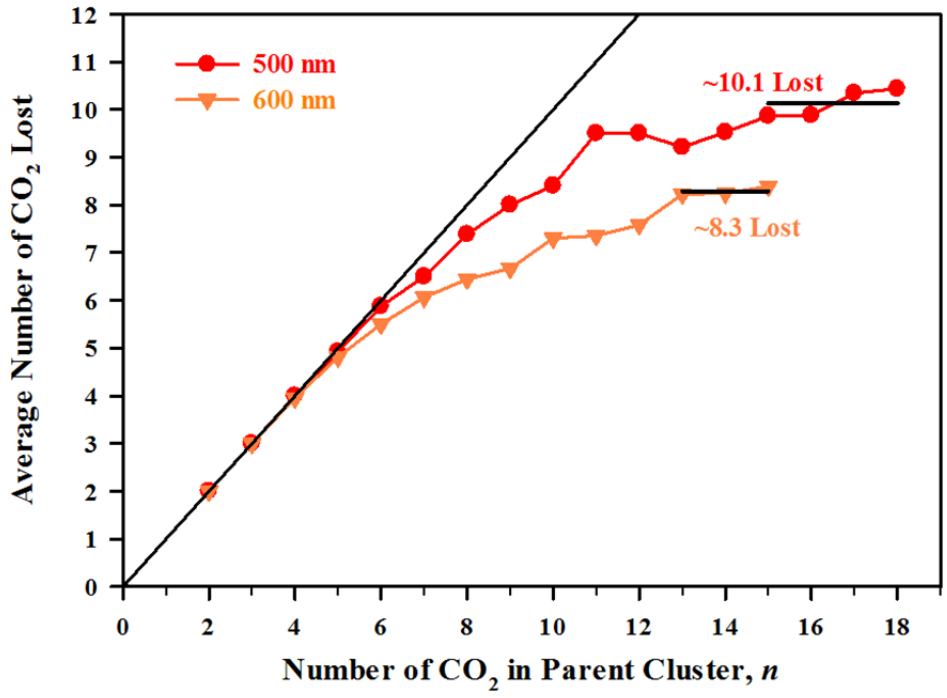

Figure 4.13 The average number of CO_2 lost from ICN^--based photoproducts as a function of parent cluster size following 500 and 600 nm excitation of $ICN^-(CO_2)_n$. The solid black *horizontal* lines show the average number of CO_2 lost for the largest clusters studied. The solid black *diagonal* line corresponds to the evaporation of all CO_2 solvent molecules from the parent cluster and is shown as a guide.

4.5 Comparison of $ICN^-(CO_2)_n$ and $ICN^-(Ar)_n$ Photofragmentation

Comparison of the ionic photoproduct distributions as a function of cluster size following 500 nm excitation of $ICN^-(CO_2)_n$ and $ICN^-(Ar)_n$ to the $^2\Pi_{1/2}$ excited state provides a microscopic picture of ICN^-–solvent interactions. Figure 4.14 shows the ionic photoproducts distributions of $ICN^-(CO_2)_n$ and $ICN^-(Ar)_n$ (n = 1–5) following 500 nm excitation. Following 500 nm excitation of $ICN^-(CO_2)_n$, the CN^--based photoproducts quickly dominate the ionic photoproduct distribution and the yield of recombined products varies as a function of n. Additionally, the

I^--based channel for $ICN^-(CO_2)_n$ quickly disappears, illustrating the dominance of nonadiabatic transitions. Conversely, following 500 nm excitation of $ICN^-(Ar)_n$, the I^--based photoproducts dominant the ionic photoproduct distribution, with only a roughly 6% contribution from recombined products for $1 \leq n \leq 5$.

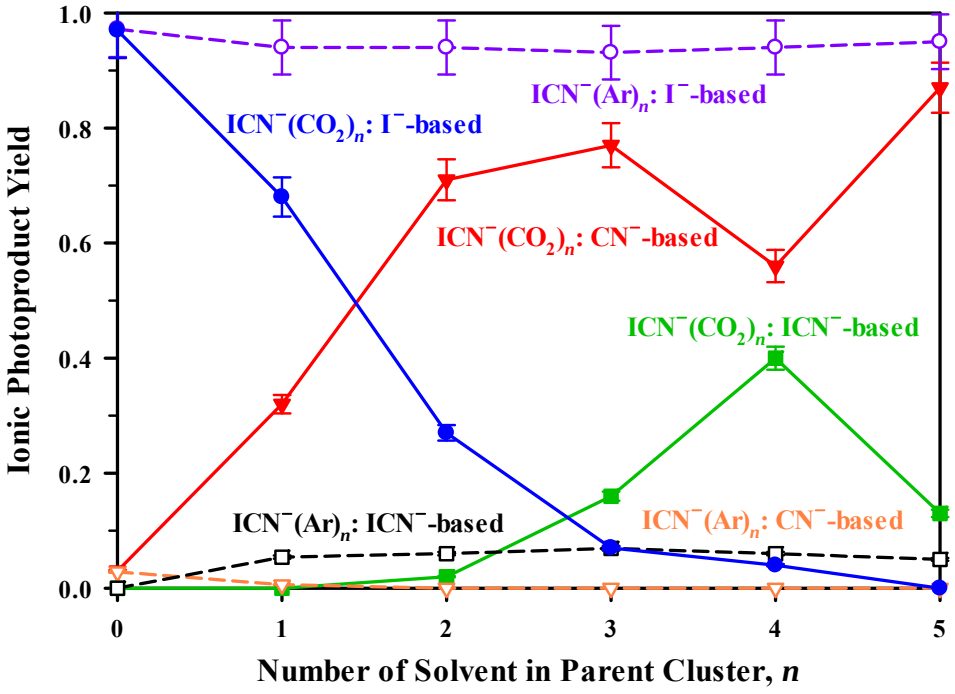

Figure 4.14 Ionic photoproduct distribution of $ICN^-(CO_2)_n$ and $ICN^-(Ar)_n$ (Chapter III) following one-photon 500 nm excitation to the $^2\Pi_{1/2}$ excited state. The error bars correspond to a 5% standard deviation and are plotted for each ionic product distribution.

The striking difference in the photofragmentation dynamics can be qualitatively understood by comparing the dominant electrostatic interactions between the two solvents and the ICN^- chromophore. The CO_2 solvent interacts strongly with the ICN^- chromophore because of its large quadrupole moment. This ion-quadrupole interaction has previously[33-36, 39, 76, 77] been

attributed to the initial CO_2 solvation around the bond axis of the chromophore. Additionally, the CO_2–CO_2 interactions are strong due to the quadrupole moment and result in the formation of a rigid cage around a chromophore, which is expected to promote recombination of a dissociating chromophore for large values of *n*. Conversely, Ar has neither a permanent dipole nor quadrupole moment and Ar–Ar interactions are weak, forming a loose network of solvent atoms.

Figure 4.15 shows the average number of solvent lost from the ICN^--based photoproducts as a function of the parent cluster size following 500 nm excitation of $ICN^-(CO_2)_n$ and $ICN^-(Ar)_n$. The solid black line in Fig. 4.15 represents the loss of all solvent in the parent following excitation. It is apparent from Fig. 4.15 that more solvent is evaporated following 500 nm excitation of $ICN^-(CO_2)_n$; this observation is seemingly in opposition to the fact that the energy required to evaporate CO_2 is approximately 4 times that of Ar. As proposed in Sec. 4.4.3, recombination of the chromophore following excitation of $ICN^-(CO_2)_n$ ($n \geq 4$) is likely the result of nonadiabatic transitions from the $^2\Pi_{1/2}$ excited state to the ground state introduced by perturbation of the electronic structure of the ICN^- chromophore from the solute-solvent interaction, leading to recombination in the ground state well. Similar photodissociation dynamics were observed[33, 35] following excitation of $ICl^-(CO_2)_n$ and $IBr^-(CO_2)_n$ to the $^2\Pi_{1/2}$ excited state. However, as presented in Chapter III, recombination following excitation of $ICN^-(Ar)_n$ is likely to occur following a radiative transition from a well in the $^2\Pi_{1/2}$ excited state to the ground. Therefore, the linear behavior of the number of CO_2 solvent molecules lost as a function of *n* (see Fig. 4.15) for $ICN^-(CO_2)_n$ adheres to a more statistical evaporation, like $ICl^-(CO_2)_n$ and $IBr^-(CO_2)_n$, in which recombination occurs *via* nonadiabatic transitions with coincident evaporation. In contrast, the number of Ar solvent atoms lost following 500 nm excitation of $ICN^-(Ar)_n$ does not follow the statistical model, revealing the alternative

recombination dynamics accessed by these clusters. Furthermore, the stronger ion-quadrupole interaction between the ICN^- chromophore and the CO_2 solvent and the more rigid CO_2 cage may hinder the rotation of the CN diatom following photodissociation. This may result in more energy partitioned to evaporation of solvent following 500 nm excitation of $ICN^-(CO_2)_n$ compared to $ICN^-(Ar)_n$. The current experimental results do not provide a definitive answer concerning the CN rotation without the aid of further experimental and theoretical studies.

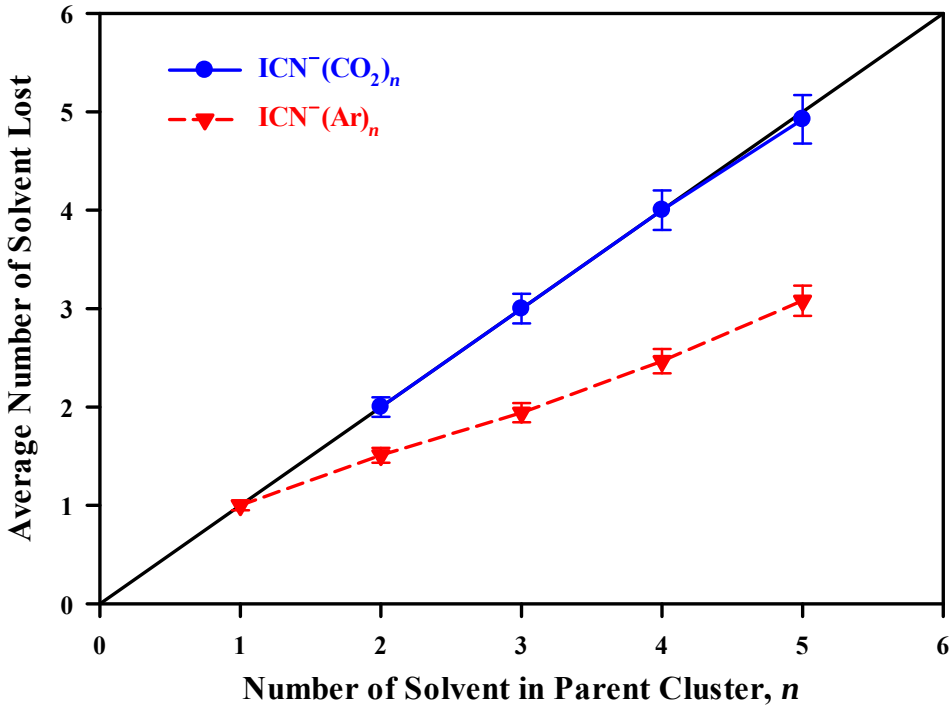

Figure 4.15 The average number of solvent lost from I^--based and ICN^--based photoproducts as a function of parent cluster size, *n*, following 500 nm excitation of $ICN^-(CO_2)_n$ and $ICN^-(Ar)_n$. See Chapter III for $ICN^-(Ar)_n$ photofragmentation results. The solid black line corresponds to the evaporation of all solvent from the parent cluster and is shown as a guide. The error bars correspond to a 5% standard deviation.

4.6 Recombination following photoexcitation of $ICN^-(CO_2)_n$, $I_2^-(CO_2)_n$, and $IBr^-(CO_2)_n$

Comparison of ICN^- photofragmentation with dihalide photofragmentation provides an informative perspective on the recombination of photodissociated chromophores. The bond dissociation energy of the chromophores, the solvent binding energies, the ionic radii, and the asymptotic dissociation products are all qualitatively similar for ICN^-, I_2^-, and IBr^-; however, the yield of recombined photoproducts following excitation to the $^2\Pi_{1/2}$ excited state varies dramatically between solutes. Figure 4.16 shows the yield of recombined photoproducts following 600 nm excitation of $ICN^-(CO_2)_n$, 720 nm excitation of $I_2^-(CO_2)_n$,[87] and 760 nm excitation of $IBr^-(CO_2)_n$.[51] At these wavelengths, roughly 0.4 eV of kinetic energy is released to each cluster at the $^2\Pi_{1/2}$ excited state asymptote. (The yield of recombined products for $ICl^-(CO_2)_n$ is not shown in Fig. 4.16 because a study utilizing an excitation energy that results in 0.4 eV of energy release has not been performed to date). As can be seen in Fig. 4.16, the addition of two solvent molecules is sufficient to allow for nonadiabatic transitions from the $^2\Pi_{1/2}$ state to the ground state, resulting in recombined products for both ICN^- and IBr^-. Addition of the third CO_2 results in a peak in the ICN^--based product yield and an increase in the yield of IBr^--based products. However, subsequent solvation results in a decrease in the yield of ICN^--based products, while the yield of IBr^--based products continues to increase. When $n = 5$, roughly 88% of the observed ionic photofragments are IBr^--based products, but ICN^--based products only account for roughly 20% of the ionic photoproducts; no recombined photoproducts are observed for $I_2^-(CO_2)$, $n = 0$–5. For $4 \leq n \leq 11$, the yield of recombined ICN^--based products varies between ~10–20%, but does not dependent on parent cluster size. When $n \geq 13$, the yield of ICN^--based products increases, but never overcomes roughly 50% of the ionic photoproducts observed. Recombined I_2^- photoproducts are first observed when $n = 6$ and the yield of

recombined I_2^- products increases as n increases. The yield of recombined products for both $IBr^-(CO_2)_n$ and $I_2^-(CO_2)_n$ reaches 100% at $n = 8$ for $IBr^-(CO_2)_n$ and $n = 17$ for $I_2^-(CO_2)_n$.

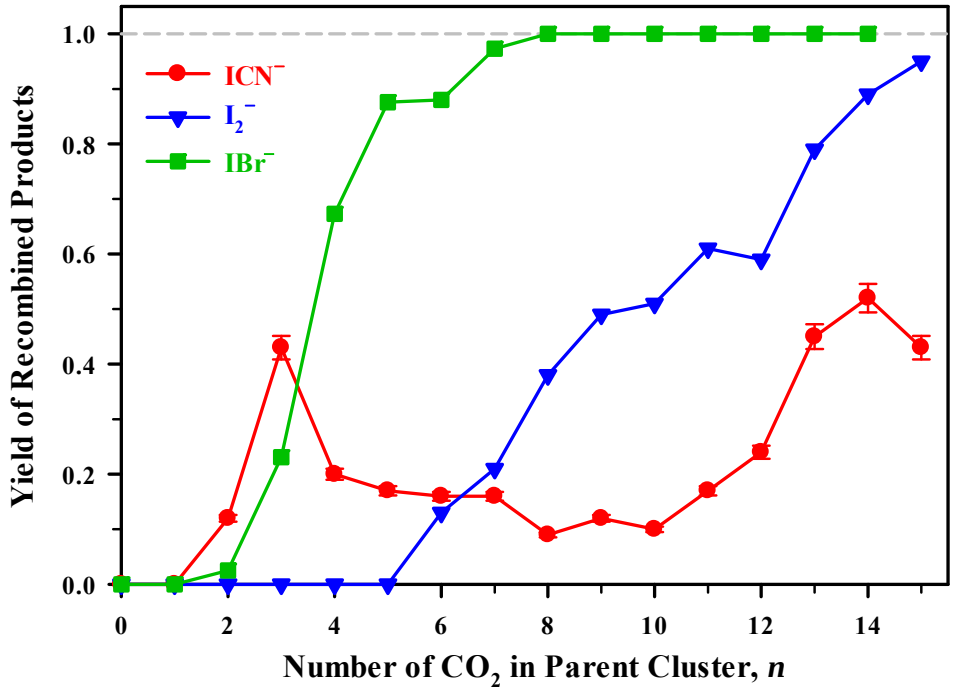

Figure 4.16 Yield of recombined photoproducts following excitation of $ICN^-(CO_2)_n$, and $I_2^-(CO_2)_n$, (Ref. 87) and $IBr^-(CO_2)_n$ (Ref. 51) to the $^2\Pi_{1/2}$ excited state. The excitation wavelengths utilized result in roughly 0.4 eV of kinetic energy release for each solute. The dashed gray line represents 100% recombined photoproducts. The error bars on the $ICN^-(CO_2)_n$ photoproducts correspond to a 5% standard deviation.

The marked contrast in the yield of recombined photoproducts can be qualitatively understood by comparing the structures of the three clusters as a function n. Papanikolas *et al.*[108] performed Monte Carlo simulations to report the minimum energy structure of $I_2^-(CO_2)_n$. Their simulations showed that for $n \leq 6$, the CO_2 solvent binds to I_2^- around the waist of the chromophore and equally solvates both iodine atoms. This structure does not allow

recombination for $n \leq 6$, as the dissociation of the chromophore is unimpeded by the solvent. However, for $n \geq 7$, the solvation of I_2^- begins to occur at one end of the chromophore and the yield of recombined photoproducts begins to increase as n increases. Similar to $I_2^-(CO_2)_n$, the first few ($n \leq 4$) CO_2 molecules solvate IBr^- around the bond axis.[35, 39] Additional solvation results in the Br end of the chromophore becoming enclosed by a CO_2 cage. Solvation of the Br end of the chromophore increases the yield of recombination significantly, and the only photoproducts observed by $n = 8$ are IBr^--based. The solvation of $ICN^-(CO_2)_n$ is expected to occur in a similar fashion to $ICl^-(CO_2)_n$, see Sec. 4.4.4; initial solvation occurs around the waist of ICN^- and continues around the smaller end of the chromophore. However, as Fig. 4.16 shows, following the addition of the fourth CO_2, photoexcitation of $ICN^-(CO_2)_4$ with 600 nm light results in a decrease in the yield of recombined products. This decrease is the result of the favorable solvation of CN^- and the likely formation of the $NCCO_2^-$ molecule which becomes trapped in the ground state well at large internuclear distances introduced by the CO_2 solvating CN^- (detailed in Sec. 4.4.3). The yield of recombined products reduces to ~10–20% for $4 \leq n \leq 11$, but for $n = 13$–15, it again begins to increase. It is proposed that this increase is the result of solvation beginning to significantly enclose the iodine end of ICN^- giving rise to an increased yield of recombined products. This explanation is the same proposed in Sec. 4.4.4 to account for the average number of CO_2 lost as a function of cluster size in the large cluster limit.

4.7 Summary and Conclusions

Results of photofragmentation studies of $ICN^-(CO_2)_n$ following 400, 500, and 600 nm excitation show a disparity in ionic photoproduct distributions compared to previously studied dihalides due to intrinsic properties of the solute and the location of solvation about the

chromophore. Furthermore, comparison of the results of photofragmentation of $ICN^-(CO_2)_n$ and $ICN^-(Ar)_n$ reveal the importance of solute-solvent interactions in photofragmentation dynamics. Results of photodissociation action spectra reveal the stabilization of the $^2\Pi_{1/2}$ excited state upon solvation of the ICN^- chromophore with CO_2. Following 500 or 600 nm excitation of $ICN^-(CO_2)_n$ to the $^2\Pi_{1/2}$ excited state, CN^--based photoproducts dominate following the addition of roughly two CO_2 solvent molecules. This result is likely due to nonadiabatic transitions from the $^2\Pi_{1/2}$ state to the $^2\Sigma^+$ excited state for n = 1–3, and nonadiabatic transitions from the $^2\Pi_{1/2}$ states to the $\tilde{X}\ ^2\Sigma^+$ state are most probable when $n \geq 4$. The yield of recombined ICN^--based photoproducts observed reaches a maximum at small values of n; n_{max} increases with an increase in excitation energy. The sudden decrease in the yield of ICN^--based products following this local maximum is the result of the favorable solvation of CN^- and the formation of the $NCCO_2^-$ molecule or a solvent-separated-like complex. Analysis of the average number of CO_2 molecules lost as a function of cluster size for the CN^--based products provides evidence of the location of the solvent about ICN^- as n increases. Additionally, examination of the average number of CO_2 molecules lost for the ICN^--based products as a function of cluster size provides an approximation of the CO_2 solvent binding energy (~198 meV), but does not include the possibility of energy partitioned into CN rotation. Comparison of the photofragmentation of $ICN^-(CO_2)_n$ and $ICN^-(Ar)_n$ illustrates the central role of the solvent in the dissociation dynamics, while comparison to $I_2^-(CO_2)_n$, $IBr^-(CO_2)_n$, and $ICl^-(CO_2)_n$ elucidates the role of the solute.

Chapter V: Recombination Dynamics of Photodissociated $IBr^-(CO_2)_n$

5.1 Introduction

The study of ultra-fast cluster dynamics has long been a field of interest allowing for the investigation of the behavior of molecules influenced by their environments.[109, 110] Simplification of the local environment by using gas phase cluster ions provides one the chance to study these influences and gain a fundamental understanding of the effects solvation has on molecules.[109, 111-113] These effects can be seen in simple processes such as solvent molecules being used to dissipate energy or more complex interactions involving perturbation of the electronic character of the solvated chromophore. Phenomena resulting from solvent perturbed potential energy surfaces, such as solvent-induced recombination and "cage effects," can be studied using molecular dynamics with the application of simple, first-order kinetic models.

Over the past 15 years, the Lineberger and Parson groups have carried out a collaborative theoretical and experimental investigation into the dynamics of photodissociation of diatomic molecular ions embedded in mass-selected molecular clusters.[33, 34, 37, 76, 114-120] A common theme that runs through much of this work has been the systematic measurement of the cluster size dependence of product branching ratios, such as the relative probabilities of dissociation vs. solvent-induced recombination, and of the time constants for the associated processes. Earlier work in this series reported[38] a surprising disparity between the overall propensity for solvent-induced recombination following near-IR excitation, and the rate of this recombination process. For example, as the number of CO_2 solvents around IBr^- was increased from 5 to 8, the recombination probability increased[35] from 90% to 100%, but the timescale for recombination

increased from 12 ps to 900 ps.[38] This result is in dramatic variance with earlier investigations of the homonuclear dihalide cluster $I_2^-(CO_2)_n$, where somewhat more kinetic energy was available to the photofragments and for which recombination times were of order 10 ps and **decreased** with increasing cluster size.[37, 120] The results of nonadiabatic molecular dynamic simulations, which reproduced these experimental trends, were also included in the earlier papers.[76, 114, 118, 121] On the basis of the $IBr^-(CO_2)_n$ simulations, it was predicted that the trend in recombination time would reverse as the cluster size was increased further. The experiments presented in this chapter involve the recombination of photodissociated, size-selected $IBr^-(CO_2)_n$, n = 11–14, anionic clusters;[39] they were designed to test the above prediction, and to provide additional physical understanding of this very unexpected result. Results of earlier experiments and theory are presented only to the extent required to provide a context for these new results and the resulting fuller interpretation.

5.2 Experimental

A pump-probe technique is utilized to study solvation-induced recombination dynamics of photodissociated $IBr^-(CO_2)_{11\text{-}14}$. The experimental apparatus, laser system, and data acquisition methods corresponding to this experiment were previously discussed in Chapter II. Briefly, a one-color (795-nm) pump-probe scheme is employed to measure the absorption recovery times for the $IBr^-(CO_2)_n$ cluster anions.[38] Photoexcitation of the dihalide at this wavelength excites IBr^- to the dissociative $\tilde{A}'\ ^2\Pi_{1/2}$ state, leading to I^- and Br products with ~0.29 eV kinetic energy release. As CO_2 solvent molecules are added, the ionic photoproducts change to Br^-- and IBr^--based products with varying degrees of solvation, indicating dissociation on the ground state surface or recombination of the chromophore, respectively.[35] With eight or

more solvent molecules attached to the chromophore, the only observed photoproducts are IBr^--based, indicating 100% recombination.[35] Once recombined and sufficiently vibrationally relaxed on the ground state, the chromophore regains near-IR absorption and can again be excited to the $\tilde{A}'\ ^2\Pi_{1/2}$ state *via* the 795 nm probe pulse. Following the absorption of a second photon, the ionic photoproducts have a mass-to-charge ratio different from any of the one-photon products due to solvent evaporation. Two-photon products are then monitored as a function of pump-probe delay time, taking advantage of the fact that the electric potential of the secondary reflectron mass spectrometer can be adjusted to detect only products of pump and probe laser absorption.[38] Appropriate background corrections are applied to assure that the reported two-photon signal results only from the absorption of one photon from each of the pump and probe laser pulses.[36, 37, 122]

5.3 Theoretical Methods

The theoretical work presented in this section was performed by Matthew A. Thompson and a detailed description can be found elsewhere;[102] therefore, only a brief description of those results that are required to understand the experimental data is presented here.

5.3.1 Electronic Structure

The potential energy curves, Fig. 5.1, and associated electronic properties of the isolated IBr^- solute were obtained using MOLPRO 2002,[123] with the energy-consistent effective core potential (ECP) of Stoll *et al*.[124] The electronic structure calculations use the internally-contracted multireference configuration interaction (icMRCI) methods developed by Knowles and Werner.[125-127] The reference orbitals and configurations are obtained from

state-averaged complete active-space self-consistent field calculations[128, 129] that consist of 15 electrons in the lowest two Σ, Π_x, and Π_y states that arise from the ^2P state of the neutral and ^1S state of the ion. A spin-orbit calculation of all six states is then performed using spin-orbit ECPs.[130] Other electronic properties of IBr^- are tabulated and compared with experiment in Table 5.1.

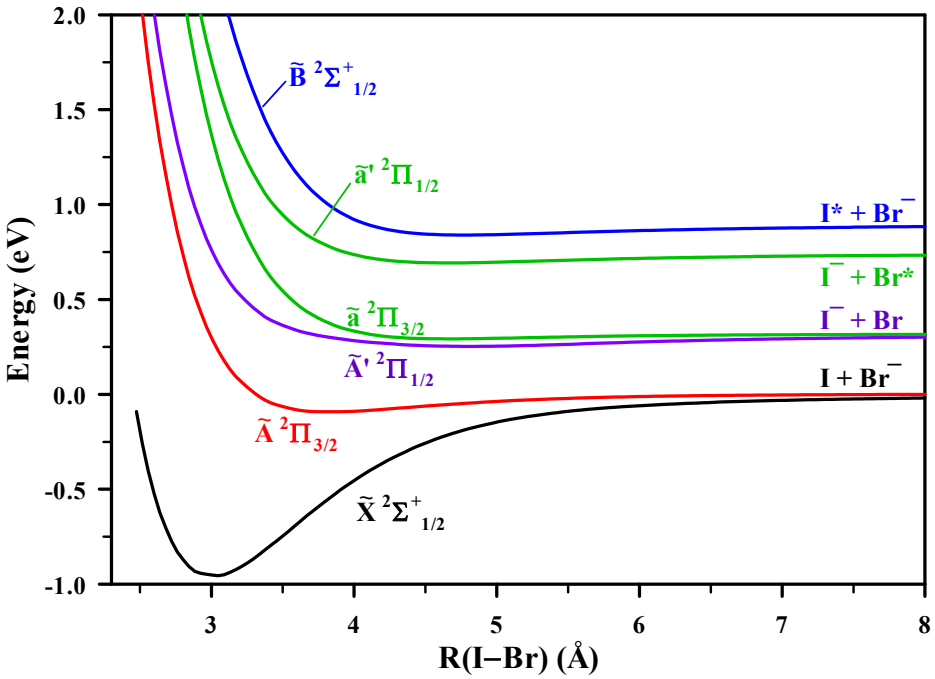

Figure 5.1 Potential energy curves for the six lowest spin-orbit states of IBr^-.

Table 5.1 Summary of energetics from *ab initio* calculations (energies in eV)

		Calc.	Expt.	Δ(Calc. – Expt.)
Spin-Orbit Splitting	Br	0.4237	0.4569[a]	−0.0331
	I	0.8932	0.9427[a]	−0.0495
	ΔEA(I–Br)	0.3156	0.3045[b]	0.0111
	$D_0(IBr^-)$	0.948[d]	1.10(4)[c]	−0.152
			0.966[e]	−0.018
	EA(IBr)	2.494	2.51(2)[e]	−0.016
	R_e (Å)	3.05	3.06(3)[e]	−0.01

[a]Ref. 74
[c]Ref. 91
[d]Calculated using $\omega_e = 118$ cm^{-1}, as obtained by analysis of the ground state potential energy curve with LeRoy's LEVEL program, Ref. 131
[e]Ref. 35
[f]Ref. 69

5.3.2 Molecular Dynamics

The nonadiabatic molecular dynamics (MD) simulations for $IBr^-(CO_2)_n$ are based on the effective Hamiltonian method developed by Maslen *et al.*[132] and previously applied[76, 115, 116, 118, 121] to $I_2^-(CO_2)_n$. Briefly, the electrostatic and induction interactions between the IBr^-solute and the CO_2 solvent are calculated from an operator including electrostatic and induction terms for the solute and solvent. For the solute, a distributed multipole analysis (DMA) (Ref. 133) of the isolated solute electronic structure is calculated. At each time step of a molecular dynamics simulation, the effective Hamiltonian for the solvated ion is diagonalized to yield the energies, forces, and nonadiabatic transition probabilities needed for the next step.

5.3.3 Minimum Energy Structures

Long time simulations on the ground electronic state surface are used to obtain energies and structures for the solvated chromophore. Minimum energy structures for $IBr^-(CO_2)_n$ (n = 1–16) are constructed by sampling 201 configurations from a 1 ns trajectory on the IBr^- ground state having an energy corresponding to a temperature of 80 K. These configurations are then quenched to local minima.[134] The lowest energy structure obtained for each cluster size is shown in Fig. 5.2, and the corresponding energetic properties are reported in Table 5.2. While this procedure is not expected to find the lowest energy configuration for any but the smallest clusters, the structures reported in Fig. 5.2 and Table 5.2 are characteristic of the minimum energy configurations of the cluster anions. The most striking visual feature of these minimum energy structures is the changing asymmetry of the solvent configurations, with maximum asymmetry near a half-filled first solvation shell. This asymmetry plays a major role in the unusual recombination dynamics.

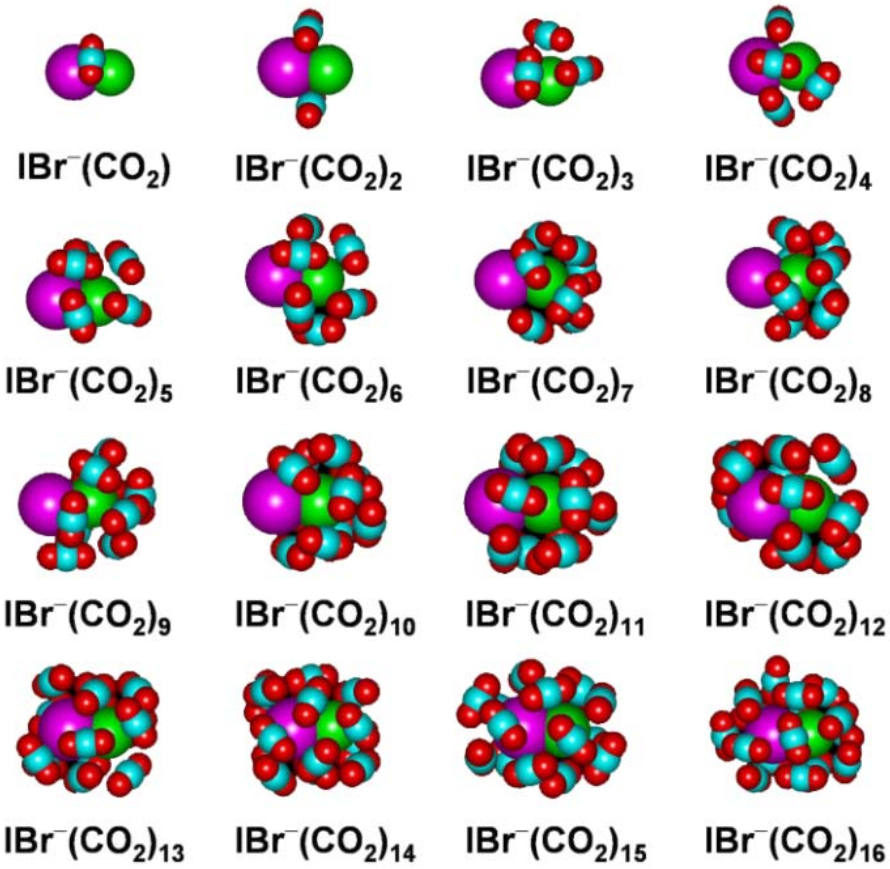

Figure 5.2 Exemplar calculated minimum energy structures for $IBr^{-}(CO_2)_n$, n = 1–16. The pattern of CO_2 filling is first around the bond, next the Br end beginning at n = 3, and then the iodine end beginning at n = 9.

Table 5.2 Properties of minimal energy clusters of $IBr^-(CO_2)_n$ from 80 K trajectory ensembles

n	**PE (meV)[a]**	**Δ*n* (meV)[b]**	**−PE/*n* (meV)**	**# local min.**
1	−205	205	205	1
2	−406	201	203	23
3	−627	222	209	22
4	−852	225	213	47
5	−1074	222	215	65
6	−1301	227	217	98
7	−1525	224	218	104
8	−1775	251	222	63
9	−2009	233	223	64
10	−2248	240	225	112
11	−2483	234	226	135
12	−2680	198	223	111
13	−2917	237	224	126
14	−3157	240	225	143
15	−3380	223	225	131
16	−3588	208	224	140

[a]Not including IBr^- bond energy (0.956 eV).
[b]See Eq. (1).

To quantify this concept, we define the asymmetry of a solvent configuration, ΔΦ, as the energy required to move a charge of −e from the iodine end to the Br end of a cluster. Negative values mean solvation favors bromine, while positive values favor iodine. Figure 5.3 shows the solvent asymmetry for ground state $IBr^-(CO_2)_n$ averaged over an ensemble of clusters at 60 K. This asymmetry is maximum near a half-filled solvent shell, consistent with the geometrical structures.

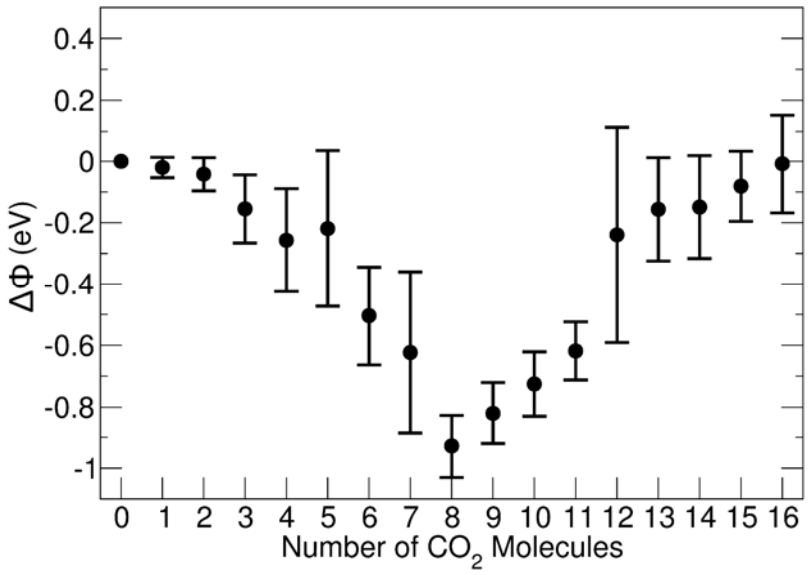

Figure 5.3 Average ΔΦ for 100 configurations of $IBr^-(CO_2)_{0\text{-}16}$ in the ground state at 60 K. Error bars represent one standard deviation of the mean.

5.3.4 Trajectory Calculations

Ensembles for MD simulations are constructed as follows. First, starting from the calculated minimum energy structures, the cluster is warmed for 40 ps at a temperature of 60 K, followed by a 100 ps run on the ground state to test that the cluster energetics are stable. After that, the ensembles are constructed using a 2 fs time-step run on the electronic ground state that samples every 5 ps until 100 configurations are constructed. A step-size of 1 fs is used for all trajectories. A trajectory is classified as "dissociated" if the solute bond length ever exceeded 40 a_0 on any electronic surface, and as "recombined" if it ever became less than 3.3 Å on the ground state. As discussed in the next section, the timescales for recombination in the intermediate-sized clusters (n = 8–10) are extremely long,[38] and in these cases it is not feasible to follow every trajectory in an ensemble all the way to its final destination. In these cases, we propagate the ensemble until enough trajectories have recombined that we can calculate a

recombination time – this requires as much as 2 ns in extreme cases – and then extrapolate the branching ratio for recombination on the basis of the fraction of trajectories that have dissociated or recombined at this time.

5.4 Experimental Results

5.4.1 Absorption Recovery Dynamics of $IBr^-(CO_2)_n$, n = 11–14

The absorption recovery times of the smaller $IBr^-(CO_2)_n$ clusters, n = 5−10, following 795 nm excitation to the $\tilde{A}'\ ^2\Pi_{1/2}$ state were previously reported by our group.[38] It was found that the absorption recovery time increased as the number of CO_2 molecules in the cluster increased from tens of picoseconds for $IBr^-(CO_2)_{5,6}$ to almost 1 ns for $IBr^-(CO_2)_{8,10}$. While this cluster size dependence is the opposite of that observed[37, 120, 122] for $I_2^-(CO_2)_n$, $I_2^-(OCS)_n$, and $I_2^-(Ar)_n$, it has been corroborated by theoretical predictions. Furthermore, these predictions indicated that for even larger clusters, n = 12 and 13, the absorption recovery lifetime should return to tens of picoseconds as with $IBr^-(CO_2)_{5,6}$. At that time, experimental difficulties prevented the formation of the larger ion clusters. The cluster ion production difficulties have now been resolved and experimental results for these and other larger clusters are presented here.

Figure 5.4 shows the time-dependent absorption recovery of $IBr^-(CO_2)_{11}$. The transient is obtained by using a weighted average of the signal resulting from four days of data acquisition of the IBr^- and $IBr^-(CO_2)$ two-photon products. Plotted individually, these two products exhibited very similar absorption recovery transients. However, the appearance of the transients changed slightly on a day-to-day basis. The y-axis in Fig. 5.4 represents the two-photon, pump-probe signal normalized to unity at the signal level observed at a 500 ps time delay. The transient

recombination signal shows a steep, initial rise from slightly greater than 0 ps to 30 ps and then a more gradual rise until 650 ps. While all the data sets show the steep, initial rise from 0 ps to 30 ps, the more gradual rise out to 650 ps is only observed in two of the four data sets. Given that the existence of this very slow rise is almost totally dependent on the 50 ps data, its existence must be considered as tentative at best. Because both the pump and probe pulses are the same wavelength, the signal is symmetric about $t = 0$. When the pump and probe beams overlap temporally, we see a large "coherence peak" whose shape is essentially the autocorrelation function of the 795 nm laser pulse. When fitting the absorption recovery data, however, we avoid this artifact with the physically compelling assumption that there can be no recombination at time zero,

$$N(t) = 1 - e^{-\frac{t}{\tau}} \tag{5.1}$$

where τ represents the absorption recovery lifetime. Fitting to this model yields a value of 7(2) ps for τ. This fit is shown as the dotted line in Fig. 5.4. The experimental data also hint at the possibility of a long recovery time for a small (possibly 10 %) component of the $IBr^-(CO_2)_{11}$ clusters; however, given the day-to-day fluctuations associated with the data sets, a definitive conclusion cannot be made. Regardless of the exact functional form of the fit that is utilized, though, it is clear that the principal absorption recovery occurs much more rapidly than was observed for the $IBr^-(CO_2)_8$ and $IBr^-(CO_2)_{10}$ clusters, 900(100) ps. This result is in accord with theoretical predictions that the absorption recovery time should decrease for larger $IBr^-(CO_2)_n$ clusters.[38]

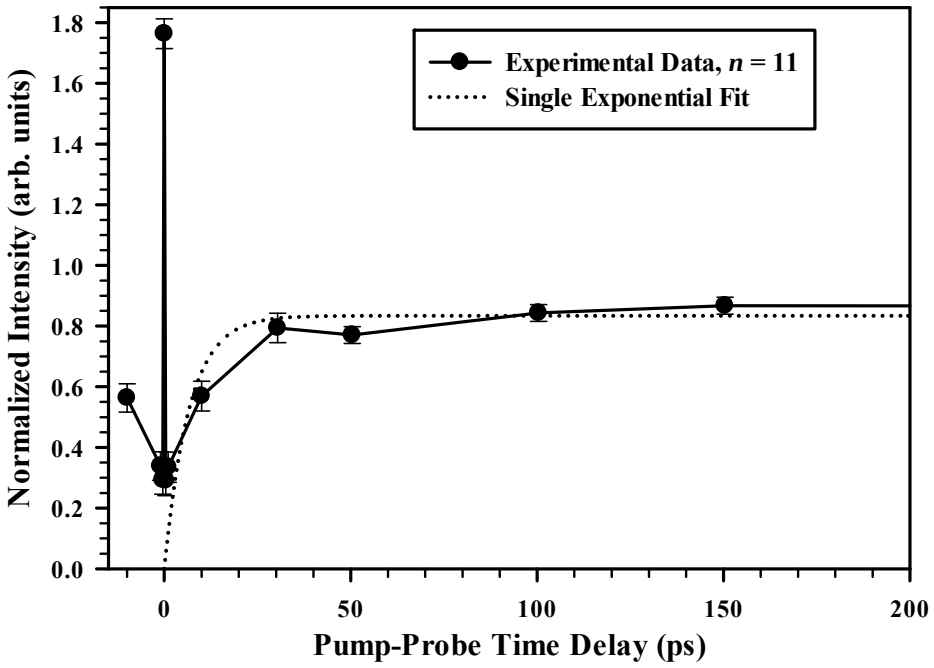

Figure 5.4 Transient illustrating the absorption recovery of $IBr^-(CO2)_{11}$. The circles represent the experimental data, and the dotted line is the result of a single exponential fit. The black line is used to guide the eye.

The $IBr^-(CO_2)_{12}$ absorption recovery dynamics are qualitatively similar to those observed for $IBr^-(CO_2)_{11}$. In this case, however, only the $IBr^-(CO_2)$ two-photon product was detected. Furthermore, no evidence was observed for a second time constant. A single exponential fit of the data yielded a lifetime of 10.3(8) ps, in further support of the theoretical predictions for the larger $IBr^-(CO_2)_n$ clusters.[38]

The transient depicting the absorption recovery of $IBr^-(CO_2)_{13}$ is illustrated with filled squares in Fig. 5.5. This transient was obtained by summing data from the $IBr^-(CO_2)$, $IBr^-(CO_2)_2$, and $IBr^-(CO_2)_3$ two-photon products and then normalizing the (constant) signal level at 100 ps to unity. Clearly, this transient is much more complicated than that observed for $IBr^-(CO_2)_{11}$. There is a sharp initial rise from 0.4 to 1 ps, then a plateau at 3–5 ps, and finally a

decrease and leveling off of the signal by 10–20 ps. Data were recorded for time delays as long as 500 ps, and no significant changes in the signal intensity were observed after 20 ps. It is interesting to note that the signal at 3–5 ps actually exceeds that at 100 ps. A qualitative explanation for this behavior is given below. It is clear, however, that unlike the data for $IBr^-(CO_2)_{11}$ and $IBr^-(CO_2)_{12}$, this transient cannot be accurately fitted with a simple exponential rise. We are left, then, to make only a qualitative estimate of the absorption recovery time, as discussed below.

As shown by the filled circles in Fig. 5.5, a transient was also recorded for $IBr^-(CO_2)_{14}$. This transient was acquired by summing the $IBr^-(CO_2)_2$, $IBr^-(CO_2)_3$, and $IBr^-(CO_2)_4$ two-photon products. The intensity was again normalized to unity at the signal level at 100 ps. Note that this transient is qualitatively similar to that observed for $IBr^-(CO_2)_{13}$. A sharp rise is observed from 0.4 to 1.0 ps, along with a peak at 4 ps, and a gradual decay and leveling off of the signal by 10 ps. As with $IBr^-(CO_2)_{13}$, data were taken out to a 500 ps time delay, and no significant changes in the signal level were observed at long time delays. Thus, the experiments do not confirm the predictions by theory that the absorption recovery of $IBr^-(CO_2)_{14}$ should consist of both a fast and slow component (see Section 5.4.2). The peak of the transient at 4 ps is much more pronounced in the absorption recovery of $IBr^-(CO_2)_{14}$ than in the recovery of $IBr^-(CO_2)_{13}$, as is evidenced by the magnitude of the y-scale; the signal level at 5 ps for $IBr^-(CO_2)_{13}$ is approximately 1.05, while that observed at 4 ps for $IBr^-(CO_2)_{14}$ is approximately 1.4. Interestingly, depending on the particular product detected for $IBr^-(CO_2)_{14}$, the magnitude of the peak also varied. Higher mass products gave rise to a larger peak in the transient. These observations are consistent with our picture of the absorption recovery for $IBr^-(CO_2)_{13}$ and $IBr^-(CO_2)_{14}$, as discussed below. Finally, as with $IBr^-(CO_2)_{13}$, it is impossible to get an accurate

absorption recovery lifetime by fitting the data to an exponential rise. Thus, we are again left to qualitatively assign an absorption recovery lifetime, as discussed in the following paragraph.

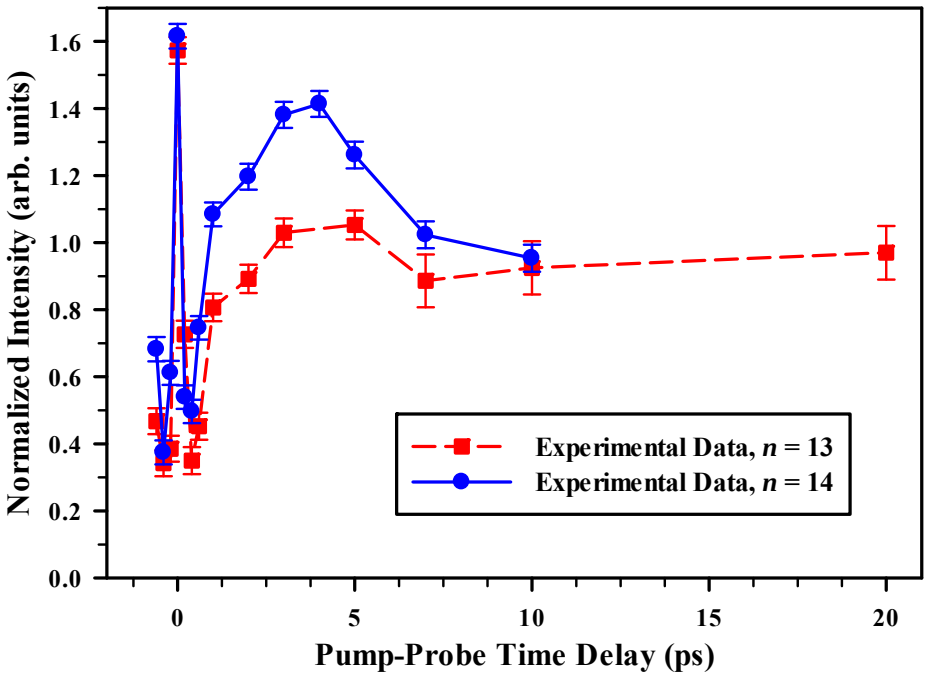

Figure 5.5 Absorption recovery transient for $IBr^-(CO_2)_{13}$, dashed line and squares, and $IBr^-(CO_2)_{14}$, solid line and circles. The lines are shown to guide the eye.

The nonexponential behavior observed in the transients for $IBr^-(CO_2)_{13}$ and $IBr^-(CO_2)_{14}$ shown in Fig. 5.5 is attributed to population traversing vibrationally excited states of the ground electronic state after recombination. The absorption cross section of the $\tilde{A}' \leftarrow \tilde{X}$ transition for IBr^- peaks at 740 nm.[51] This implies that excitation from a 795 nm laser pulse, the wavelength used in these experiments, will have a greater cross section from vibrationally excited levels in the ground electronic state than from the lowest vibrational levels. Figure 5.6 illustrates this with a schematic of the excitation of the chromophore from the lowest vibrational level, $h\nu_{asym}$, and

from an excited vibrational level, $h\nu_{overshoot}$. The sharp rise observed in the transients for n = 13 and 14 from 0.4 ps to 1.0 ps, then, is attributed to population traversing high vibrational states in the ground electronic state. The transient then peaks above the normalization point at 4 ps, at which time recombined population is traversing intermediate vibrationally excited levels. This is illustrated by the $h\nu_{overshoot}$ arrow in the figure. Finally, the transient reaches the asymptotic level at 10 ps when the population has reached low vibrational levels, as shown by the $h\nu_{asym}$ arrow. Based upon this description of the transients observed for $IBr^-(CO_2)_{13}$ and $IBr^-(CO_2)_{14}$, we assign their absorption recovery lifetimes as 5(3) and 4(2) ps, respectively. This picture also supports our observation that the higher mass products for $IBr^-(CO_2)_{14}$ give rise to a larger peak in the transient because higher mass products are less likely to make it back down to the lowest vibrational levels in the ground state. Thus, they will be more prevalent in the intermediate vibrational levels which correspond to the signal responsible for the peak in the transient. Of note is that the theoretical methods used in simulating the absorption recovery dynamics of these clusters, as outlined in the following section, do not account for the change in the IBr^- cross section as a function of vibrational level and therefore will not reproduce the peak in the transient.

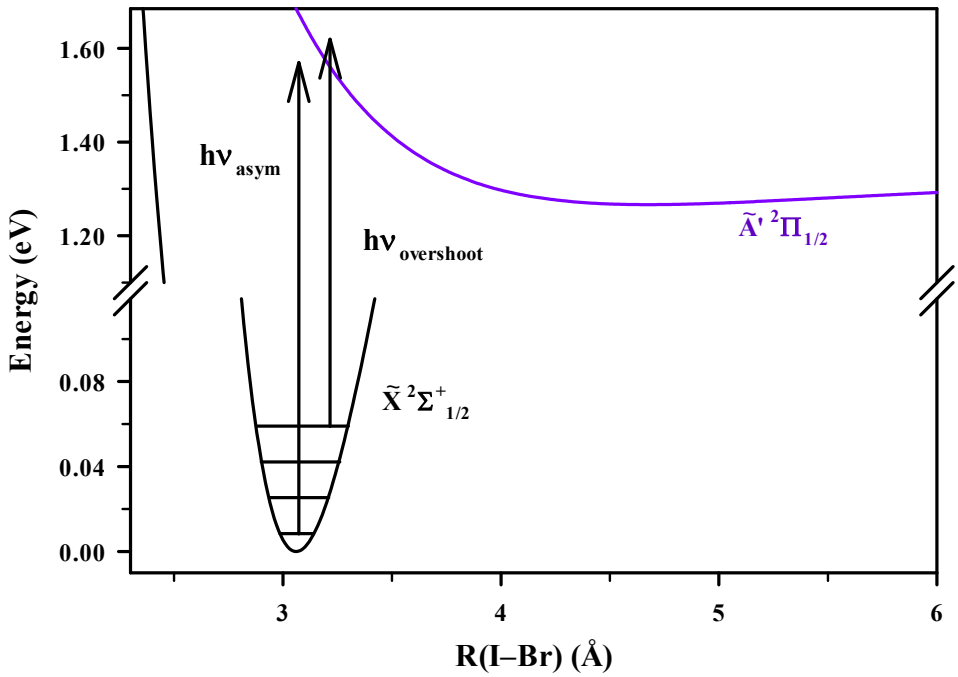

Figure 5.6 Schematic diagram illustrating the origin of the overshoot of the asymptote for the absorption recovery of $IBr^-(CO_2)_{13,14}$. The ground state potential is a Morse potential obtained using the experimentally determined parameters for the equilibrium bond length and vibrational frequency (Refs. 69, 131). The excited state potential is also a model Morse potential with the well depth chosen to match the experimentally determined value (Ref. 135) and the equilibrium bond length adjusted to illustrate the origin of the overshoot. The arrow labeled $h\nu_{overshoot}$ represents the transition giving rise to the overshoot of the asymptote, and the arrow labeled $h\nu_{asym}$ represents the transition giving rise to the asymptotic signal. Note the break in the energy scale along the y-axis.

5.4.2 Simulated Absorption Recovery Dynamics of $IBr^-(CO_2)_n$, n = 5–16

Long-time nonadiabatic MD simulations of $IBr^-(CO_2)_{5\text{-}16}$ were carried out to obtain simulated time constants for ground-state recombination. All simulations used a time step of 1 fs, while the length of simulations ranged from 20 ps for $IBr^-(CO_2)_5$ to 2 ns for $IBr^-(CO_2)_{8,10}$; ensemble sizes ranged from 100 trajectories for $IBr^-(CO_2)_{8,10}$ to over 1700 for $IBr^-(CO_2)_5$. A trajectory was considered to have "recombined" when the IBr^- bond length reached 3.3 Å on the ground state.

In most cases, it was possible to fit the time dependence of the recombination with a simple exponential (Eq. 5.1). An example of this fit is provided in Fig. 5.7 which plots both the theoretical and experimental results along with their respective single exponential fits. The exceptions were $IBr^-(CO_2)_{14}$, which required a bi-exponential fit, and $IBr^-(CO_2)_{5,6}$, for which a time delay of several ps elapsed before recombination began. In the latter case, the time dependence was fit to the expression:

$$N(t) = A_0[1 - e^{-\frac{t-t_0}{\tau}}] \qquad (5.2)$$

where the time delay t_0 is treated as an additional fit parameter. The simulated ground-state recombination times are summarized along with the experimental results in Fig. 5.8. Both experiment and simulation show an increase in ground-state recombination time of 2–3 orders of magnitude from $IBr^-(CO_2)_5$ to $IBr^-(CO_2)_{8–10}$.

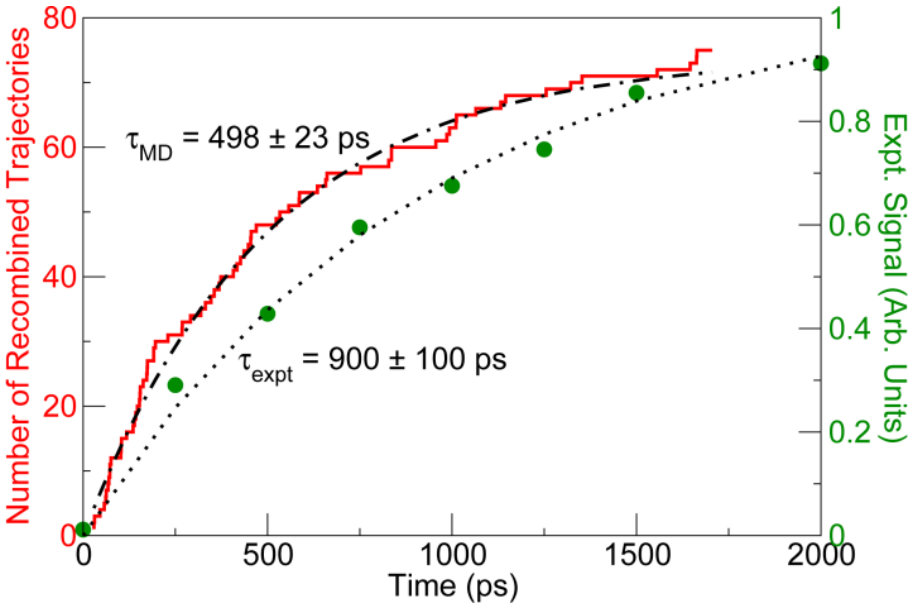

Figure 5.7 Ground-state recombination dynamics for $IBr^{-}(CO_2)_8$. The stepped line represents theoretical results, τ_{MD}, and the dots represent experimental data, τ_{expt}. The dotted and dash-dot-dash lines represent single-exponential fits to the experimental and simulated data, respectively, see Eq. (5.1).

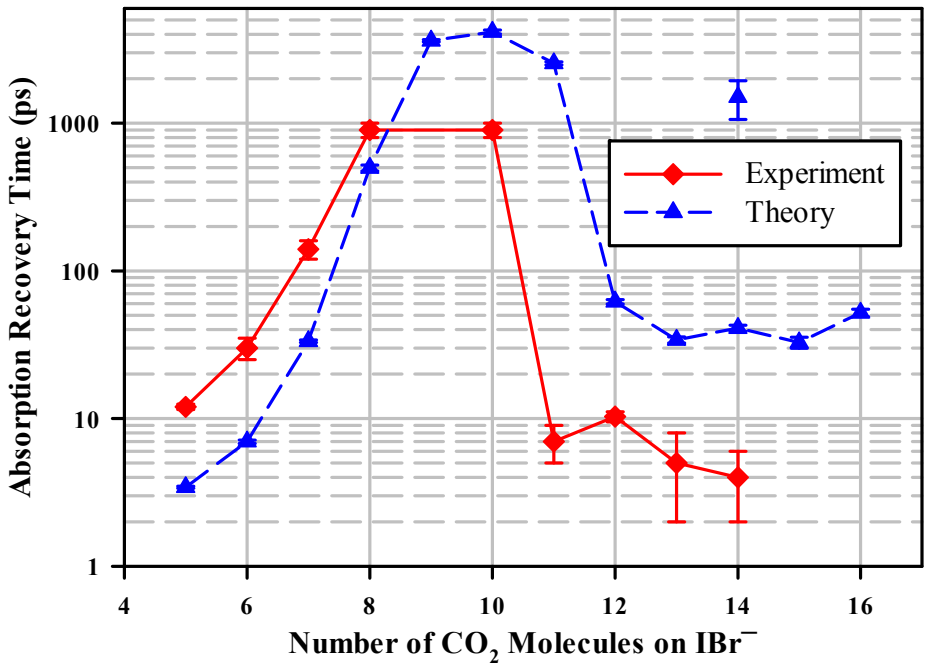

Figure 5.8 Comparison of experimental and theoretical ground-state recombination times. The red solid line and diamonds represent the experimental data, and the blue dashed line and triangles represent the results of the theoretical calculations. The lines connecting the data points correspond to the fast component of the absorption recovery in cases where the recovery was best fit to a bi-exponential function. The data points not connected by a line correspond to the slow component of the absorption recovery.

The extraordinarily long relaxation times observed in both simulation and experiment for n = 8–10 strongly suggest that in the solvated molecular ion, the potential energy surface corresponding to the Ã′ state contains a deep well. In order to elucidate the topography of this multidimensional surface, a technique used previously[121, 136] was adopted, in which trajectories are analyzed in terms of two coordinates, solute bond length and a collective solvent coordinate. In IBr^-, a negative $\Delta\Phi$ broadly represents a solvent configuration that is concentrated around the bromine atom, while a positive $\Delta\Phi$ corresponds to a configuration concentrated around iodine. A larger absolute value of $\Delta\Phi$ represents more solvent asymmetry, Fig. 5.9 (bottom), while a $\Delta\Phi$ near zero represents a more symmetric solvent configuration, Fig. 5.9 (top). Note that, in contrast

to a symmetric solute system like $I_2^-(CO_2)_n$, $\Delta\Phi = 0$ does not correspond exactly to a symmetric solvent configuration, as the two solute atoms are not the same. Also, many different solute-solvent configurations correspond to the same value of $\Delta\Phi$.

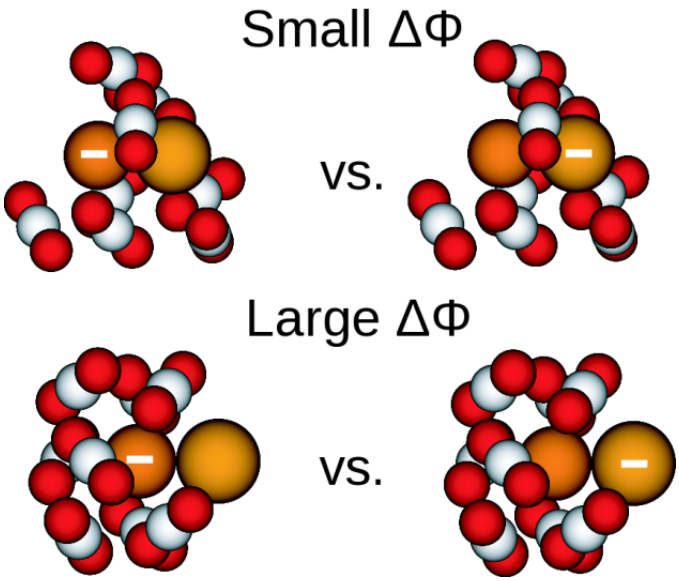

Figure 5.9 Visual representation of the solvent coordinate, $\Delta\Phi$, using $IBr^-(CO_2)_8$ clusters. $\Delta\Phi$ is defined by the change in energy when the charge is transferred from the bromine atom to the iodine atom as shown on the left and right sides of the figure, respectively. A symmetric solvent configuration, top, corresponds to a small $\Delta\Phi$. An asymmetric solvent configuration, bottom, corresponds to large values of $\Delta\Phi$.

While these plots allow analysis of the concerted motion of the solute and solvent over the length of the trajectory, the energy landscape has to be inferred from the limitations of this movement on the 2D surface. Wells and valleys of the energy landscape are indicated by batches of trajectories that are trapped either in small, compact areas (wells) or long, slim areas (valleys) on the 2D surface. Since a more extensive discussion of the physical significance of this

solvent-coordinate view of the recombination dynamics has appeared in the major publication[39] of this work, it will not be repeated here.

5.5 Discussion

The principal results of the experiments and simulations are presented in Figs. 5.4, 5.5, 5,7, 5.8, and 5.9, and may be summarized as follows:

(i) In these clusters, recombination is a highly efficient process, in the sense that given enough time, the probability of recombination is high. It occurs to a measureable degree in clusters having as few as two solvent molecules and reaches 100% for clusters having eight or more solvent molecules, significantly less than a closed solvent shell. This is very similar to the behavior seen for $I_2^-(CO_2)_n$ clusters.[37, 120]

(ii) While recombination is efficient, it is not necessarily fast, and the long time probability of recombination is not simply related to the rate. The timescale for recombination *increases* with increasing cluster size, up to $n = 10$, and then decreases as n increases further. This is drastically different from the behavior seen in I_2^- clusters.[37] In particular, the recombination times for $n = 8–10$ are orders of magnitude longer than those seen in the homonuclear system.

(iii) The solvent coordinate $\Delta\Phi$ plays a decisive role in recombination. The timescale for recombination is strongly correlated with the early-time distribution of $\Delta\Phi$, and trajectories that lead to recombination all follow similar pathways when plotted in $(r, \Delta\Phi)$ space.

The increase in recombination times for n = 5–10 appears to be roughly exponential with n, which strongly suggests that the recombination mechanism involves an activated process. Figure 5.9, in turn, elucidates the molecular origin of this process: recombination requires a collective motion of the solvent cage from the vicinity of the Br atom to that of the iodine atom. Collecting together the observations detailed in the preceding section, a coherent description of the excitation, dissociation and recombination process can be presented.

In clusters having 5 to 10 solvent molecules, absorption of a photon leads to an excited state in which the charge is predominantly localized on the Br atom (in contrast to the bare chromophore). The solvent molecules stabilize this charge distribution, more so since the I–Br bond is extended in this excited state. Increasing the number of solvent molecules increases the degree of stabilization, thereby lowering the free energy of the excited state "well." After a sufficiently long time, however, thermal fluctuations carry the solvent cage close to a symmetric geometry. The charge can then transfer to the iodine atom, and the solvent then reorganizes so as to stabilize this charge distribution. This solvent-driven adiabatic electron transfer event is the rate determining step in the recombination mechanism. The well in the excited state surface corresponding to solvated I^- is energetically close to a barrier in a lower lying excited state, however, so nonadiabatic transitions to this state and from it to the ground state are rapid. Once on the lower states, the chromophore can either dissociate (in small clusters) or recombine (in large clusters).

In clusters having more than ten solvent molecules, a further increase in n does not further stabilize the Br-localized configuration, since the additional solvent molecules add to the iodine side of the anionic chromophore. Indeed, one can expect that by stabilizing the I^-

localized configuration, the additional solvents may actually pull down the barrier to solvent reorganization. The free-energy barrier to solvent reorganization has both an energetic and an entropic component. In the largest clusters, both components are small, since a small amount of energy is required to move any given solvent molecule, and only a few solvent molecules need to be moved, in order for the solvent cage to reach a configuration at which nonadiabatic electronic quenching can occur.

Finally, to address the conundrum that opened this chapter: how does it come about that the ionic photoproduct distribution and the rate constant for recombination do not track one another? The answer is that the two processes are determined by dynamics on different potential surfaces. Except in the very smallest clusters ($n < 4$) there is essentially no dissociation on the initially excited surface. Instead, the simulations imply that the distribution between dissociation and recombination takes place on the $\tilde{A}$ and $\tilde{X}$ surfaces, following solvent reorganization and electronic quenching. As n increases from 5 to 10, the timescales for both dissociation and recombination increase because the solvated Br^- configuration becomes more stable. Once solvent reorganization and electronic quenching have occurred, however, the larger clusters can more effectively cage the fragments on the lower surface.

5.6 Conclusions

Experimental studies and nonadiabatic molecular dynamics simulations of the photodissociation and recombination of size-selected $IBr^-(CO_2)_n$ anionic clusters following excitation in the near-IR have been carried out. The simulations rely upon an effective Hamiltonian model that accounts, in a self-consistent fashion, for the interaction between the polarizable charge distribution on the anionic chromophore and the electrostatic forces due to the

solvent molecules. The surprising results of recent experimental studies[38] of this system – recombination times that increase with cluster size, resulting in timescales of the order of nanoseconds in clusters having 8–10 solvent molecules – are reproduced by the simulations, which furthermore predict that the timescale decreases again as the cluster size is increased further. New experimental results, presented in this chapter, confirm this latter prediction. A detailed analysis of the simulation trajectories leads to a comprehensive physical explanation for the experimental trends: recombination is found to be an activated process, with the rate-determining step being collective motion of the solvent cage from a configuration that stabilizes a charge localized on Br^- to one that favors I^-.

Chapter VI: UV Photofragmentation of $ICN^-(Ar)_n$ and Future Directions

6.1 Introduction

In order to elucidate further the electronic structure and photodissociation dynamics of ICN^- and solvated ICN^-, preliminary photofragmentation studies of mass-selected $ICN^-(Ar)_n$ were performed following ultraviolet (UV) excitation. Argon atoms were utilized as the solvent to prepare the ICN^- chromophore with minimal initial internal energy before photoexcitation. Additionally, only minor perturbations to the electronic structure of the ICN^- chromophore result from solvation with Ar atoms. Unlike previously studied dihalides,[33-35, 39] the $^2\Sigma^+$ excited state of the ICN^- chromophore is lower in energy than the $^2\Pi_{1/2}/^2\Pi_{3/2}$ excited states, where the mixed state designation $^2\Pi_{1/2}/^2\Pi_{3/2}$ is defined by McCoy.[66] Figure 6.1 shows the calculated potential energy curves of linear ICN^- as a function of the distance between the iodine atom and the center-of-mass of the CN diatom. The energy separation between the $^2\Pi_{1/2}$ and the $^2\Pi_{1/2}/^2\Pi_{3/2}$ excited states, corresponding to the excitation energy of the CN $\tilde{A}\ ^2\Pi \leftarrow \tilde{X}\ ^2\Sigma$ transition (1.146 eV),[71] is larger than the spin-orbit splitting energy of iodine (0.94 eV).[74] This leads to the $^2\Sigma^+$ excited state being stabilized in energy compared to the $^2\Pi_{1/2}/^2\Pi_{3/2}$ state. Therefore, the dissociation channel calculated[66] to be highest in energy corresponds to dissociation into I^- + CN ($\tilde{A}\ ^2\Pi$) and not I* ($^2P_{1/2}$) + CN^-, as with the dihalides.[33-35, 39] One of the results of the different ordering of the excited states is the nonadiabatic dynamics between the $^2\Pi_{1/2}$ and $^2\Sigma^+$ excited states with the appearance of an avoided crossing (dashed lines in Fig. 6.1). This avoided crossing is the result of a change in the charge distribution[66] on the chromophore on the $^2\Pi_{1/2}$ and $^2\Sigma^+$ excited state as a function of the distance between iodine and the center-of-mass of CN (see Chapter IV).

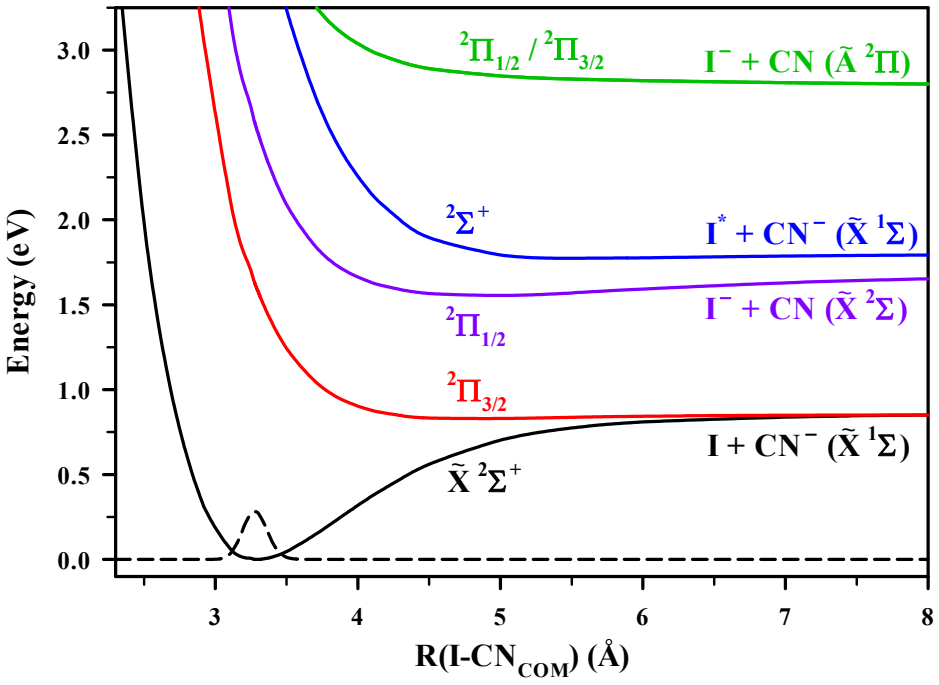

Figure 6.1 Linear ICN^- potential energy curves (based on Ref. 66) as a function of the distance between the iodine atom and the center-of-mass of the CN diatom. The ground state wavefunction is shown as a black dashed line. The diabatic curves proposed to take part in the dissociation dynamics of ICN^- are shown for the $^2\Pi_{1/2}$ (dashed purple line) and $^2\Sigma^+$ (dashed blue line) excited states.

One consequence of this crossing is that the ionic photoproduct distribution arising from 300 nm excitation of $ICN^-(Ar)_n$ should be different from the 500 nm distribution reported in Chapter III. In that case, 500 nm excitation[40] of $ICN^-(Ar)_n$, $1 \leq n \leq 5$, resulted in the major photoproducts being I^--based photoproducts (> 90 %). Recombined ICN^- constituted 5–10 % of the total, and CN^--based products are absent. Additionally, the I^--based and ICN^--based photoproducts are highly solvated. This last observation, coupled with calculations, shows that the excitation energy is not solely partitioned into solvent evaporation; instead, roughly 20% of the 1 eV excess energy is partitioned into CN rotation. Furthermore, recombined photoproducts are observed for n = 1–5. Due to the small Ar solvent binding energy, ~50 meV,[67] and the

flatness of the energy landscape around ICN^-, an Ar solvent atom can explore configurations different from its minimum energy configuration above the I–C bond. Specifically, an Ar solvent atom can sometimes be found near the CN end of the ICN^- chromophore. A collision between the departing CN diatom and the solvent Ar atom following photodissociation can convert a substantial amount of CN translational energy into CN rotational energy. This results in sufficient energy removed from CN translation to trap $I\cdots CN^-$ on the excited state surface, possibly for a sufficiently long time for a radiative transition from the $^2\Pi_{1/2}$ excited state to the $\tilde{X}\ ^2\Sigma^+$ state.[40] This radiative process is invoked because there is no other way to eliminate this much energy when a single solvent molecule is present.

Following photoexcitation of $ICN^-(Ar)_n$ with UV light, the dissociation dynamics could possibly involve the avoided crossing between the $^2\Sigma^+$ and $^2\Pi_{1/2}$ excited states. Excitation to and dissociation on the $^2\Sigma^+$ excited state without the contribution of nonadiabatic dynamics would result in observation of only CN^--based photoproducts. If the avoided crossing contributes to the dissociation dynamics, I^--based and ICN^--based photoproducts are expected to be observed as well. It is likely that observation of I^--based photoproducts is the result a nonadiabatic transition and dissociation on the $^2\Pi_{1/2}$, while the ICN^--based products are observed following a radiative transition from the $^2\Pi_{1/2}$ excited state to the $\tilde{X}\ ^2\Sigma^+$ state. While solvated I^--based photoproducts are observed following UV excitation of $ICN^-(Ar)_n$, the degree of solvation is not as extensive as that following 500 nm excitation. Furthermore, photoproducts as a result of one-atom caging are also not observed following UV excitation. However, a significant contribution of CN^- photoproducts is observed and illustrates multi-state dissociation dynamics of $ICN^-(Ar)_n$ following UV excitation.

6.2 Experimental

The photofragmentation studies of $ICN^-(Ar)_n$ are performed utilizing a tandem time-of-flight mass spectrometer (TOF MS) in conjunction with a nanosecond laser system. The sample of ICN is synthesized in the same manner described in Sec. 3.2 of Chapter III. Additionally, the TOF MS and experimental procedures are detailed in Chapter II; therefore, only information relevant to the generation of UV radiation will be presented here. The data presented here is the result of only five sets of data and is, therefore, only preliminary data; further photofragmentation studies following UV excitation of $ICN^-(Ar)_n$ are ongoing.

For the photofragmentation studies presented in this chapter, UV radiation is utilized. As detailed in Chapter II, the nanosecond laser (Coherent, model Infinity) is equipped with a commercial optical parametric oscillator (henceforth referred to as XPO), providing signal radiation between 420 and 680 nm. For the experiments presented in this chapter, a second harmonic generation stage (Coherent) positioned following the XPO, frequency doubles the signal radiation to generate UV light (260–340 nm). The light is collimated in a 2:1 telescope before entering the TOF MS. The energy content of a single pulse is ~260 μJ throughout this spectral range. The cross-sectional area of the laser beam is measured utilizing the knife-edge technique detailed in Chapter II.

6.3 Preliminary Results for UV Photoexcitation of $ICN^-(Ar)_n$

Preliminary studies of the photodissociation dynamics of $ICN^-(Ar)_n$ following 270 to 330 nm excitation have been performed in order to elucidate the role of multiple excited electronic state dynamics in the UV dissociation dynamics. Preliminary calculations performed

by McCoy[137] show the transition moments between the $\tilde{X}\ ^2\Sigma^+$ state and the $^2\Pi_{1/2}$, $^2\Sigma^+$ and $^2\Pi_{1/2}/^2\Pi_{3/2}$ excited states allow the possibility of both states playing a significant role in the dissociation dynamics. If a transition from the $\tilde{X}\ ^2\Sigma^+$ state to the $^2\Sigma^+$ occurs, the nonadiabatic crossing between the $^2\Sigma^+$ and $^2\Pi_{1/2}$ excited states discussed in Chapter IV likely plays a significant role in the dissociation dynamics.

6.3.1 Photodissociation Action Spectra

Preliminary measurements of the *relative* cross section for the production of ionic photoproducts following 270 to 330 nm excitation of ICN^- show a peak in the cross section near 300 nm. These results are determined in a similar manner to those obtained from visible photolysis. As described in Chapter II, the cross sections reported are *relative* cross sections because detection efficiencies of the photoproducts and parent ions as well as the spatial overlap of the ion-laser interaction are not measured.

Figure 6.2 shows the *relative* cross sections, $\sigma_{rel}(\lambda)$, for the production of I^- and CN^- photoproducts following 270 to 330 nm excitation of ICN^- with no solvent. Additionally, the *relative* cross sections for the production of I^- and CN^- following 430 to 650 nm excitation of the ICN^- chromophore are shown as a reference. All values in Fig. 6.2 are normalized to the *relative* cross section for the production of I^- at 300 nm. The error limits are the average percent error for each photoproduct after five data sets; their values are defined in the caption for Fig. 6.2. The full-width-at-half-maximum (FWHM) of $\sigma_{rel}(\lambda)$ for the production of I^- products from 270–330 nm is ~50 nm, compared to ~60 nm from 430–650 nm. The increased *relative* cross section for the production of I^- products following UV excitation indicates a stronger transition is being probed than that observed following 430–650 nm excitation. A sudden increase in the

cross section of CN^- at 280 nm is shown in Fig. 6.2; however, experiments presently being performed show a contribution from the CN^- photoproduct following 270 nm excitation and suggest that this sudden onset is not as drastic as indicated in Fig. 6.2.[138]

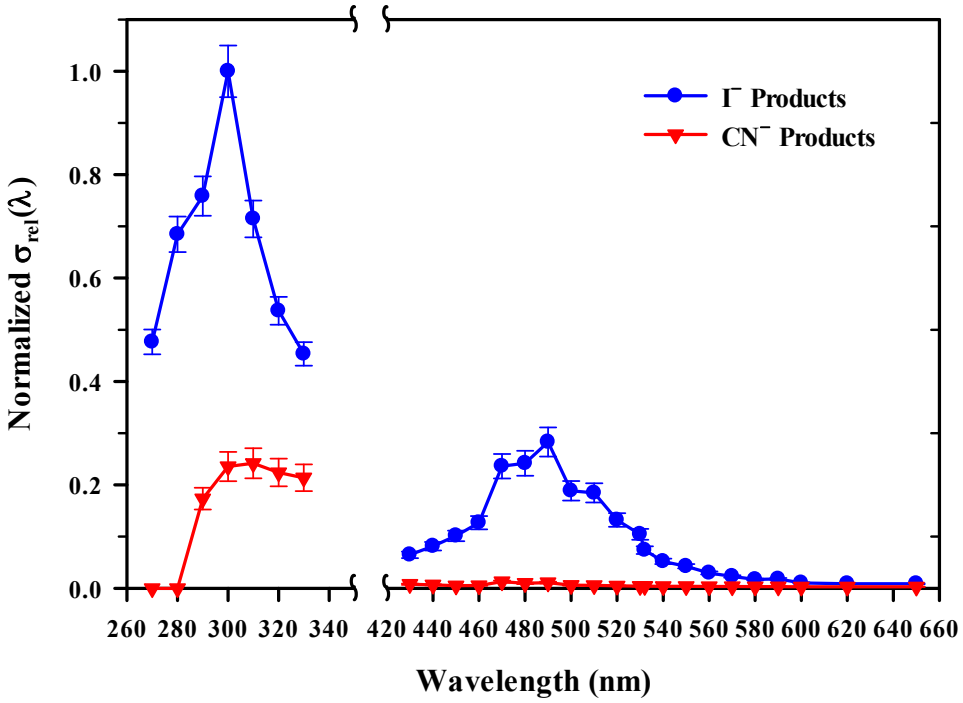

Figure 6.2 Normalized *relative* cross section ($\sigma_{rel}(\lambda)$) for the production of I^- and CN^- following 270 to 330 nm excitation of the ICN^- chromophore. The normalized relative cross section for the production of I^- and CN^- following 430 to 650 nm excitation of ICN^- is shown for reference. All values are normalized to $\sigma_{rel}(\lambda)$ for the production of I^- products at 300 nm. The error limits are the average percent error for each photoproduct and are defined as follows: 15% for CN^- and 10% for I^- following 430–650 nm excitation, and 12% and 5% for CN^- and I^- following 270–330 nm excitation, respectively. Note the break in the x-axis.

The dominance of I^- photoproducts following 270–330 nm excitation of the ICN^- chromophore suggests that photoexcitation is either accessing the $^2\Pi_{1/2}/^2\Pi_{3/2}$ or the $^2\Sigma^+$ excited states. If excitation to the $^2\Sigma^+$ excited state occurs, I^- photoproducts are produced following a nonadiabatic transition to the $^2\Pi_{1/2}$ state asymptote. Preliminary calculations by McCoy[137] show

that the $^2\Sigma^+$ and the $^2\Pi_{1/2}/^2\Pi_{3/2}$ states lie close in energy at the ground state equilibrium geometry of ICN^- following 300 nm excitation. Additionally, similar to IBr^-,[102] the $^2\Sigma^+ \leftarrow \tilde{X}\ ^2\Sigma^+$ transition has the largest transition moment, followed by the $^2\Pi_{1/2} \leftarrow \tilde{X}\ ^2\Sigma^+$ transition, with the smallest of the three moments being the $^2\Pi_{1/2}/^2\Pi_{3/2} \leftarrow \tilde{X}\ ^2\Sigma^+$ transition. Thus, the I^- products are proposed to result from excitation of the ICN^- chromophore to the $^2\Sigma^+$ excited state and a subsequent nonadiabatic transition. Due to the possible contribution of nonadiabatic dynamics, the CN^- photoproducts observed following 270 to 330 nm excitation of the ICN^- chromophore are likely produced following a nonadiabatic transition to the $^2\Pi_{1/2}$ state and dissociation on the adiabatic $^2\Sigma^+$ excited state asymptote. This results in a cross section for the production of CN^- photoproducts that is roughly a factor 40 times larger than the cross section following 430 to 650 nm excitation of the ICN^- chromophore, for which only a minor yield of CN^- products are observed (e.g. ~3% following 500 nm excitation).

6.3.2 Photofragmentation Data at 300 nm

The ionic photoproduct distribution for the photofragmentation of $ICN^-(Ar)_n$ following 300 nm excitation is shown in Fig. 6.3. Additionally, Table 6.1 tabulates the yield of each ionic photoproduct observed following 300 nm excitation of $ICN^-(Ar)_n$; the bold red values in Table 6.1 give the percentage of each dissociation channel (i.e. I^--based, CN^--based, or ICN^--based) and are plotted in Fig. 6.3. Laser power dependence studies were performed to confirm that all ionic photoproducts were the result of one-photon photodissociation of $ICN^-(Ar)_n$.

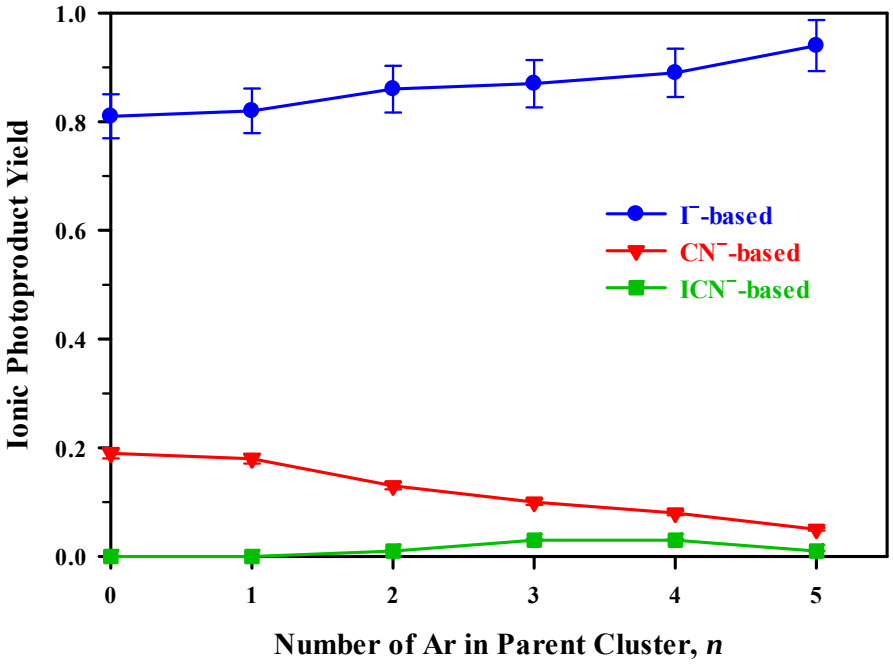

Figure 6.3 Ionic photoproduct distribution of $ICN^-(Ar)_n$ following one-photon 300 nm excitation. The data points are the bold red values in Table 6.1. The error bars correspond to a 5% standard deviation and are plotted for each ionic product distribution.

Table 6.1 One-photon ionic photoproducts following 300 nm excitation of $ICN^-(Ar)_n$.

Parent Cluster	CN^--Based	I^--Based	ICN^--Based
ICN^-	CN^- = 19% **19%**	I^- = 81% **81%**	**0%**
$ICN^-(Ar)$	CN^- = 18% **18%**	I^- = 41% $I^-(Ar)$ = 41% **82%**	**0%**
$ICN^-(Ar)_2$	CN^- = 13% **13%**	I^- = 32% $I^-(Ar)$ = 54% **86%**	ICN^- = 1% **1%**
$ICN^-(Ar)_3$	CN^- = 10% **10%**	I^- = 20% $I^-(Ar)$ = 39% $I^-(Ar)_2$ = 28% **87%**	ICN^- = 3% **3%**
$ICN^-(Ar)_4$	CN^- = 8% **8%**	I^- = 15% $I^-(Ar)$ = 37% $I^-(Ar)_2$ = 37% **89%**	ICN^- = 3% **3%**
$ICN^-(Ar)_5$	CN^- = 5% **5%**	I^- = 9% $I^-(Ar)$ = 22% $I^-(Ar)_2$ = 42% $I^-(Ar)_3$ = 17% $I^-(Ar)_4$ = 4% **94%**	ICN^- = 1% **1%**

Following 300 nm excitation of ICN^-, roughly 81% of the ionic photoproducts observed are I^-. For I^- photoproducts to be observed, the chromophore must dissociate on either the $^2\Pi_{1/2}/^2\Pi_{3/2}$ excited state or on the $^2\Pi_{1/2}$ state following a nonadiabatic transition from the $^2\Sigma^+$ excited state. As stated in Sec. 6.3.1, preliminary calculations[137] show that the transition from the $\tilde{X}\ ^2\Sigma^+$ state to the $^2\Sigma^+$ excited state has the largest transition moment, and it is therefore likely that

ICN^- is predominantly excited to the $^2\Sigma^+$ state, after which the dissociating chromophore undergoes a nonadiabatic transition to the $^2\Pi_{1/2}$ state, resulting in I^- products. Within the limits of a one-dimensional Landau-Zener approximation[139-141] of the transition probability between two states in an avoided crossing, the high amount of kinetic energy supplied to ICN^- following 300 nm excitation (roughly 2.36 eV at the $^2\Sigma^+$ excited state asymptote) favors a nonadiabatic transition from the $^2\Sigma^+$ state to the $^2\Pi_{1/2}$ state and, thus, dissociation into I^- + CN ($\tilde{X}\ ^2\Sigma$). Though the hopping probability is greater due to the large kinetic energy, the observation of CN^- products following UV excitation implies that a small portion (~19%) of the ionic photoproducts are possibly a result of adiabatic dissociation on the $^2\Sigma^+$ excited state into I* ($^2P_{1/2}$) and CN^-. This result is in agreement with the proposal that more than one excited state contributes to the dissociation dynamics of the ICN^- chromophore following UV excitation. Additionally, a minor contribution from dissociation on the $^2\Pi_{1/2}/^2\Pi_{3/2}$ excited state may occur, but the present experimental setup cannot confirm this proposal and theoretical work is in the preliminary stages.

Upon addition of Ar solvent atoms, the ionic photoproduct distribution is altered in favor of a larger yield of I^- photoproducts, a smaller yield of CN^- products, and a minor contribution from **recombined** products. With the addition of one Ar solvent atom, the only observed ionic photoproducts following UV excitation of $ICN^-(Ar)$ are I^--based and CN^-; recombined ICN^- is not detected. Following the addition of a second Ar solvent, interestingly, recombined ICN^- is observed. Qualitatively similar to the results of 500 nm excitation of $ICN^-(Ar)_n$ (see Chapter III), the yield of recombined products remains at roughly 3% for all values of *n* studied, but now with the excitation energy increased from 2.5 to 4 eV. Production of recombined products following 300 nm excitation might occur *via* a mechanism similar to that proposed for 500 nm excitation,

with the exceptions that a nonadiabatic transition from the $^2\Sigma^+$ state to the $^2\Pi_{1/2}$ state must occur first and there is much more excess energy that must be taken away by either radiation or the two departing Ar atoms. It might be that, following 300 nm excitation to the $^2\Sigma^+$ excited state, the dissociating chromophore undergoes a nonadiabatic transition to the $^2\Pi_{1/2}$ state and becomes trapped in a relatively shallow (~270 meV) well. The trapping time would have to be sufficiently long to allow a radiative transition to the ground state. In contrast to 500 nm excitation, the recombined photoproducts observed following 300 nm excitation are predominantly ICN^-, with a small contribution from $ICN^-(Ar)$. However, even a single Ar atom remaining attached to the recombined ICN^- is astonishing.

As the number, *n*, of Ar solvent atoms is increased, the yield of I^--based products steadily increases from roughly 82% of the ionic photoproducts for $n = 1$ to roughly 94% for $n = 5$. Following 300 nm excitation of $ICN^-(Ar)_n$, all CN^- photoproducts observed are unsolvated, whereas the I^--based products are highly solvated. For example, following 300 nm excitation of $ICN^-(Ar)_2$, I^- (~32%) and $I^-(Ar)$ (~54%) are observed but only unsolvated CN^- is observed (13%). This is qualitatively similar to 500 nm excitation of $ICN^-(Ar)_n$, in which highly solvated I^--based products were observed, but the dominant photoproduct was often the highest solvated (largest number of Ar solvent) products. These observations are tantalizing, but do not point to the underlying mechanism; thus, more work is needed.

More recent photofragmentation studies[138] of $ICN^-(Ar)_n$ following UV excitation in which more sets of data have been measured observe additional weak photoproducts not shown in these preliminary results. Although the ionic photoproduct distributions and the cross section for the production of CN^- following 270 and 280 nm excitation are slightly different, the qualitative results are the same for these preliminary results and the current experiments.

6.4 Summary of Preliminary Results

Photofragmentation of $ICN^-(Ar)_n$ (n = 0–5) following UV excitation results in dynamics that are possibly affected by an avoided crossing between the $^2\Sigma^+$ and $^2\Pi_{1/2}$ excited states. The *relative* cross section for the production of I^- and CN^- following 270 to 330 nm excitation of the ICN^- chromophore reveal the dominance of I^- photoproducts, but also show the presence of CN^- products. The I^--based and unsolvated CN^- photoproducts following UV excitation of $ICN^-(Ar)_n$ suggest multiple excited state are accessed, but are the result of an undetermined mechanism. Additionally, only a small contribution (~3%) from recombined products is observed for n = 2–5.

6.5 Future Directions

Future studies of the photodissociation dynamics of solvated ICN^- will focus on the energy flow within the chromophore and the effect of different solvents on the dynamics. Photofragmentation studies following 400, 500, and 600 nm excitation of $ICN^-(Ar)_n$ ($n > 5$) clusters would complete the comparison between the short-range ion-induced dipole interaction between ICN^- and Ar versus the long-range ion-quadrupole interaction of ICN^- with CO_2. Additionally, analysis of the average number of Ar solvent atoms lost following photoexcitation of $ICN^-(Ar)_n$ in the large cluster limit would elucidate the location of solvation as n is increased and provide another experimental measurement of the solvent binding energy of Ar to the ICN^- chromophore. Photofragmentation studies of the ICN^- chromophore solvated by molecules with strong permanent dipole moments would further develop the understanding of dynamics induced by long-range interactions. Solvents such as water, ammonia, and carbonyl sulfide, could be utilized to provide a range of strength of the solvent's dipole moment. Increased solute-solvent and solvent-solvent interactions, as a result of solvent dipole moments, may result in an

increased yield of recombined ICN^- photoproducts. Furthermore, theoretical studies simulating the photodissociation dynamics of the ICN^- chromophore on the $^2\Sigma^+$ excited state, involving the nonadiabatic avoided crossing, and including solvation of ICN^- would help elucidate the details of the photodissociation dynamics.

Time-resolved studies of solvated ICN^- would also provide insight into the dissociation dynamics of this triatomic pseudo-dihalide. Performing time-resolved photoelectron spectroscopy studies could potentially provide experimental evidence for the involvement of the avoided crossing and monitor the appearance time of various photoproducts following photodissociation of $ICN^-(CO_2)_n$. However, because of the small Ar solvent binding energy to ICN^- (~50 meV),[67] identification of the spectral features corresponding to each photoproduct following photodissociation and photodetachment of $ICN^-(Ar)_n$ is unfeasible. Time-resolved absorption recovery experiments on $ICN^-(CO_2)_n$ would elucidate the presence or absence of the $NCCO_2^-$ molecule or solvent-separated-like complexes following photoexcitation of larger clusters and potentially measure the timescale of recombination of the dissociating chromophore. Unfortunately, because the yield of recombined one-photon photoproducts never exceeds roughly 50% (for all wavelengths studied), the signal intensity of two-photon photoproducts is exceedingly small, making time-resolved experiments difficult. Furthermore, because the effects of differential solvation in $ICN^-(CO_2)_n$ are proposed to be similar to those observed for $ICl^-(CO_2)_n$,[77] the time scale for absorption recovery of $ICN^-(CO_2)_n$ is expected to surpass that of $IBr^-(CO_2)_n$, possibly overreaching the limit of the present experimental apparatus.

Photodissociation studies of other triatomic solutes within molecular clusters would provide further understanding of the importance of the internal degrees-of-freedom in the

dissociation dynamics. Experimental studies of the photofragmentation of $BrCN^-(Ar)_n$ and $ClCN^-(Ar)_n$ would elucidate the role of the CN rotation following photoexcitation. As the mass match between the halogen and the CN diatom becomes closer, the translational and rotational energy partitioned into the CN fragment following photodissociation decreases. Therefore, solvent evaporation may play an increased role in the dissociation dynamics as the mass of the solute is decreased from ICN^- to $BrCN^-$ to $ClCN^-$.

Bibliography

[1] J. Franck and E. Rabinowitch, "Some remarks about free radicals and the photochemistry of solutions," *Trans. Faraday Soc.* **30**, 120 (1934).

[2] E. Rabinowitch and W. C. Wood, "The collison mechanism and the primary photochemical process in solutions," *Trans. Faraday Soc.* **32**, 1381 (1936).

[3] E. Rabinowitch and W. C. Wood, "Properties of Illuminated Iodine Solutions. I. Photochemical Dissocistion of Iodine Molecules in Solution," *Trans. Faraday Soc.* **32**, 547 (1936).

[4] A. L. Harris, J. K. Brown, and C. B. Harris, "The Nature of Simple Photodissociation Reactions in Liquids on Ultrafast Time Scales," *Annu. Rev. Phys. Chem.* **39**, 341 (1988).

[5] D. A. V. Kliner, J. C. Alfano, and P. F. Barbara, "Photodissociation and vibrational relaxation of I_2^- in ethanol," *J. Chem. Phys.* **98**, 5375 (1993).

[6] L. F. Meadows and R. M. Noyes, "The Dependence on Wave Length of Quantum Yields for Iodine Dissociation," *J. Am. Chem. Soc.* **82**, 1872 (1960).

[7] D. J. Nesbitt and J. T. Hynes, "Slow vibrational relaxation in picosecond iodine recombination in liquids," *J. Chem. Phys.* **77**, 2130 (1982).

[8] J. Troe, "Atom and Radical Recombination Reactions," *Annu. Rev. Phys. Chem.* **29**, 223 (1978).

[9] P. K. Walhout, J. C. Alfano, K. A. M. Thakur, and P. F. Barbara, "Ultrafast Experiments on the Photodissociation, Recombination, and Vibrational Relaxation of I_2^-: Role of Solvent-Induced Solute Charge Flow," *J. Phys. Chem.* **99**, 7568 (1995).

[10] M. Wulff, S. Bratos, A. Plech, R. Vuilleumier, F. Mirloup, M. Lorenc, Q. Kong, and H. Ihee, "Recombination of photodissociated iodine: A time-resolved x-ray-diffraction study," *J. Chem. Phys.* **124**, 034501 (2006).

[11] J. M. Farrar, "Size-dependent reactivity in open shell metal-ion polar solvent clusters: spectroscopic probes of electronic-vibration coupling, oxidation and ionization," *Int. Rev. Phys. Chem.* **22**, 593 (2003).

[12] R. B. Gerber, A. B. McCoy, and A. Garcia-Vela, "Photochemical Reactions in Weakly Bound Clusters," *Annu. Rev. Phys. Chem.* **45**, 275 (1994).

[13] G. R. Fleming and M. Cho, "Chromophore-solvent Dynamics," *Annu. Rev. Phys. Chem.* **47**, 109 (1996).

[14] J. R. R. Verlet, "Femtosecond spectroscopy of cluster anions: insights into condensed-phase phenomena from the gas-phase," *Chem. Soc. Rev.* **37**, 505 (2008).

[15] V. E. Bondybey and M. K. Beyer, "How many molecules make a solution?," *Int. Rev. Phys. Chem.* **21**, 277 (2002).

[16] E. T. Branigan, N. Halberstadt, and V. A. Apkarian, "Solvation dynamics through Raman spectroscopy: Hydration of Br_2 and Br_3^-, and solvation of Br_2 in liquid bromine," *J. Chem. Phys.* **134**, 174503 (2011).

[17] B. L. Grigorenko, A. V. Nemukhin, and V. A. Apkarian, "Many-body potentials and dynamics based on diatomics-in-molecules: Vibrational frequency shifts in Ar_nHF (n = 1–12,62) clusters," *J. Chem. Phys.* **104**, 5510 (1996).

[18] M. E. Jacox, "The vibrational energy levels of small transient molecules isolated in neon and argon matrices," *Chem. Phys.* **189**, 149 (1994).

[19] O. Cheshnovsky and S. Leutwyler, "Proton transfer in neutral gas-phase clusters: α-Naphthol·$(NH_3)_n$," *J. Chem. Phys.* **88**, 4127 (1988).

[20] T. Droz, R. Knochenmuss, and S. Leutwyler, "Excited-state proton transfer in gas-phase clusters: 2-Naphthol·$(NH_3)_n$," *J. Chem. Phys.* **93**, 4520 (1990).

[21] O. David, C. Dedonder-Lardeux, and C. Jouvet, "Is there an Excited State Proton Transfer in phenol (or 1-naphthol)-ammonia clusters? Hydrogen Detachment and Transfer to Solvent: A key for non-radiative processes in clusters," *Int. Rev. Phys. Chem.* **21**, 499 (2002).

[22] S. Goyal, D. L. Schutt, and G. Scoles, "Molecular solvation in atomic clusters studied by means of molecular beam infrared spectroscopy," *Acc. Chem. Res.* **26**, 123 (1993).

[23] X. J. Gu, D. J. Levandier, B. Zhang, G. Scoles, and D. Zhuang, "On the infrared spectroscopy of SiF_4 and SF_6 in Ar clusters: Location of the solute," *J. Chem. Phys.* **93**, 4898 (1990).

[24] A. McIlroy, R. Lascola, C. M. Lovejoy, and D. J. Nesbitt, "Structural dependence of hydrogen fluoride vibrational red shifts in Ar_nHF, n = 1–4, via high-resolution slit jet infrared spectroscopy," *J. Phys. Chem.* **95**, 2636 (1991).

[25] M. A. Johnson and W. C. Lineberger, "Pulsed Methods for Cluster Ion Spectroscopy," in *Techniques for the Study of Ion Molecule Reactions*, edited by J. M. Farrar, and J. W. Saunders (Wiley, New York, 1988), pp. 591.

[26] P. R. Kemper and M. T. Bowers, "Pulsed Methods for Cluster Ion Spectroscopy," in *Techniques for the Study of Ion Molecule Reactions*, edited by J. M. Farrar, and J. W. Saunders (Wiley, New York, 1988), p. 1.

[27] A. W. Castleman and R. G. Keesee, "Gas-Phase Clusters: Spanning the States of Matter," *Science* **241**, 36 (1988).

[28] A. W. Castleman and S. Wei, "Cluster Reactions," *Annu. Rev. Phys. Chem.* **45**, 685 (1994).

[29] R. G. Keesee and A. W. Castleman Jr., "Thermochemical Data on Gas-Phase Ion-Molecule Association and Clustering Reactions," *J. Phys. Chem. Ref. Data* **15**, 1011 (1986).

[30] R. G. Keesee, N. Lee, and A. W. Castleman Jr., "Properties of clusters in the gas phase: V. Complexes of neutral molecules onto negative ions," *J. Chem. Phys.* **73**, 2195 (1980).

[31] C. G. Elles and F. F. Crim, "Connecting Chemical Dynamics in Gases and Liquids," *Annu. Rev. Phys. Chem.* **57**, 273 (2006).

[32] M. L. Alexander, N. E. Levinger, M. A. Johnson, D. Ray, and W. C. Lineberger, "Recombination of Br_2^- photodissociated within mass selected ionic clusters," *J. Chem. Phys.* **88**, 6200 (1988).

[33] M. E. Nadal, P. D. Kleiber, and W. C. Lineberger, "Photofragmentation of mass-selected $ICl^-(CO_2)_n$ cluster ions: Solvation effects on the structure and dynamics of the ionic chromophore," *J. Chem. Phys.* **105**, 504 (1996).

[34] J. M. Papanikolas, J. R. Gord, N. E. Levinger, D. Ray, V. Vorsa, and W. C. Lineberger, "Photodissociation and geminate recombination dynamics of I_2^- in mass-selected $I_2^-(CO_2)_n$ cluster ions," *J. Phys. Chem.* **95**, 8028 (1991).

[35] T. Sanford, S.-Y. Han, M. A. Thompson, R. Parson, and W. C. Lineberger, "Photodissociation dynamics of $IBr^-(CO_2)_n$, $n < 15$," *J. Chem. Phys.* **122**, 054307 (2005).

[36] V. Vorsa, P. J. Campagnola, S. Nandi, M. Larsson, and W. C. Lineberger, "Photofragmentation of $I_2^-(Ar)_n$ Clusters: Observation of Metastable Isomeric Ionic Fragments," *J. Chem. Phys.* **105**, 2298 (1996).

[37] J. M. Papanikolas, V. Vorsa, M. E. Nadal, P. J. Campagnola, H. K. Buchenau, and W. C. Lineberger, "I_2^- photodissociation and recombination dynamics in size-selected $I_2^-(CO_2)_n$ cluster ions," *J. Chem. Phys.* **99**, 8733 (1993).

[38] V. Dribinski, J. Barbera, J. P. Martin, A. Svendsen, M. A. Thompson, R. Parson, and W. C. Lineberger, "Time-resolved study of solvent-induced recombination in photodissociated $IBr^-(CO_2)_n$ clusters," *J. Chem. Phys.* **125**, 133405 (2006).

[39] M. A. Thompson, J. P. Martin, J. P. Darr, W. C. Lineberger, and R. Parson, "A combined experimental/theoretical investigation of the near-infrared photodissociation of $IBr^-(CO_2)_n$," *J. Chem. Phys.* **129**, 224304 (2008).

[40] A. S. Case, E. M. Miller, J. P. Martin, Y.-j. Lu, L. Sheps, A. B. McCoy, and W. C. Lineberger, "Dynamic Mapping of CN Rotation Following Photoexcitation of ICN^-," *Angew. Chem., Int. Ed.* **124**, 2705 (2011).

[41] W. C. Wiley and I. H. McLaren, "Time-of-Flight Mass Spectrometer with Improved Resolution," *Rev. Sci. Instrum.* **26**, 1150 (1955).

[42] B. Bak and A. Hillebert, "Cyanogen Iodide," *Org. Synth.* **4**, 207 (1963).

[43] J. A. A. Ketelaar and S. Kruyer, "Der Dampfdruck des Jodcyans," *Recl. Trav. Chim. Pays-Bas* **62**, 550 (1943).

[44] Y. B. Konev, N. I. Lipatov, P. P. Pashinin, and A. M. Prokhorov, "Molecular infrared laser with $Br^* \rightarrow CO_2$ electronic-vibrational energy transfer as the pump mechanism," *Sov. J. Quantum Electron.* **9**, 1167 (1979).

[45] B. D. Rafferty, B. T. Anderson, J. Glassman, H. C. Miller, A. I. Lampson, and G. D. Hager, "Experimental and theoretical investigation of a coaxial pumped photolytic atomic bromine laser," *IEEE J. Quantum Electron.* **33**, 685 (1997).

[46] E. Wrede, S. Laubach, S. Schulenburg, A. Brown, E. R. Wouters, A. J. Orr-Ewing, and M. N. R. Ashfold, "Continuum state spectroscopy: A high resolution ion imaging study of IBr photolysis in the wavelength range 440–685 nm," *J. Chem. Phys.* **114**, 2629 (2001).

[47] M. A. Johnson and W. C. Lineberger, "Spectroscopy of Ionic Clusters," in *Molecular and Cluster Beam Science* (National Research Council, Washington, DC, 1987).

[48] B. R. Eichelberger, T. P. Snow, and V. M. Bierbaum, "Collision Rate Constants for Polarizable Ions," *J. Am. Soc. Mass Spectrom.* **14**, 501 (2003).

[49] R. E. Continetti, D. R. Cyr, and D. M. Neumark, "Fast 8 kV metal-oxide semiconductor field-effect transistor switch," *Rev. Sci. Instrum.* **63**, 1840 (1992).

[50] B. A. Mamyrin, V. I. Karataev, D. V. Shmikk, and V. A. Zagulin, "The mass-reflectron, a new nonmagnetic time-of-flight mass spectrometer with high resolution," *Sov. Phys. JETP* **37**, 45 (1973).

[51] T. Sanford, "Photodissociation Dynamics and Photoelectron Imaging Spectroscopy of Anions and Anion Clusters," Ph.D. thesis, University of Colorado, 2004.

[52] J. M. Khosrofian and B. A. Garetz, "Measurement of a Gaussian laser beam diameter through the direct inversion of knife-edge data," *Appl. Opt.* **22**, 3406 (1983).

[53] D. W. Boo, Y. Ozaki, L. H. Andersen, and W. C. Lineberger, "Femtosecond Dynamics of Linear Ag_3^-," *J. Phys. Chem. A* **101**, 6688 (1997).

[54] J. Barbera, "Combining Research in Physical Chemistry and Chemical Education," Ph.D. thesis, University of Colorado, 2007.

[55] J. F. Black, J. R. Waldeck, and R. N. Zare, "Evidence for three interacting potential energy surfaces in the photodissociation of ICN at 249 nm," *J. Chem. Phys.* **92**, 3519 (1990).

[56] G. Hancock, G. Richmond, G. A. D. Ritchie, S. Taylor, M. L. Costen, and G. E. Hall, "Frequency modulated circular dichroism spectroscopy: application to ICN photolysis," *Mol. Phys.* **108**, 1083 (2010).

[57] J. Helbing, M. Chergui, S. Fernandez-Alberti, J. Echave, N. Halberstadt, and J. A. Beswick, "Caging and excited state emission of ICN trapped in cryogenic matrices: experiment and theory," *Phys. Chem. Chem. Phys.* **2**, 4131 (2000).

[58] W. P. Hess and S. R. Leone, "Absolute I* quantum yields for the ICN Ã state by diode laser gain-vs-absorption spectroscopy," *J. Chem. Phys.* **86**, 3773 (1987).

[59] A. I. Krylov and R. B. Gerber, "Photodissociation of ICN in solid and in liquid Ar: Dynamics of the cage effect and of excited-state isomerization," *J. Chem. Phys.* **100**, 4242 (1994).

[60] A. C. Moskun and S. E. Bradforth, "Photodissociation of ICN in polar solvents: Evidence for long lived rotational excitation in room temperature liquids," *J. Chem. Phys.* **119**, 4500 (2003).

[61] A. C. Moskun, A. E. Jailaubekov, S. E. Bradforth, G. Tao, and R. M. Stratt, "Rotational Coherence and a Sudden Breakdown in Linear Response Seen in Room-Temperature Liquids," *Science* **311**, 1907 (2006).

[62] I. Nadler, D. Mahgerefteh, H. Reisler, and C. Wittig, "The 266 nm photolysis of ICN: Recoil velocity anisotropies and nascent E,V,R,T excitations for the CN + I($^2P_{3/2}$) and CN + I($^2P_{1/2}$) channels," *J. Chem. Phys.* **82**, 3885 (1985).

[63] C. A. Rivera, N. Winter, R. V. Harper, I. Benjamin, and S. E. Bradforth, "The dynamical role of solvent on the ICN photodissociation reaction: connecting experimental observables directly with molecular dynamics simulations," *Phys. Chem. Chem. Phys.* **13**, 8269 (2011).

[64] Y. Amatatsu, S. Yabushita, and K. Morokuma, "*Ab initio* potential energy surfaces and trajectory studies of A-band photodissociation dynamics: ICN* → I + CN and I* + CN," *J. Chem. Phys.* **100**, 4894 (1994).

[65] J. Qian, D. J. Tannor, Y. Amatatsu, and K. Morokuma, "*Ab initio* structure and wave packet dynamics of ICN photodissociation," *J. Chem. Phys.* **101**, 9597 (1994).

[66] A. B. McCoy, "Potential Energy Surfaces and Porperties of ICN^- and ICN," *Int. J. Quantum Chem.*, DOI: 10.1002/qua.24011 (2012).

[67] E. M. Miller, L. Sheps, Y.-j. Lu, A. S. Case, A. B. McCoy, and W. C. Lineberger, "New View of ICN A continuum using Photoelectron Spectroscopy of ICN^-," *J. Chem. Phys.* **136**, 044313 (2011).

[68] F. Muntean, M. S. Taylor, A. B. McCoy, and W. C. Lineberger, "Femtosecond study of $Cu(H_2O)$ dynamics," *J. Chem. Phys.* **121**, 5676 (2004).

[69] L. Sheps, E. M. Miller, and W. C. Lineberger, "Photoelectron spectroscopy of small $IBr^-(CO_2)_n$, n = 0–3 cluster anions," *J. Chem. Phys.* **131**, 064304 (2009).

[70] C. E. Klots, "The Evaporative Ensemble," *Z. Phys. D Atom. Mol. Cl.* **5**, 83 (1987).

[71] K. P. Huber and G. Herzberg, *Molecular Spectra and Molecular Structure. IV. Constants of Diatomic Molecules*, (Van Nostrand Reinhold Co., 1979).

[72] A. J. Kotlar, R. W. Field, J. I. Steinfeld, and J. A. Coxon, "Analysis of perturbations in the $A\ ^2\Pi$–$X\ ^2\Sigma^+$ "Red" system of CN," *J. Mol. Spectrosc.* **80**, 86 (1980).

[73] S. E. Bradforth, E. H. Kim, D. W. Arnold, and D. M. Neumark, "Photoelectron spectroscopy of CN^-, NCO^-, and NCS^-," *J. Chem. Phys.* **98**, 800 (1993).

[74] C. E. Moore, *Atomic Energy Levels*, 2nd ed. (National Bureau of Standards, Washington, DC, 1971) Vol. 35, National Standards Reference Data Series.

[75] E. R. Barthel, I. B. Martini, and B. J. Schwartz, "Direct observation of charge-transfer-to-solvent (CTTS) reactions: Ultrafast dynamics of the photoexcited alkali metal anion sodide Na^-," *J. Chem. Phys.* **112**, 9433 (2000).

[76] J. Faeder, N. Delaney, P. E. Maslen, and R. Parson, "Modeling structure and dynamics of solvated molecular ions: Photodissociation and recombination in $I_2^-(CO_2)_n$," *Chem. Phys.* **239**, 525 (1998).

[77] J. R. Faeder and R. Parson, "Simulations of $ICl^-(CO_2)_n$ Photodissociation: Effects of Structure, Excited State Charge Flow, and Solvent Dynamics," *J. Phys. Chem. A* **114**, 1347 (2010).

[78] D. Khuseynov, D. J. Goebbert, and A. Sanov, "Oxygen cluster anions revisited: Solvent-mediated dissociation of the core O_4^- anion," *J. Chem. Phys.* **136**, 094312 (2012).

[79] L. Sheps, E. M. Miller, S. Horvath, M. A. Thompson, R. Parson, A. B. McCoy, and W. C. Lineberger, "Solvent-Mediated Electron Hopping: Long-Range Charge Transfer in $IBr^-(CO_2)$ Photodissociation," *Science* **328**, 220 (2010).

[80] L. Sheps, E. M. Miller, S. Horvath, M. A. Thompson, R. Parson, A. B. McCoy, and W. C. Lineberger, "Solvent-mediated charge redistribution in photodissociation of IBr^- and $IBr^-(CO_2)$," *J. Chem. Phys.* **134**, 184311 (2011).

[81] L. Velarde, T. Habteyes, E. R. Grumbling, K. Pichugin, and A. Sanov, "Solvent resonance effect on the anisotropy of $NO^-(N_2O)_n$ cluster anion photodetachment," *J. Chem. Phys.* **127**, 084302 (2007).

[82] T. N. Olney, N. M. Cann, G. Cooper, and C. E. Brion, "Absolute scale determination for photoabsorption spectra and the calculation of molecular properties using dipole sum-rules," *Chem. Phys.* **223**, 59 (1997).

[83] S. B. Nielsen, P. Ayotte, J. A. Kelley, and M. A. Johnson, "Infrared spectroscopic observation of the argon isomer distribution in evaporative ensembles of $I^-\cdot ROH\cdot Ar_m$ (R = methyl, ethyl, isopropyl) clusters," *J. Chem. Phys.* **111**, 9593 (1999).

[84] W. H. Robertson, J. A. Kelly, and M. A. Johnson, "A pulsed supersonic entrainment reactor for the rational preparation of cold ionic complexes," *Rev. Sci. Instrum.* **71**, 4431 (2000).

[85] P. Ayotte, G. H. Weddle, J. Kim, and M. A. Johnson, "Vibrational Spectroscopy of the Ionic Hydrogen Bond: Fermi Resonances and Ion-Molecule Stretching Frequencies in the Binary $X^-\cdot H2O$ (X = Cl, Br, I) Complexes *via* Argon Predissociation Spectroscopy," *J. Am. Chem. Soc.* **120**, 12361 (1998).

[86] N. Chetty and V. W. Couling, "Measurement of the electric quadrupole moments of CO_2 and OCS," *Mol. Phys.* **109**, 655 (2011).

[87] N. E. Levinger, "Spectroscopy and Dynamics of Larger Cluster Ions," Ph.D. thesis, University of Colorado, 1990.

[88] M. E. Nadal, "The Study of the Photodissocation and Recombination Dynamics of Mass-Selected Cluster Ions: Solvent Effects on the Structure and Dynamics of the Ionic Chromophore," Ph.D. thesis, University of Colorado, 1996.

[89] J. E. Huheey, *Inorganic Chemistry: Principles of Structure and Reactivity*, 3rd ed. (Harper and Row, New York, 1983).

[90] H. D. B. Jenkins and D. F. C. Morris, "Crystal Radius and Enthalpy of Hydration of the Cyanide Ion," *Mol. Phys.* **33**, 663 (1977).

[91] *CRC Handbook of Chemistry and Physics*, 66th ed. (CRC, Boca Raton, 1985).

[92] D. W. Arnold, S. E. Bradforth, E. H. Kim, and D. M. Neumark, "Anion photoelectron spectroscopy of iodine-carbon dioxide clusters," *J. Chem. Phys.* **97**, 9468 (1992).

[93] D. W. Arnold, S. E. Bradforth, E. H. Kim, and D. M. Neumark, "Study of halogen-carbon dioxide clusters and the fluoroformyloxyl radical by photodetachment of $X^-(CO_2)$ (X = I, Cl, Br) and FCO_2^-," *J. Chem. Phys.* **102**, 3493 (1995).

[94] B. S. Ault, "Matrix isolation investigation of the fluoroformate anion," *Inorg. Chem.* **21**, 756 (1982).

[95] K. Hiraoka, S. Mizuse, and S. Yamabe, "Stability and structure of cluster ions: Halide ions with CO_2," *J. Chem. Phys.* **87**, 3647 (1987).

[96] K. Hiraoka, T. Shoda, K. Morise, S. Yamabe, E. Kawai, and K. Hirao, "Stability and structure of cluster ions in the gas phase: Carbon dioxide with Cl^-, H_3O^+, HCO_2^+, and HCO^+," *J. Chem. Phys.* **84**, 2091 (1986).

[97] T. B. McMahon and C. J. Northcott, "The fluoroformate ion, FCO_2^-. An ion cyclotron resonance study of the gas phase Lewis acidity of carbon dioxide and related isoelectronic species," *Can. J. Chem.* **56**, 1069 (1978).

[98] Y. Zhao, C. C. Arnold, and D. M. Neumark, "Study of the $I \cdot CO_2$ van der Waals complex by threshold photodetachment spectroscopy of I^-CO_2," *J. Chem. Soc., Faraday Trans.* **89**, 1449 (1993).

[99] K. G. Spears, "Ion-Neutral Bonding," *J. Chem. Phys.* **57**, 1850 (1972).

[100] G. Ciccotti, M. Ferrario, J. T. Hynes, and R. Kapral, "Dynamics of ion pair interconversion in a polar solvent," *J. Chem. Phys.* **93**, 7137 (1990).

[101] J. Mattay and M. Vondenhof, "Contact and solvent-separated radical ion pairs in organic photochemistry," in *Photoinduced Electron Transfer III* (Springer Berlin / Heidelberg, 1991), Vol. 159, pp. 219.

[102] M. A. Thompson, "From Femtoseconds to Nanoseconds: Simulation of IBr^- Photodissociation Dynamics in CO_2 Clusters," Ph.D. thesis, University of Colorado, 2007.

[103] P. J. Campagnola, L. A. Posey, and M. A. Johnson, "Controlling the internal energy content of sizeselected cluster ions: An experimental comparison of the metastable decay rate and photofragmentation methods of quantifying the internal excitation of $(H_2O)_n^-$," *J. Chem. Phys.* **95**, 7998 (1991).

[104] S. Wei and A. W. Castleman Jr., "Using reflectron time-of-flight mass spectrometer techniques to investigate cluster dynamics and bonding," *Int. J. Mass Spectrom. Ion Process.* **131**, 233 (1994).

[105] S. Wei, W. B. Tzeng, and A. W. Castleman Jr., "Kinetic energy release measurements of ammonia cluster ions during metastable decomposition and determination of cluster ion binding energies," *J. Chem. Phys.* **92**, 332 (1990).

[106] C. E. Klots, "Evaporative Cooling," *J. Chem. Phys.* **83**, 5854 (1985).

[107] P. C. Engelking, "Determination of cluster binding energy from evaporative lifetime and average kinetic energy release: Application to $(CO_2)_n^+$ and Ar_n^+ clusters," *J. Chem. Phys.* **87**, 936 (1987).

[108] J. M. Papanikolas, P. E. Maslen, and R. Parson, "Recombination and Relaxation of Molecular-Ions in Size-Selected Clusters - Monte-Carlo and Molecular-Dynamics Simulations of $I_2^-(CO_2)_n$," *J. Chem. Phys.* **102**, 2452 (1995).

[109] D. M. Neumark, "Time-resolved Photoelectron Spectroscopy of Molecules and Clusters," *Annu. Rev. Phys. Chem.* **52**, 255 (2001).

[110] D. M. Neumark, "Probing chemical dynamics with negative ions," *J. Chem. Phys.* **125**, 132303 (2006).

[111] D. M. Neumark, "Probing the transition state with negative ion photodetachment: experiment and theory," *Phys. Chem. Chem. Phys.* **7**, 433 (2005).

[112] A. Sanov and W. C. Lineberger, "Cluster anions: Structure, interactions, and dynamics in the sub-nanoscale regime," *Phys. Chem. Chem. Phys.* **6**, 2018 (2004).

[113] J. Simons, "Molecular Anions," *J. Phys. Chem. A* **112**, 6401 (2008).

[114] N. Delaney, J. Faeder, P. E. Maslen, and R. Parson, "Photodissociation, recombination, and electron transfer in cluster ions: A nonadiabatic molecular dynamics study of $I_2^-(CO_2)_n$," *J. Phys. Chem. A* **101**, 8147 (1997).

[115] N. Delaney, J. Faeder, and R. Parson, "Simulation of UV photodissociation of $I_2^-(CO_2)_n$: Spin-orbit quenching *via* solvent mediated electron transfer," *J. Chem. Phys.* **111**, 651 (1999).

[116] J. Faeder, N. Delaney, P. E. Maslen, and R. Parson, "Charge flow and solvent dynamics in the photodissociation of cluster ions: A nonadiabatic molecular dynamics study of $I_2^-Ar_n$," *Chem. Phys. Lett.* **270**, 196 (1997).

[117] S. Nandi, A. Sanov, N. Delaney, J. Faeder, R. Parson, and W. C. Lineberger, "Photodissociation of $I_2^-(OCS)_n$ cluster ions: Structural implications," *J. Phys. Chem. A* **102**, 8827 (1998).

[118] R. Parson, J. Faeder, and N. Delaney, "Charge flow and solvent dynamics in the photodissociation of solvated molecular ions," *J. Phys. Chem. A* **104**, 9653 (2000).

[119] A. Sanov, T. Sanford, L. J. Butler, J. Vala, R. Kosloff, and W. C. Lineberger, "Photodissociation dynamics of gas-phase $BrICl^-$ and IBr_2^- anions," *J. Phys. Chem. A* **103**, 10244 (1999).

[120] V. Vorsa, S. Nandi, P. J. Campagnola, M. Larsson, and W. C. Lineberger, "Recombination Dynamics Of Photodissociated I_2^- In Size-Selected Ar and CO_2 Clusters," *J. Chem. Phys.* **106**, 1402 (1997).

[121] N. Delaney, J. Faeder, and R. Parson, "Photodissociation and recombination of solvated I_2^-: What causes the transient absorption peak?," *J. Chem. Phys.* **111**, 452 (1999).

[122] A. Sanov, T. Sanford, S. Nandi, and W. C. Lineberger, "Spin-orbit relaxation and recombination dynamics in $I_2^-(CO_2)_n$ and $I_2^-(OCS)_n$ cluster ions: A new type of photofragment caging reaction," *J. Chem. Phys.* **111**, 664 (1999).

[123] H.-J. Werner, P. J. Knowles, G. Knizia, F. R. Manby, M. Schütz, P. Celani, T. Korona, R. Lindh, A. Mitrushenkov, G. Rauhut, K. R. Shamasundar, T. B. Adler, R. D. Amos, A. Bernhardsson, A. Berning, D. L. Cooper, M. J. O. Deegan, A. J. Dobbyn, F. Eckert, E. Goll, C. Hampel, A. Hesselmann, G. Hetzer, T. Hrenar, G. Jansen, C. Köppl, Y. Liu, A. W. Lloyd, R. A. Mata, A. J. May, S. J. McNicholas, W. Meyer, M. E. Mura, A. Nicklaß, D. P. O'Neill, P. Palmieri, K. Pflüger, R. Pitzer, M. Reiher, T. Shiozaki, H. Stoll, A. J. Stone, R. Tarroni, T. Thorsteinsson, M. Wang, and A. Wolf, MOLPRO, Version 2002.6, a package of *ab initio* programs, 2003 (http://www.molpro.net).

[124] H. Stoll, B. Metz, and M. Dolg, "Relativistic energy-consistent pseudopotentials – Recent developments," *J. Comp. Chem.* **23**, 767 (2002).

[125] P. J. Knowles and H.-J. Werner, "An efficient method for the evaluation of coupling coefficients in configuration interaction calculations," *Chem. Phys. Lett.* **145**, 514 (1988).

[126] P. J. Knowles and H.-J. Werner, "Internally contracted multiconfiguration-reference configuration interaction calculations for excited states," *Theor. Chim. Acta* **84**, 95 (1992).

[127] H.-J. Werner and P. J. Knowles, "An efficient internally contracted multiconfiguration-reference configuration interaction method," *J. Chem. Phys.* **89**, 5803 (1988).

[128] P. J. Knowles and H.-J. Werner, "An efficient second-order MCSCF method for long configuration expansions," *Chem. Phys. Lett.* **115**, 259 (1985).

[129] H.-J. Werner and P. J. Knowles, "A second order multiconfiguration SCF procedure with optimum convergence," *J. Chem. Phys.* **82**, 5053 (1985).

[130] A. Berning, M. Schweizer, H.-J. Werner, P. J. Knowles, and P. Palmieri, "Spin-orbit matrix elements for internally contracted multireference configuration interaction wavefunctions," *Mol. Phys.* **98**, 1823 (2000).

[131] R. J. Le Roy, "Level 7.7: A computer program for solving the radial Schrodinger equation for bound and quasibound levels", University of Waterloo Chemical Physics Research Report No. CP-661, 2005 (http://leroy.uwaterloo.ca/programs/).

[132] P. E. Maslen, J. Faeder, and R. Parson, "An effective Hamiltonian for an electronically excited solute in a polarizable molecular solvent," *Mol. Phys.* **94**, 693 (1998).

[133] A. J. Stone, *The Theory of Intermolecular Forces*, (Oxford, New York, 1996).

[134] W. H. Press, S. A. Teukolsky, W. T. Vetterling, and B. P. Flannery, *Numerical Recipes in C: The Art of Scientific Computing*, 2nd ed. (Cambridge University Press, New York, 1992).

[135] R. Mabbs, K. Pichugin, and A. Sanov, "Time-resolved imaging of the reaction coordinate," *J. Chem. Phys.* **122**, 174305 (2005).

[136] N. Delaney, "Understanding the Photodissociation Dynamics of Molecular Cluster Ions," Ph.D. thesis, Univeristy of Colorado, 1999.

[137] A. B. McCoy, private communication (2012).

[138] A. S. Case, private communication (2012).

[139] T. Baer and W. L. Hase, *Unimolecular Reaction Dynamics: Theory and Experiments*, (Oxford University Press, New York, 1996).

[140] L. D. Landau, "On the Theory of Transfer of Energy at Collisions II," *Phys. Z. Sowjetunion* **2**, 46 (1932).

[141] C. Zener, "Non-Adiabatic Crossing of Energy Levels," *Proc. R. Soc. London, A* **137**, 696 (1932).